

AD-A206 055

Spectroscopic Characterization of HAN-Based Liquid Gun
Propellants and Nitrate Salt Solutions

Final Report

Thomas B. Brill

January 15, 1989

U. S. ARMY RESEARCH OFFICE

DAAG29-84-K-0198

Department of Chemistry
University of Delaware
Newark, DE 19716

APPROVED FOR PUBLIC RELEASE;
DISTRIBUTION UNLIMITED

DTIC
SELECTED
MAR 23 1989
S H D

THE VIEW, OPINIONS, AND/OR FINDINGS CONTAINED IN THIS REPORT ARE THOSE OF THE AUTHOR(S) AND SHOULD NOT BE CONSTRUED AS AN OFFICIAL DEPARTMENT OF THE ARMY POSITION, POLICY, OR DECISION, UNLESS SO DESIGNATED BY OTHER DOCUMENTATION.

REPORT DOCUMENTATION PAGE

1a. REPORT SECURITY CLASSIFICATION Unclassified		1b. RESTRICTIVE MARKINGS	
2a. SECURITY CLASSIFICATION AUTHORITY		3. DISTRIBUTION/AVAILABILITY OF REPORT Approved for public release; distribution unlimited.	
2b. DECLASSIFICATION/DOWNGRADING SCHEDULE		4. PERFORMING ORGANIZATION REPORT NUMBER(S)	
6a. NAME OF PERFORMING ORGANIZATION University of Delaware		6b. OFFICE SYMBOL (if applicable)	
7a. NAME OF MONITORING ORGANIZATION U. S. Army Research Office		5. MONITORING ORGANIZATION REPORT NUMBER(S) ARL 21493.13-CH	
6c. ADDRESS (City, State, and ZIP Code) Department of Chemistry Newark, DE 19716		7b. ADDRESS (City, State, and ZIP Code) P. O. Box 12211 Research Triangle Park, NC 27709-2211	
8a. NAME OF FUNDING/SPONSORING ORGANIZATION U. S. Army Research Office		8b. OFFICE SYMBOL (if applicable)	
9. PROCUREMENT INSTRUMENT IDENTIFICATION NUMBER DAAG-29-84-K-0198		10. SOURCE OF FUNDING NUMBERS	
8c. ADDRESS (City, State, and ZIP Code) P. O. Box 12211 Research Triangle Park, NC 27709-2211		PROGRAM ELEMENT NO.	PROJECT NO.
11. TITLE (Include Security Classification) Spectroscopic characterization of HAN-based liquid gun propellants and nitrate salt solutions		TASK NO.	WORK UNIT ACCESSION NO.
12. PERSONAL AUTHOR(S) Thomas B. Brill			
13a. TYPE OF REPORT Final	13b. TIME COVERED FROM 10/1/85 TO 1/31/89	14. DATE OF REPORT (Year, Month, Day) January 15, 1989	15. PAGE COUNT 112
16. SUPPLEMENTARY NOTATION The view, opinions and/or findings contained in this report are those of the author(s) and should not be construed as an official Department of the Army position, policy, or decision, unless so designated by other documentation.			
17. COSATI CODES		18. SUBJECT TERMS (Continue on reverse if necessary and identify by block number)	
FIELD	GROUP	SUB-GROUP	Liquid gun propellants, FTIR Spectroscopy, HAN Raman Spectroscopy, Nitrate salt solutions. Thermal decomposition. (AW)
19. ABSTRACT (Continue on reverse if necessary and identify by block number) The high heating rate thermal decomposition of HAN and LP1845 was conducted using the FTIR/temperature profiling technique. The crystal structure of pure HAN was obtained. Models of the behavior of these materials during decomposition were developed. Very concentrated aqueous metal nitrate salt solutions were also investigated at high temperature and pressure by Raman spectroscopy to gain an understanding of the properties of HAN under similar conditions. To determine the feasibility of non-intrusive droplet studies by IR spectroscopy, acoustic levitation was developed as an IR spectroscopy sampling technique.			
20. DISTRIBUTION/AVAILABILITY OF ABSTRACT <input type="checkbox"/> UNCLASSIFIED/UNLIMITED <input type="checkbox"/> SAME AS RPT. <input type="checkbox"/> DTIC USERS		21. ABSTRACT SECURITY CLASSIFICATION Unclassified	
22a. NAME OF RESPONSIBLE INDIVIDUAL		22b. TELEPHONE (include Area Code)	22c. OFFICE SYMBOL

I. Statement of Problem

This research program was undertaken to provide a phenomenological, chemical description of the solution properties and decomposition characteristics of HAN-based liquid gun propellants and model nitrate salt solutions under fast-heating rate, high temperature and elevated pressure conditions. It was recognized in advance that these objectives would require the development of new spectroscopic cells geared toward the special problems of these materials and conditions. The papers and submitted manuscripts are attached.

II. Summary of the Most Important Results

- (1) The crystal and molecular structure of HAN and HAN-d₄ was determined by single crystal x-ray diffraction. (Ref. 1).
- (2) The thermal decomposition of HAN was investigated at heating rates exceeding 100°C/sec and pressures up to 1000psi. The product concentrations were found to oscillate under certain conditions. (Ref. 2).
- (3) A four-step thermal decomposition model of LP1845 was developed based on fast thermolysis at pressures up to 1000psi. H₂O is evolved, followed by the decomposition of HAN, followed by the decomposition of TEAN, followed by ignition of the sample. (Ref. 3).
- (4) Concentrated aqueous metal nitrate salt solutions were investigated up to 450°C and 5000psi by Raman spectroscopy and exhibit increasing molecularity at the higher temperatures. That is, contact ion pairs replace solvent separated ion pairs as the temperature is increased. (Ref. 4).

- (5) A description of the behavior of LP1845 under the conditions of essentially instantaneous heating at high pressure was ascertainable from the findings of (4). The contact ion pairs enhance the initial step of thermal decomposition found in (3) which is proton transfer to form HNO_3 . (Ref. 5)
- (6) A new, original design for a high pressure, high temperature Raman spectroscopy cell for aqueous solutions was developed and constructed. (Ref. 6).
- (7) A technique that permits simultaneous temperature measurements and real-time, in situ, FTIR spectroscopy to be performed was developed and constructed. (Ref. 7).
- (8) Acoustic levitation was demonstrated as a non-intrusive IR spectroscopy sampling technique for the study of droplets. (Ref. 8).

III. List of Papers Published

1. A. L. Rheingold, J. T. Cronin, T. B. Brill and F. K. Ross, Acta Cryst. C43, 402 (1987).
2. J. T. Cronin and T. B. Brill, J. Phys. Chem. 90, 178 (1986).
3. J. T. Cronin and T. B. Brill, Combust. Flame, 74, 81 (1988).
4. P. D. Spohn and T. B. Brill, J. Phys. Chem. in press.
5. T. B. Brill, P. D. Spohn and J. T. Cronin, J. Energetic Mat. in press.
6. P. D. Spohn and T. Brill, Appl. Spectrosc. 41, 1152 (1987).
7. J. T. Cronin and T. B. Brill, Appl. Spectrosc. 41, 1147 (1987).
8. J. T. Cronin and T. B. Brill, Appl. Spectrosc. in press.

IV. List of all Scientific Personnel

1. Thomas B. Brill, principal investigator
2. James T. Cronin, Ph.D. to be awarded in early 1989.
3. Peter D. Spohn, Ph.D. to be awarded in early 1989.

V. Contracts with Army Laboratory Personnel

During the research program, the behavior of LP's and the components of LP's were discussed with many Army Laboratory personnel. In particular, information transfer occurred frequently between our laboratory and Drs. Nathan Klein, Robert Fifer, John Vanderhoff, Richard Beyer, Eli Freedman, Madeline Decker, and Ron Sasse' at BRL. Many discussions with Dr. Surya Bulusu of Picatinny Arsenal also took place.

Accession For	
NTIS GRA&I	<input checked="" type="checkbox"/>
DTIC TAB	<input type="checkbox"/>
Unannounced	<input type="checkbox"/>
Justification	
By	
Litho/Repro/	
Availability Codes	
and/or	
Dist	Special
A-1	

Acta Cryst. (1987), C43, 402-404

Structure of Hydroxylammonium Nitrate (HAN) and the Deuterium Homolog

BY A. L. RHEINGOLD, J. T. CRONIN AND T. B. BRILL*

Department of Chemistry, University of Delaware, Newark, DE 19716, USA

AND F. K. ROSS*

Research Reactor, University of Missouri, Columbia, MO 65211, USA

(Received 25 June 1986; accepted 27 October 1986)

Abstract. HAN, $[\text{NH}_2\text{OH}]\text{NO}_3$, $M_r = 96.04$, monoclinic, $P2_1/c$, $a = 4.816(1)$, $b = 6.800(1)$, $c = 10.728(1)$ Å, $\beta = 99.35(1)^\circ$, $V = 346.7(1)$ Å³, $Z = 4$, $D_x = 1.841$ g cm⁻³, Mo $K\alpha$, $\lambda = 0.71073$ Å, $\mu = 1.86$ cm⁻¹, $F(000) = 200$, $T = 296$ K, $R_F = 0.032$ for 836 unique reflections. HAN- d_4 , $[\text{ND}_2\text{OD}]\text{NO}_3$, $M_r = 100.07$, monoclinic, $P2_1/c$, $a = 4.8165(8)$, $b = 6.8007(9)$, $c = 10.7298(13)$ Å, $\beta = 99.303(11)^\circ$, $V = 346.84(8)$ Å³, $Z = 4$, $D_x = 1.916$ g cm⁻³, Mo $K\alpha$, $\lambda = 0.71073$ Å, $\mu = 1.86$ cm⁻¹, $F(000) = 200$, $T = 296$ K, $R_F = 0.0411$ for 1073 unique reflections. HAN

and HAN- d_4 are isostructural. All of the H atoms are involved in hydrogen bonding with one being bifurcated. The shortest heavy-atom interionic distance is O...O at 2.796(1) Å.

Introduction. Hydroxylammonium nitrate (HAN) is an oxidizer and a chemical propellant when it is combined with an alkylammonium nitrate fuel in an aqueous solution (Klein, 1985). HAN dissolves in water in a stoichiometry up to about six HAN molecules to one H₂O molecule. The interionic distances are of interest in interpreting the IR spectra and as a starting point for modeling the solution (Fifer, 1984;

* Authors to whom correspondence should be addressed.

0108-2701/87/030402-03\$01.50

© 1987 International Union of Crystallography

Cronin & Brill, 1986). Despite being a simple salt of low molecular weight, its crystal structure has not been determined. In this paper the structures of both $[\text{NH}_2\text{OH}]\text{NO}_2$ and $[\text{ND}_2\text{OD}]\text{NO}_2$ are reported.

Experimental. Crystals for the HAN- d_4 determination at the University of Delaware were cleaved in an anhydrous environment from larger ones provided by R. A. Fifer (BRL, Aberdeen Proving Ground, Maryland). Crystals for the HAN determination at the University of Missouri were prepared by vacuum dehydration at 343 K of the commercially available 2.8 M solution (Southwestern Analytical Chemicals, Austin, Texas). Cleaved sample rounded by rolling between sheets of filter paper. Parenthetical values for HAN- d_4 . Crystal approximately 0.3 mm sphere (0.3 × 0.3 × 0.4 mm) in sealed glass capillary, Enraf-Nonius CAD-4 (Nicolet R3) diffractometer, graphite monochromator, Mo K α , 24 reflections ($27 < 2\theta < 33^\circ$) used to refine orientation matrix, empirical absorption correction ranging from 0 to 3.3% (no absorption correction), 3613 (1398) reflections collected, $\theta/2\theta$ scan for $2 < 2\theta < 60^\circ$ ($4 < 2\theta < 65^\circ$), $-6 \leq h \leq 6$, $-9 \leq k \leq 9$, $-14 \leq l \leq 14$ ($-7 \leq h \leq 7$, $0 \leq k \leq 10$, $0 \leq l \leq 16$); $R_{\text{int}} = 0.013$ (0.027), 1163 (1248) unique, 836 (1073) observed reflections [$F_o \geq 2.5\sigma(F_o)$], 72 parameters. Structure of HAN determined by full-matrix least squares using *MULTAN* from Enraf-Nonius *SDP* (Frenz, 1980); structure of HAN- d_4 by blocked-cascade procedure using direct methods *SOLV* from *SHELXTL* (Sheldrick, 1983). $R_F = 0.032$ (0.0411), $wR_F = 0.043$ (0.0437) [$w^{-1} = \sigma^2(F_o) + gF_o^2$, $g = 0.0008$, $\sigma(F_o)$ from counting statistics]. Non-H atoms anisotropic. H(O) atoms located from difference maps and refined isotropically. Final GOF 2.015 (1.485). Max. peak 0.28 (0.22) e \AA^{-3} , min. peak -0.24 (-0.24) e \AA^{-3} in final $\Delta\rho$ map. This is approximately one half of the height of the last H atom located [H(4)]. $(\Delta/\sigma)_{\text{max}} = 0.07$ (0.05). A large secondary-extinction correction was required $F^* = F_o/[1.0 + 0.002x(F_o)^2/\sin(2\theta)]^{0.25}$; x refined to 4.3×10^{-3} (9.9×10^{-4}) in final run. All form factors from *International Tables for X-ray Crystallography* (1974).

Discussion. Table 1 lists the atomic coordinates of HAN and HAN- d_4 , while Table 2 gives the intramolecular bond distances and angles, and Table 3 gives selected interionic heavy-atom distances that involve hydrogen bonding.† HAN and HAN- d_4 are isostructural and have remarkably similar crystal parameters, bond distances and angles. The structural

† Lists of structure factors and anisotropic thermal parameters have been deposited with the British Library Document Supply Centre as Supplementary Publication No. SUP 43368 (17 pp.). Copies may be obtained through The Executive Secretary, International Union of Crystallography, 5 Abbey Square, Chester CH1 2HU, England.

Table 1. Atom coordinates ($\times 10^4$) and temperature factors ($\text{\AA}^2 \times 10^3$)

	x	y	z	U_{eq}
HAN-d_4				
O(1)	-528 (2)	-2054 (1)	6137 (1)	33 (1)*
O(2)	3194 (2)	-2132 (1)	5233 (1)	34 (1)*
O(3)	-772 (2)	-3198 (2)	4238 (1)	44 (1)*
O(4)	5347 (2)	397 (1)	7214 (1)	33 (1)*
N(1)	613 (2)	-2457 (1)	5193 (1)	25 (1)*
N(2)	3595 (2)	-360 (1)	8014 (1)	28 (1)*
D(1)	2142 (39)	-920 (25)	7563 (14)	39 (4)
D(2)	4631 (40)	-1108 (27)	8525 (15)	47 (4)
D(3)	2956 (40)	570 (26)	8464 (16)	49 (5)
D(4)	5000 (38)	-244 (26)	6606 (15)	45 (5)
HAN				
O(1)	-527 (2)	-2052 (1)	6139 (1)	33 (1)*
O(2)	3185 (2)	-2125 (1)	5233 (1)	34 (1)*
O(3)	-779 (2)	-3197 (1)	4241 (1)	44 (1)*
O(4)	5352 (2)	396 (1)	7213 (1)	33 (1)*
N(1)	610 (2)	-2454 (1)	5193 (1)	25 (1)*
N(2)	3592 (2)	-361 (1)	8014 (1)	28 (1)*
H(1)	2075 (29)	-950 (21)	7563 (11)	41 (4)
H(2)	4655 (30)	-1157 (3)	8546 (12)	53 (4)
H(3)	2935 (32)	631 (22)	8426 (11)	52 (4)
H(4)	4994 (30)	-235 (23)	6545 (11)	52 (4)

* Equivalent isotropic U defined as one third of the trace of the orthogonalized U_{ij} tensor.

Table 2. Bond distances (\AA) and angles ($^\circ$)

	HAN- d_4	HAN
O(1)-N(1)	1.259 (1)	1.259 (1)
O(3)-N(1)	1.235 (1)	1.234 (1)
O(4)-D(4)	0.780 (17)	0.829 (12)
N(2)-D(2)	0.849 (17)	0.886 (13)
O(2)-N(1)	1.256 (1)	1.254 (1)
O(4)-N(2)	1.395 (1)	1.399 (1)
N(2)-D(1)	0.872 (17)	0.902 (12)
N(2)-D(3)	0.881 (18)	0.892 (12)
Angles		
O(1)-N(1)-O(2)	119.5 (1)	119.4 (1)
O(2)-N(1)-O(3)	119.9 (1)	120.1 (1)
O(4)-N(2)-D(2)	105.3 (13)	106.0 (7)
O(4)-N(2)-D(3)	111.9 (12)	109.0 (7)
D(2)-N(2)-D(3)	107.2 (16)	110.9 (9)
N(2)-O(4)-D(4)	103.9 (14)	106.2 (8)
O(1)-N(1)-O(3)	120.6 (1)	120.5 (1)
O(4)-N(2)-D(1)	109.3 (11)	110.6 (7)
D(1)-N(2)-D(2)	115.6 (16)	114.0 (11)
D(1)-N(2)-D(3)	107.3 (17)	106.3 (11)

Table 3. Shortest heavy-atom interionic distances (\AA)

Transformations are those to create the second atom.

	HAN- d_4	HAN
O(1)...N(2)	2.834 (1)	2.830 (1)
O(2)...O(4)	2.800 (1)	2.796 (1)
$x, -\frac{1}{2}y, \frac{1}{2}z$		
O(3)...N(2)	2.829 (1)	2.833 (1)
O(2)...N(2)	2.961 (1)	2.963 (1)
$-x, \frac{1}{2}y, \frac{1}{2}z$		
O(1)...N(2)	2.916 (1)	2.916 (1)
$1+x, \frac{1}{2}y, \frac{1}{2}z$		
O(3)...N(2)	2.983 (1)	2.981 (1)

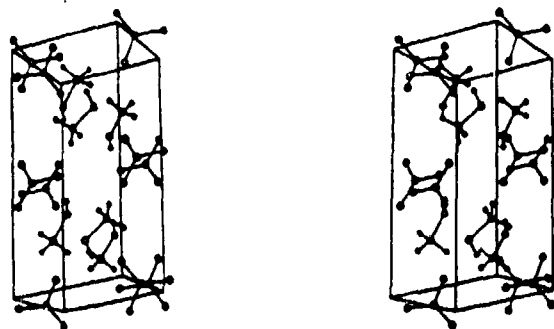


Fig. 1. Stereoscopic view of the unit cell along the *b* axis.

consequences of deuteration of HAN are thus rather small. As shown in Fig. 1, the crystals at room temperature are devoid of water of crystallization despite the strong affinity that HAN and H_2O have for one another.

The local environment of the NH_2OH^+ ion is shown in Fig. 2. All of the H atoms take part in hydrogen bonding, with H(2) being bifurcated between O(2) and O(3). This distribution is consistent with the H to NO_3^- stoichiometry and the tendency for all H atoms in salts such as HAN to be involved in hydrogen bonding (Olovsson & Jönsson, 1976). The interionic $O \cdots O$ and $O \cdots N$ distances correspond to $O-H$ and $N-H$ bond distances of about 0.96 and 1.03 Å, respectively (Olovsson & Jönsson, 1976). As expected, however, the distances refined from diffraction data are about 0.2 Å shorter than this because of the scattering model used for the H atoms. Within the nitrate anion the $N-O$ bond distances differ slightly despite the fact that all of the O atoms are involved in significant hydrogen-bonding interactions.

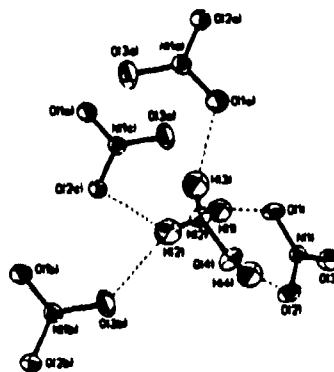


Fig. 2. The local environment of NO_3^- ions surrounding the $[NH_2OH]^+$ ion showing the hydrogen-bonding interactions.

TBB thanks the Army Research Office for support under DAAG-29-84-K-0198 and Dr R. A. Fifer for a sample of HAN- d_4 . FKR thanks the Army Research Office for support under DAAG-29-85-K-0064.

References

- CRONIN, J. T. & BRILL, T. B. (1986). *J. Phys. Chem.* **90**, 178-181.
 FIFER, R. A. (1984). Chemical Propulsion Information Agency Publication No. 412, Vol. II, pp. 529-541.
 FRENZ, B. A. (1980). *Enraf-Nordius Structure Determination Package*, Version 17, College Station, Texas.
International Tables for X-ray Crystallography (1974), Vol. IV. Birmingham: Kynoch Press. (Present distributor D. Reidel, Dordrecht.)
 KLEIN, N. (1985). BRL TR-2641. Ballistics Research Laboratory, Aberdeen Proving Ground, Maryland.
 OLOVSSON, S. & JÖNSSON, P.-G. (1976). In *The Hydrogen Bond*, Vol. II, edited by P. SCHUSTER, G. ZUNDEL & C. SANDORFY, pp. 393-457. New York: North-Holland.
 SHELDRIK, G. M. (1983). *SHELXTL Users Manual*, Revision 4.1. Nicolet XRD Corporation, Madison, Wisconsin.

Thermal Decomposition of Energetic Materials. 8. Evidence of an Oscillating Process during the High-Rate Thermolysis of Hydroxylammonium Nitrate, and Comments on the Interionic Interactions

J. T. Cronin and T. B. Brill*

Department of Chemistry, University of Delaware, Newark, Delaware 19716 (Received: June 17, 1985)

Relatively dry, solid hydroxylammonium nitrate (HAN), $(\text{NH}_2\text{OH})\text{NO}_3$, was examined by IR spectroscopy from 170 K to well above its decomposition point. The modes in the $2600\text{--}2950\text{-cm}^{-1}$ range are assigned to $-\text{NH}_2^+$ combination tones, rather than to $\nu(\text{OH})$ as was recently proposed for aqueous HAN solutions. Frequency-to-distance correlations for solid HAN cast doubt on the viability of using $\nu(\text{NH}/\text{OH})$ fundamentals to determine accurate interionic distances in HAN. Several of the thermolysis products of HAN (HNO_3 , N_2O , and NO_2) were quantified in real time by rapid-scan FTIR and were found to oscillate when solid HAN and aqueous HAN solutions were pyrolyzed at a high rate (130 K s^{-1}) with pressures ≥ 100 psi of Ar. The onset of the oscillation is delayed by increasing the initial H_2O content. The period of oscillation at constant pressure increases with the heating rate. Some comments on the reactions that may lead to the decomposition products of HAN are made based on these findings.

Introduction

Extremely concentrated aqueous hydroxylammonium nitrate (HAN), $(\text{NH}_2\text{OH})\text{NO}_3$, and aliphatic ammonium nitrates are combustible at elevated temperature and pressure making them interesting as chemical propellants.¹ Many of the fundamental structural and decomposition questions about HAN and HAN solutions remain to be answered. In this paper the vibrational mode assignments and their relationship to interionic interactions in HAN have been reexamined in an attempt to clarify several contradictory aspects. Rapid-scan FTIR spectroscopy (RSFTIR) characterizes real-time, high-heating rate thermolysis of HAN and HAN solutions and has provided an intriguing view into the dynamics of the process. The most interesting observation is the temporal oscillations that take place among the product concentrations at elevated pressure.

Experimental Section

Samples of solid and aqueous HAN and HAN- d_4 were generously supplied by R. A. Fifer and N. Klein, BRL, Aberdeen, MD. Multiple freeze-thaw cycles under vacuum were used in an effort to obtain H_2O -free solid HAN. The percent deuteration

of HAN- d_4 was enhanced by the addition of D_2O before the freeze-thaw cycles.

The calibrated pyrolysis cell, spectral methods, and data reduction for high-rate thermal decomposition at specific pressures and heating rates using RSFTIR are fully described elsewhere.² Ramp heating occurs until the final filament temperature (T_f) is reached. T_f is then maintained for the remainder of the 10-s data collection. The Nicolet 60SX FTIR spectrometer with an MCT detector was set for 10 scans s^{-1} , 2 scans per file, 4-cm^{-1} resolution. Approximately 1 mg of sample was placed on the nichrome filament by a micropipet as necessary for the solutions. This procedure was carried out under an Ar blanket. The cell was then closed and the Ar pressure adjusted to the desired level. Thermolysis was conducted at 2, 15, 50, 100, 200, 500, and 1000 psi (1 psi = 6.9 KPa). The heating rates were $130 \pm 10\text{ K s}^{-1}$ and the final filament temperature ranged from 600 K at 2 psi to 500 K at 1000 psi. These experiments were repeated a number of times to perfect the technique and because an occasional erratic result was obtained. While the details of the product concentrations vary slightly from run to run, the essential features are reproducible and accurate in all cases. Erratic behavior seemed to occur when the sample droplet size was allowed to vary too

(1) For a review see Klein, N. BRL-TR-2641, Ballistics Research Laboratory, Aberdeen Proving Ground, MD, Feb 1985.

(2) Oyumi, Y.; Brill, T. B. *Combust. Flame* 1985, 62, 213.

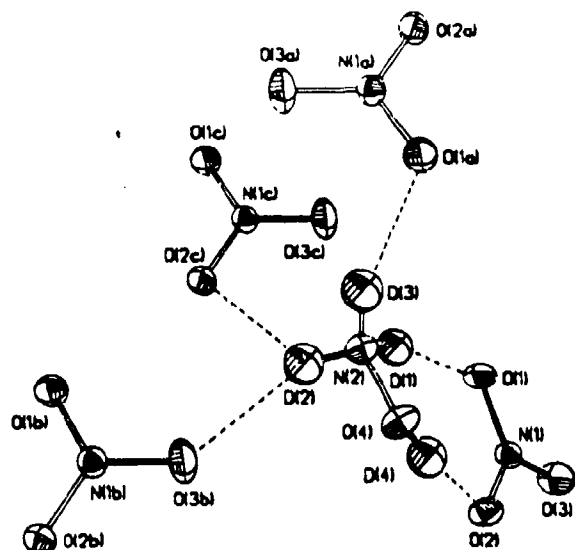


Figure 1. The microenvironment of NO_3^- ions about ND_3OD^+ in crystalline HAN-d_4 . The hydrogen bond contacts are shown as dashed lines.

much. The absorbance values were converted to concentration-time profiles (percent by volume) by the use of the absolute intensities of characteristic modes.² $\text{H}_2\text{O}(\text{g})$ was not quantified because the vibration-rotation fine structure complicated the integration process. IR-inactive species, such as N_2 and O_2 , were not quantified. HAN solutions are known to be unstable in the presence of certain metal ions.^{3,4} Therefore, we compared the thermolysis results for HAN on a nichrome and a gold-plated nichrome filament using the same experimental conditions. No differences were detected.

The spectrum of neat HAN between 170 and 470 K was examined by using slow heating and cooling (5 K min^{-1}) as appropriate. The sample resided in a semiconfined state between two NaCl plates,⁵ and the temperature was measured by embedding a type J thermocouple between the plates and recording the temperature with a Fluke digital thermometer. Thirty-two scans at 1-cm^{-1} resolution were recorded.

Solid HAN and HAN-d_4

The details of recent crystal structure determinations of HAN and HAN-d_4 will appear separately.⁶ HAN and HAN-d_4 are isostructural ($P2_1/c$, $Z = 4$) and possess remarkably similar distances and angles. Figure 1 shows the NO_3^- environment surrounding a single ND_3OD^+ ion. All of the hydrogen atoms engage in hydrogen bonding with one of the N-D bonds being bifurcated. The $\text{O}(2)\cdots\text{O}(4)$ distance is $2.800(1) \text{ \AA}$ while the shortest interionic $\text{N}\cdots\text{O}$ distances lie in the range of $2.834\text{--}2.983(1) \text{ \AA}$. These distances would categorize HAN as a moderately strongly hydrogen-bonded solid. There is no H_2O of crystallization in the lattice. Since the ions of HAN lie at C_1 sites of the unit cell, none of the vibrational modes remains fully degenerate and all have "a" symmetry.

Many of the IR-active absorptions of HAN and HAN-d_4 at room temperature have been assigned previously in the solid and solution state.⁷⁻¹⁰ Table I lists the frequencies observed in this work for solid HAN and HAN-d_4 . In addition to the fundamentals, a number of overtone/combination bands appear which have become enhanced by the N-H and O-H vibrational anharmonicity introduced by hydrogen bonding. The intensity of

TABLE I: Mid-IR Frequencies (cm^{-1}) for Solid HAN and HAN-d_4 at 297 K^a

$(\text{NH}, \text{OH})\text{NO}_3$	$(\text{ND}, \text{OD})\text{NO}_3$	tentative assignments
3140 sh, m		H_2O
	2422 w	$2\nu_{\text{as}}(\text{ND}_3^+)$
3043 vs, b	2315 s, b	$\nu_{\text{as}}(\text{NH/D}) + \nu(\text{OH/D})$
2991 vs, b	2258 s, b	
2920 sh, s	2165 w, b	$\nu_{\text{s}}(\text{NH/D})$
2880 s		
2750 m	2113 w	$\text{NH}_3/\text{D}_3^+ + \text{OH/D}$ bending combination bands
(1182 + 1554)	(856 + 1258)	
2711 m	2023 w	
(1182 + 1535)	(797 + 1258)	
2685 m	1969 w	
(1149 + 1535)	(856 + 1144)	
2653 m		
(1182 + 1473)		
2626 m		
(1182 + 1455)		
2386 w		$\delta_{\text{as}}(\text{NH}_3/\text{D}_3^+) + \text{lattice}$ $(\nu_1 + \nu_2)(\text{NO}_3^-)$
2(1182)		
1846 w, b	1559 w, b	$\delta_{\text{as}}(\text{NH}_3/\text{D}_3^+)$
1755 m	1785 w	
1554 m	1258 w	$\delta_{\text{as}}(\text{NH}_3/\text{D}_3^+)$
1535 w		
1473 m	1147 m	$\delta_{\text{as}}(\text{NH}_3/\text{D}_3^+)$
1455 m		
1428 m, sh		$\nu_3(\text{NO}_3^-)$
1371 vs	1353 vs	
1182 s	856 m	NH_3/D_3^+ rock
1149 s	797 m	OH/D bend
1075 w	1020 w	$\nu_1(\text{NO}_3^-)$
987 s	981 m	$\nu(\text{N-O})$
818 s	634 m	$\nu_2(\text{NO}_3^-)$

^a vs = very strong, s = strong, m = medium, w = weak, b = broad, sh = shoulder.

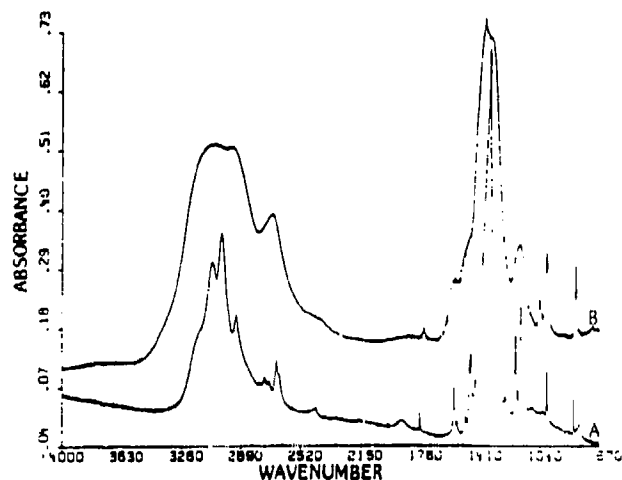


Figure 2. (a) The mid-IR spectrum of solid, partially dry HAN at 297 K . The shoulder at 3140 cm^{-1} is H_2O dependent and appears not to be a HAN fundamental. (b) Melted HAN at 350 K .

the shoulder at 3140 cm^{-1} in solid HAN (Figure 2a) depends on the amount of adsorbed H_2O present in the sample and is, therefore, unlikely to be a HAN mode. We concur with most of the previous assignments on hydroxylammonium salts⁷⁻¹⁴ and have added several further assignments to weak overtone and combination bands in HAN . Recently, it was suggested that the absorptions in the $2620\text{--}2750\text{-cm}^{-1}$ range of aqueous HAN are produced by $\nu(\text{OH})$ ^{9,11} of a very short $\text{NH}_3\text{OH}^+\cdots\text{ONO}_2^-$ contact ion pair.⁹ The $\text{O}\cdots\text{O}$ distance (2.61 \AA) that was subsequently

- (3) Klein, N. *Proc. I.C.T. Int. Jahr* 1984, 167.
- (4) Bengtsson, A. *Acta Chem. Scand* 1973, 27, 1717.
- (5) Karpowicz, R. J.; Brill, T. E. *Appl. Spectrosc.* 1983, 27, 79.
- (6) Ross, F. K.; Rheingold, A. L.; Durney, R.; Cronin, J. T.; Brill, T. B. to be submitted for publication.
- (7) Rocchiccioli, C. *Compt. Rendu* 1961, 253, 838.
- (8) Hamann, S. D.; Linton, M. *Aust. J. Chem.* 1976, 29, 164.
- (9) Fifer, R. A. *CPIA Publ.* 1984, No. 412, Vol. II, 529.
- (10) Cronin, J. T.; Brill, T. B. Proceedings of the International Conference on the Computerization of FTIR Spectroscopy, SPIE, June 1985, in press.

- (11) VanDijk, C. A. GC-TR-83-26G, GeoCenters, Inc., Newton Upper Falls, MA, May 1983.
- (12) VanDijk, C. A.; Priest, R. G. *Combust. Flame* 1984, 57, 15.
- (13) Bunte, S. W.; Vanderhoff, J. A.; Miziolek, A. W. *CPIA Publ.* 1984, 412, Vol. II, 547.
- (14) Frasco, D. L.; Wagner, E. L. *J. Chem. Phys.* 1959, 30, 1124.

calculated from this frequency⁹ is 0.19 Å shorter than exists in the crystalline HAN,⁶ a fact that, if true, would be surprising. The resolution of these modes in the spectrum of the solid phase (Figure 2a) and in other hydroxylammonium salts^{7,12,14} and alkylammonium salts¹⁵ lends credence to their assignment to $-\text{NH}_3^+$ combination bands rather than to an OH fundamental. These modes merge into an unresolved broad absorption in molten HAN at 350 K (Figure 2b) and by dissolution of HAN in H_2O .

The correlation between the O—O distance and $\nu(\text{OH})$ ($2950\text{--}3100\text{ cm}^{-1}$) in crystalline HAN, as has been discussed by Novak⁶ for other hydrogen-bonded species,¹⁶ is not satisfying. The O(2)—O(4) distance in HAN by X-ray diffraction is 2.800 (1) Å which should place $\nu(\text{OH})$ in the vicinity of 3300 cm^{-1} . No absorptions in dry, solid HAN assignable to $\nu(\text{OH})$ occur above 3100 cm^{-1} . It should be noted, however, that Novak found substantial deviations from his average correlation line thereby making the frequency-to-distance connection risky for predictions about individual compounds. A possible explanation for why the distance-to-frequency correlation is so poor in HAN is the fact that the $-\text{NH}_3^+$ deformation modes in the $1420\text{--}1560\text{ cm}^{-1}$ range have approximately half the frequency of the NH and OH stretching modes. All of these modes have the same symmetry in the solid phase. Consequently, Fermi resonance can occur causing splittings and shifts in the fundamentals that do not originate from interionic bonding differences. These problems cast doubt on the viability of calculating reliable, absolute interionic distances from the IR frequencies of HAN. Confidence about the accuracy of these distances could be raised only by independent confirmation using other experimental methods.

Solid HAN which was relatively free of H_2O was cooled slowly to 170 K while its IR spectrum was recorded. There are normal frequency shifts and improved resolution at low temperature but no clear evidence of solid–solid phase transitions. Solid HAN was then heated through its melting point. All of the bands broaden upon melting but the NH and OH modes are, not surprisingly, the ones most profoundly affected owing to the fluctuations in the interionic distances brought on by the greater degree of ion mobility in the melt. The NH/OH stretching mode region, while broadened, is only slightly shifted toward higher frequency. Therefore, the hydrogen bonding in molten HAN is somewhat less, although not markedly so, than crystalline HAN. $\nu_2(\text{NO}_2^-)$ broadens, splits, and diminishes in frequency by about 20 cm^{-1} upon melting. As the temperature of the melt increases, gradual loss in the intensity of the NH_2OH^+ modes occurs beginning above 420 K. This event accelerates as T further increases. The modes remaining at 470 K result from a small residue of NH_4NO_2 which has been identified before as a decomposition product of HAN.¹⁷

High-Rate Thermolysis

Of much greater practical interest is the rapid decomposition of HAN at high heating rates. The development of a mass balance equation was not the purpose of the present work because homonuclear diatomics and $\text{H}_2\text{O}(\text{g})$, which originates both from desorption and decomposition, were not quantified. All of the other detected gas products were quantified. The rapid thermolysis of solid HAN at pressures below about 100 psi of Ar proved to be uninspiring. As shown in Figure 3 for 15 psi of Ar, the predominant product is HNO_2 , followed by N_2O and NO_2 . At this pressure the concentrations of these species remain relatively constant with time. If the pressure increases in steps to 50 psi, then the time dependence of the concentrations of HNO_2 and N_2O has successively greater negative and positive slopes, respectively. They are approximately equal in concentration after 10 s when $P = 50\text{ psi}$.

The intriguing results were obtained by rapidly pyrolyzing HAN ($dT/dt = 130\text{ K s}^{-1}$) at pressures above 100 psi. Figure 4 showing the results for solid, damp HAN at 500 psi is representative of

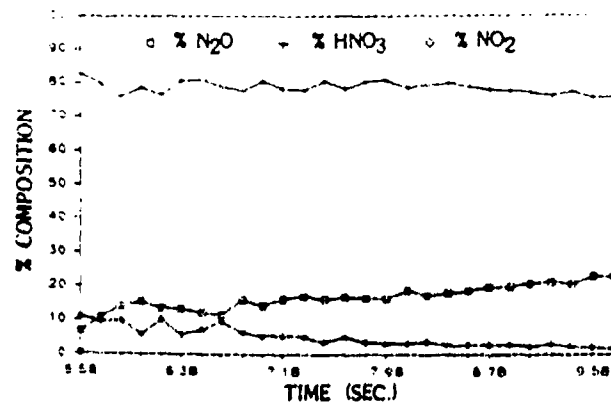


Figure 3. The thermolysis products of solid HAN in 15 psi of Ar. The heating rate was 35 K s^{-1} and T_i was 560 K. H_2O and any IR-inactive species are not quantified.

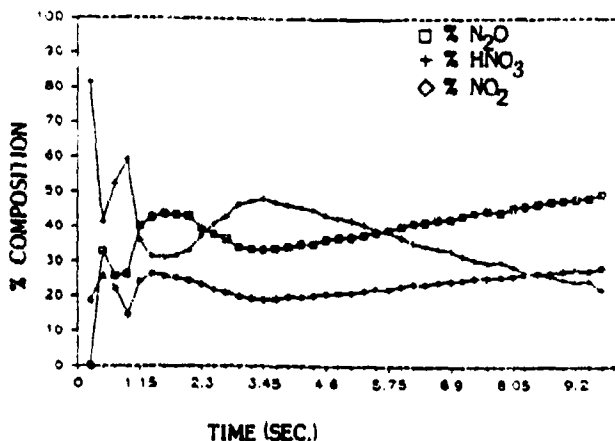


Figure 4. The temporal oscillations of the product concentrations when 1 mg of solid HAN is thermolyzed at 130 K s^{-1} and 500 psi of Ar.

the behavior. The concentrations of the products vigorously oscillate during the first few seconds of thermolysis before dampening to a more benign later stage. These temporal oscillations in the concentration somewhat resemble the behavior of less hostile, but genuinely oscillating, reactions.¹⁸ For example, the gas evolution from a concentrated aqueous solution of NH_4Cl and HNO_2 is observed to oscillate.¹⁹ Unfortunately, the conditions of HAN decomposition make it difficult to establish the source of the oscillatory process. It is not yet known whether the oscillations are chemical or physicochemical in origin. However, no oscillations of this type have been observed in any previous thermolysis studies conducted by this method^{20,21,24–27} which rules out their origin from inhomogeneities arising from convection of incomplete mixing within the cell. Beyond this, several observations in the present work at high heating rates are helpful for establishing a few of the operative factors.

First, according to the IR spectrum there is an initial burst of $\text{H}_2\text{O}(\text{g})$, (not quantified) which is then joined by $\text{HNO}_2(\text{g})$ and $\text{NO}_2(\text{g})$ followed, usually, by $\text{N}_2\text{O}(\text{g})$. The order of appearance

(18) Field, R. J.; Burger, M., Eds. "Oscillations and Traveling Waves in Chemical Systems"; Wiley-Interscience: New York, 1984.

(19) Bowers, P. G.; Noyes, R. M. *J. Am. Chem. Soc.* **1983**, *105*, 2572.

(20) Oyumi, Y.; Brill, T. B.; Rheingold, A. L.; Lowe-Ma, C. *J. Phys. Chem.* **1985**, *89*, 2309.

(21) Oyumi, Y.; Brill, T. B. *J. Phys. Chem.* **1985**, *89*, 4325.

(22) Bonner, F. T.; Kada, J.; Phelan, K. G. *Inorg. Chem.* **1983**, *22*, 1389.

(23) Pembridge, J. K.; Stedman, G. *J. Chem. Soc., Dalton Trans.* **1979**, 1657.

(24) Oyumi, Y.; Brill, T. B. *Combust. Flame* **1985**, *62*, 225.

(25) Oyumi, Y.; Brill, T. B. *Combust. Flame* **1985**, *62*, 233.

(26) Oyumi, Y.; Brill, T. B. *Combust. Flame*, submitted for publication.

(27) Oyumi, Y.; Brill, T. B.; Rheingold, A. L. *J. Phys. Chem.* **1985**, *89*, 4824.

(15) Cabana, A.; Sandorfy, C. *Spectrochim. Acta* **1962**, *18*, 843.

(16) Novak, A. *Struct. Bonding (Berlin)* **1974**, *18*, 177.

(17) Klein, N. BRL-TR-02471, Ballistics Research Laboratory, Aberdeen Proving Ground, MD, Feb 1983.

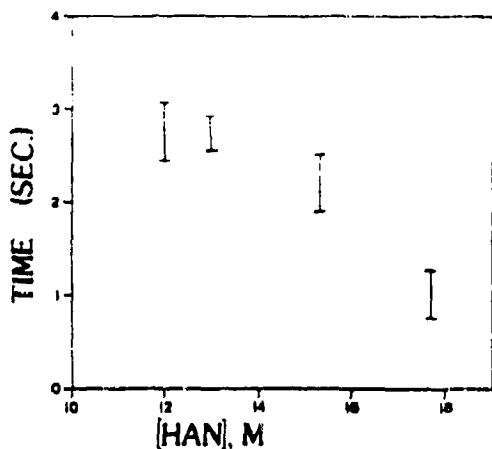
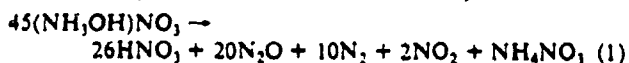


Figure 5. The relationship of the initial $[\text{HNO}_3] = [\text{N}_2\text{O}]$ crossover (see Figure 4) to the H_2O content of the HAN sample ($dT/dt = 130 \text{ K s}^{-1}$, $T_f = 510 \text{ K}$, $P = 500 \text{ psi}$ of Ar). Damp solid HAN was estimated to be 17.5 M.

of N_2O and NO_2 was reversed in several instances, and we believe that the actual and apparent order of formation can be switched by small differences in the time interval between the onset of heating and the recording of the first interferogram containing gas product information. Once reaching the 20–30% range $[\text{NO}_2]$ remains relatively steady, while $[\text{N}_2\text{O}]$ and $[\text{HNO}_3]$ fluctuate and cross one another several times. The initial crossover of HNO_3 and N_2O can be delayed by increasing the initial H_2O content of the sample (Figure 5). On this basis we believe that some of the unusual features of the thermolysis process of HAN may be tied to the effect of H_2O . Possibly the initial vaporization of some of the adsorbed H_2O may momentarily cool the sample which, in turn, affects the product distribution by altering the rates of the various competitive decomposition reactions. The oscillations are difficult to create in less than 12 M HAN solutions. Changing the heating rate/ T_f at constant pressure also affects the frequency of the oscillations. Higher heating rates and final filament temperatures were observed to compress the oscillations into a shorter time interval.

Second, the detectable gas products are those that occur from HAN decomposition in the absence of a catalyst.¹⁷



The concentrations observed in this work are not in the balance of eq 1 and N_2 is, of course, not detected. However, secondary reactions involving the products will alter the product distribution. N_2O and NO_2 are products well established by previous thermolysis studies on HAN.^{12,13,28} The products from (1) would be expected to form by multiple pathways involving radical in-

termediates. Therefore, considerable speculation enters when dissecting (1) to specify reactions that might contribute to these final products. Most of the reactions below are themselves multistep and could be occurring in parallel.

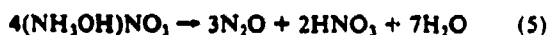
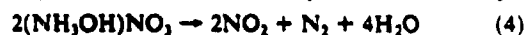
The dominant initially observed decomposition product from HAN is $\text{HNO}_3(\text{g})$. The same is true of the other simple amine nitrate salts studied to date by these RSFTIR methods: $[\text{C}(\text{C}-\text{H}_2\text{NH}_2)_4](\text{NO}_3)_4$,²⁰ $[\text{C}(\text{NHNH}_2)_3]\text{NO}_3$,²¹ and NH_4NO_3 .^{20,21} Therefore, an early step of HAN decomposition at high temperature may be rapid proton transfer from NH_3OH^+ to NO_3^- (2), but, as shown below, this is not the only path by which HAN



might produce HNO_3 . The NH_3OH from (2) would be expected to degrade, perhaps by (3).²² Any NH_3 produced by (3) should



react with HNO_3 to produce NH_4NO_3 which is a product formed during slow thermolysis of HAN (vide supra). However, NH_4NO_3 will not survive under these rapid thermolysis conditions.^{20,21} Two other routes, (4) and (5), to HAN decomposition liberate major



products observed in this study. There is reasonable evidence to suggest that N_2O is produced at a slower rate than are NO_2 and HNO_3 which would imply that reactions 3 and 5 may be slower than reactions 2 and 4.

It is noteworthy that several species believed to be present when HAN is decomposed slowly in solution are either not present or do not survive to appear in the gas phase during rapid decomposition. These species include HONO ,²³ NO_2^- ,¹³ and NO_2^+ .¹¹⁻¹³ NO has been identified among the products of HAN decomposition when time-delayed analysis is employed.²⁴ Both $\text{HONO}(\text{g})$ and $\text{NO}(\text{g})$ are readily detected products from other energetic materials.^{12,21,24-27} The fact that they are not detected from HAN at any pressure (2–1000 psi) or heating rate used implies that both have a concentration <2% of the total products under these conditions.

Just as the present real-time rapid thermolysis experiments produce results that are at some variance with previous slow heating and time-delayed experiments, we anticipate that combustion experiments on liquid HAN droplets will yield findings that update those presented here. Further studies will be forthcoming on characterizing the thermolysis of aliphatic ammonium nitrate fuels at high rates and then, ultimately, the thermolysis of aqueous solutions of HAN mixed with these fuels.

Acknowledgment. We are grateful to the Army Research Office for support of this work under grant DAAG29-84-K-0198. The Air Force Office of Scientific Research provided funds toward the purchase of the FTIR spectrometer. The technical assistance of Y. Oyumi and S. F. Palopoli was most appreciated.

Registry No. $(\text{NH}_3\text{OH})\text{NO}_2$, 13465-08-2; HNO_3 , 7697-37-2; N_2O , 10024-97-2; NO_2 , 10102-44-0.

(28) Kaufman, J. J.; Koski, W. S. Final Report to ARO, Research Triangle Park, NC, April 1980 (AD-A083-646).

Thermal Decomposition of Energetic Materials 29—The Fast Thermal Decomposition Characteristics of a Multicomponent Material: Liquid Gun Propellant 1845

J. T. CRONIN and T. B. BRILL

Department of Chemistry, University of Delaware, Newark, DE 19716

The high-rate ($> 100^{\circ}\text{C sec}^{-1}$) decomposition characteristics of a multicomponent liquid gun propellant containing hydroxylammonium nitrate (HAN), triethanol ammonium nitrate (TEAN), and water are described with the rapid-scan FTIR thermal profiling technique. The decomposition characteristics of the HAN and TEAN components were examined and then compared to the pyrolysis behavior of the liquid gun propellant 1845 (LGP1845). A four-step process that describes the major events occurring during the fast thermal decomposition and ignition of LGP1845 is presented.

INTRODUCTION

The thermal decomposition of multicomponent energetic materials in the condensed phase is complicated by the fact that synergistic interactions probably occur that will not be present upon thermolysis of the individual ingredients. Therefore, it is a challenging problem to differentiate the influence of each component on the total process. We have recently developed a new, real-time, thermolysis technique consisting of rapid-scan infrared spectroscopy conducted simultaneously with measurement of the temperature of the condensed phase (rsFTIR-thermal profiling) [1]. The heating rates employed (up to about $400^{\circ}\text{C s}^{-1}$) bring the results closer to the practical domain of propellants. With this technique the endothermic and exothermic events in the condensed phase can be correlated in real time with the various products appearing in the gas phase. This method shows great promise for fundamental investigations of multicomponent energetic materials at high heating rates and high pressures.

In this paper we report the decomposition and ignition characteristics of the liquid gun propellant 1845 (LGP1845) [2]. The propellant LGP1845 is a

multicomponent, nitrate-salt-based, aqueous propellant containing 63.2% hydroxylammonium nitrate (HAN), 19.9% triethanol ammonium nitrate (TEAN) and 16.8% H_2O by weight. By studying the individual components of LGP1845, and LGP1845 itself as a function of pressure, the sequential chemical steps that produce decomposition and ignition have been qualitatively differentiated and identified.

EXPERIMENTAL

Samples of HAN, TEAN, and LGP1845 were supplied by N. Klein of the Ballistic Research Laboratory in Aberdeen Proving Ground, MD.

The pyrolysis cell, spectral methods, and data reduction procedures for rsFTIR-thermal profiling analysis have been described elsewhere [1]. The rsFTIR-thermal profiling experiment consists of recording IR spectra of the evolved gas products as the temperature of the sample is simultaneously recorded. A Nicolet 60SX FTIR spectrometer with an MCT-B detector, set for 10 scans per second, with 2 scans per file and 4 cm^{-1} resolution was used to record the IR spectra as the sample heated. The temperature of the condensed phase was

obtained by spot welding a type-E thermocouple to the bottom center of the nichrome ribbon filament on which the sample was placed. This filament could be heated at rates between $20^{\circ}\text{C s}^{-1}$ and $400^{\circ}\text{C s}^{-1}$. After passing through an ice-point reference and a home-built low-pass filter to eliminate 60 Hz noise, the thermocouple signal was recorded on a Nicolet 4094 digital oscilloscope. At a later time the thermocouple millivolt-versus-time data were transferred from the oscilloscope to an IBM PC via RS-232. Plots of temperature versus time were then constructed using macros written for Lotus 1-2-3.

The RSFTIR -thermal profiling was conducted with and without samples so that a reference could be obtained. A calibrated Hamilton microsyringe was used to transfer the liquid sample. In each case the pyrolysis cell was then sealed, purged with argon, and the pressure of argon adjusted to the desired level. In all cases the sample remained on the filament for a maximum of several minutes. The experiment was initiated by starting the spectrometer scanning, triggering the oscilloscope to begin recording the output of the thermocouple, and simultaneously activating the heating of the filament and shutter circuit, which opened the shutter and allowed the IR beam to pass through the cell. With this timing sequence, the first interferogram corresponded to the onset of heating of the sample. The computer clock kept track of the time of each interferogram. In this way the time, temperature and spectral file could be correlated.

The RSFTIR -thermal profiling experiment was conducted at various pressures ranging from 15 psi to 1000 psi Ar. The heating rates were adjusted as desired from 50 – $400^{\circ}\text{C s}^{-1}$. The experiments were repeated a number of times to ensure reproducibility. While the details of the product concentrations and thermal profiles vary slightly from run to run, the essential features were reproducible and accurate in all cases. For relative quantitation of the gas products the IR absorbance values were converted to plots of concentration (percent by volume) versus time by using the absolute intensities of the characteristic modes [3]. Steam (H_2O) was observed but not quantified because the vibration-rotation fine structure com-

plicated the integration process. Infrared inactive products, such as N_2 , were not quantified.

Because the decomposition of HAN is known to be catalyzed by Fe and Cu [4], the decomposition product distribution from LGP1845 on different metallic ribbon filaments was examined. The standard nichrome filament (chromel A) used in this work consisted of 80% Ni and 20% Cr. In an effort to render the filament surface more inert, 1000 Å of gold was sputtered onto the surface. No significant differences were found among the thermolysis products of LGP1845 from this surface and that of the bare nichrome surface. An attempt to cover the nichrome surface with SiO_2 by firing the filament coated with hexamethyldisiloxane [5] was unsatisfactory. The filament expanded during heating, breaking the continuity of the SiO_2 layer and exposing the nichrome surface to the LGP1845 sample. In other experiments thin metal foils of Ni, Ta, and Pt were substituted for the nichrome filament. Again, the decomposition results of LGP1845 on these filaments compared with the standard nichrome filament showed no major differences. Finally, a 5-mm length of 0.005-inch diameter Fe wire was placed in contact with LGP1845 on a Pt filament. The decomposition results were not significantly different from the results of the standard nichrome filament. From these comparisons the decomposition behavior of LGP1845 appears not to be significantly altered by the surface on which it was heated, on the timescale of this experiment. However, we always took the precaution of performing the experiment as quickly as possible after loading the cell to avoid leaching the filament by the sample.

Thermolysis of HAN

Because LGP1845 is a mixture of HAN, TEAN, and H_2O , an appropriate strategy is to determine the fast heating behavior of each ingredient and then compare the results with the thermolysis characteristics of the actual propellant.

The fast decomposition of HAN in various aqueous concentrations ranging from 12 mol to 17.7 mol (solid HAN) has been reported [6]. Hence, the results will only be summarized. As shown in Fig. 1, the dominant, initial product in

THERMAL DECOMPOSITION OF LPG1845

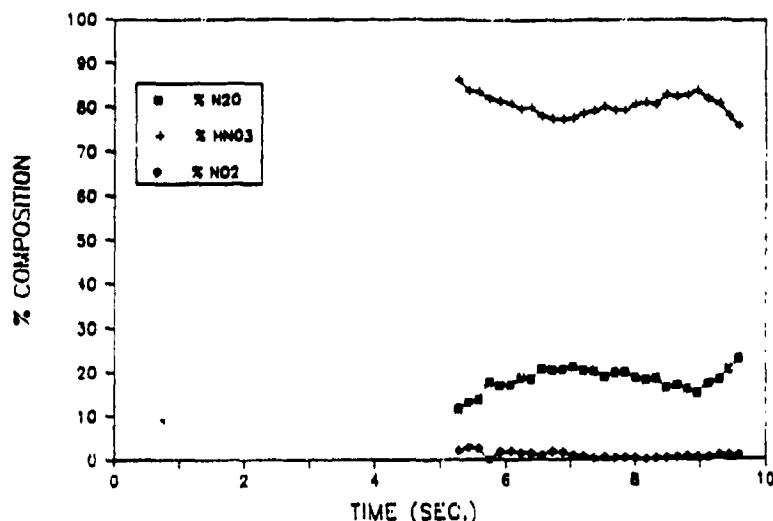


Fig. 1. The IR active gas products (excluding H₂O) evolved from the thermolysis of solid HAN at 80°C s⁻¹ under 15 psi Ar.

the decomposition of 2.5 mg of solid HAN under 15 psi Ar is HNO₃ (g). The formation of N₂O and NO₂ follows that of HNO₃. Therefore, an early step in the decomposition of HAN is probably proton transfer from NH₃OH⁺ to NO₃⁻. At this pressure the concentrations of the decomposition species remain relatively constant with time. Figure 2 shows the decomposition of 2 mg of solid HAN at 200 psi Ar and a heating rate of 80°C s⁻¹. Again, HNO₃(g) is initially detected, quickly followed by N₂O, and then by NO₂. The processes taking place to form HNO₃(g), and N₂O appear to be net endothermic because the temperature of the filament begins to lag the reference temperature trace. The formation of HNO₃ from proton transfer from the hydroxylammonium cation to the nitrate anion would be expected to be endothermic [7].

At Ar pressures of 200 psi and above, the concentrations of the products oscillate somewhat (Fig. 2) at the exotherm before dampening to constant final concentrations. As the concentration of HAN in H₂O is reduced, the severity of the oscillations lessens [6]. Also, as the concentration of water increases, the time of the initial crossover point where [HNO₃] = [N₂O] increases [6]. We believe that some of the unusual decomposition features of HAN may be attributed to the effects of

water. It is possible that the initial vaporization of water cools the reactants sufficiently that the product distributions are altered and oscillations ensue.

The exotherm in Fig. 2 begins at about 180°C and drives the filament temperature above that which would exist if no HAN were present on the filament. The NO₂ that is detected near the end of the decomposition exotherm may result from the high-temperature thermolysis of HNO₃. Infrared inactive products, such as N₂ or O₂, may also form. Nevertheless, the second stage of HAN decomposition is clearly exothermic.

Thermolysis of TEAN

The thermal decomposition and ignition of various aqueous concentrations of TEAN and solid TEAN were also investigated. Figure 3 shows a representative result of the thermolysis of 3 mg of solid TEAN under 200 psi Ar with a heating rate of 175°C s⁻¹. The first event appears to be endothermic melting of solid TEAN, which is first detected at about 105°C. This temperature is higher than the melting point measured by slow heating (80°C). Due to the high heating rates employed in this technique, some discrepancy between the melting point measured with slow heating at

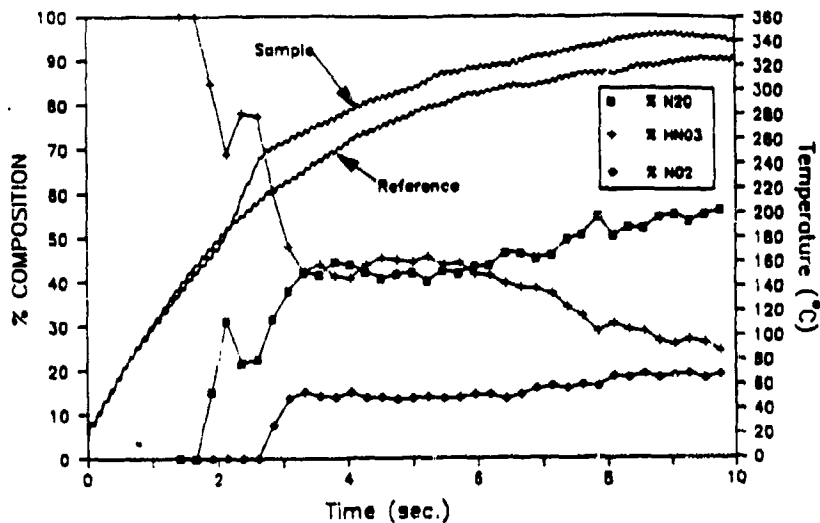


Fig. 2. The IR active gas products (excluding H_2O) evolved from the thermolysis of solid HAN at $dT/dt = 80^\circ C s^{-1}$ under 200 psi Ar. Overlaid on these products is the thermal trace of the bare filament and the thermal trace of the filament with 2.5 mg of solid HAN spread evenly on it.

equilibrium and that measured with high-heating-rate conditions is occasionally encountered. Solid TEAN liberates no detectable gas decomposition products before the exotherm. The exotherm begins in the temperature range $250-325^\circ C$. The initial product gases are detected at the exotherm and include CO_2 , N_2O , CO , NO , NH_3 , and HCN .

All of the products are detected at about the same time at this Ar pressure. These products are essentially those of the later stages of decomposition and combustion [8] of TEAN and TEAN fragments, suggesting that the effect of pressure has been to maintain the gas products near the condensed phase, raise their concentration and

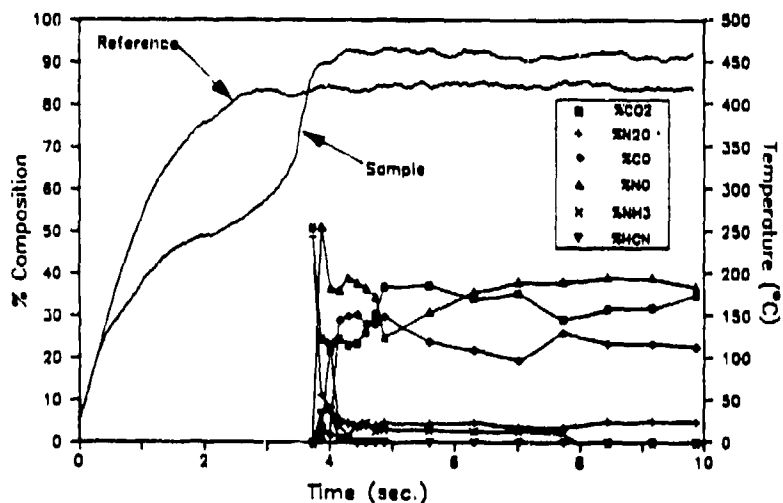


Fig. 3. The IR active gas products evolved from solid TEAN under 200 psi Ar with $dT/dt = 175^\circ C s^{-1}$. The filament reference trace and the thermal trace with 3 mg of TEAN are shown.

THERMAL DECOMPOSITION OF LPG1845

thereby create ignition conditions [8]. Concentrated aqueous solutions of TEAN exhibit essentially the same decomposition and combustion behavior as solid TEAN at pressures of at least 200 psi. Some "ash" residue remains.

Effect of H₂O

Before presenting the results for HAN-TEAN-H₂O mixtures in the form of LPG1845, it is helpful to describe the physical influence of solvent H₂O on the overall process. In the early stages of the decomposition of LPG1845, the thermal trace of the sample lags the reference trace because some heat is used to evaporate H₂O. This effect can be clearly illustrated by plotting the thermal traces of various concentrations of LPG1845 and pure H₂O, as in Fig. 4. All of these thermal traces were recorded under the same conditions: 2 μ L of liquid, 15 psi, and an initial heating rate of about 150°C s⁻¹. As expected, pure water produces the thermal trace with the longest plateau at 100°C. Note that as the plateau ends the trace becomes a smooth heating curve. As might be expected, a solution of 10% LPG1845 causes the plateau to occur at a slightly higher temperature and to be markedly shorter. After the water evaporation plateau the heating curve ex-

hibits two regions that deviate from the smooth heating trace of H₂O. These trends are continued in a more exaggerated manner for higher concentrations of LPG1845. That is, as the concentration of LPG1845 is increased, the temperature of the plateau increases and the extent of deviation from the smooth heating trace after the plateau increases. The overall effect of water is to slow the decomposition process and to reduce the magnitude of the exotherms. Removal of water increases the decomposition rate.

Thermolysis of LPG1845

Having established the independent thermolysis behavior of the three components of LPG1845, the results for the mixture become more understandable. It was informative to study the thermolysis of LPG1845 as a function of pressure because the external pressure alters the ignition characteristics [9]. Also, we found that the differentiation of the various events taking place during thermolysis can be altered by changing the pressure. Figure 5 shows the superimposition of the temperature profile and the relative concentrations of the quantified gas products from the thermolysis of 2.0 μ L of LPG1845 under 15 psi Ar and $dT/dt = 70^\circ\text{C s}^{-1}$. The thermal trace of the sample reveals

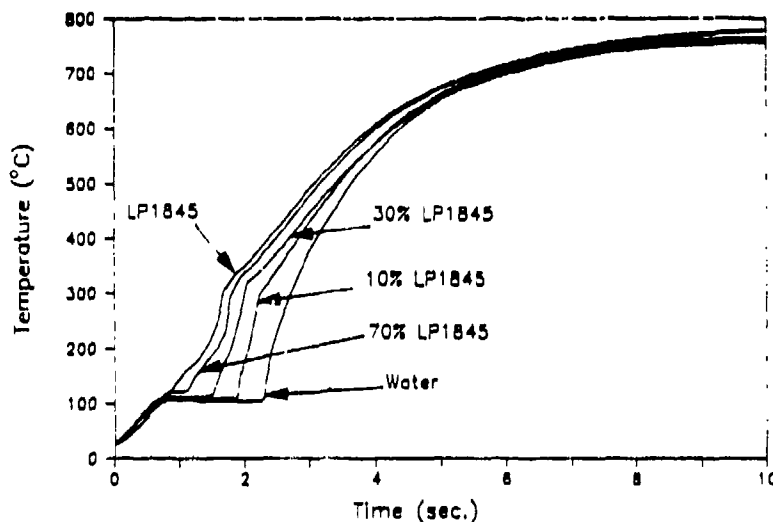


Fig. 4. The thermal traces of H₂O and LPG1845 and H₂O dilutions of LPG1845 all heated at an initial rate of about 150°C s⁻¹ under 15 psi Ar.

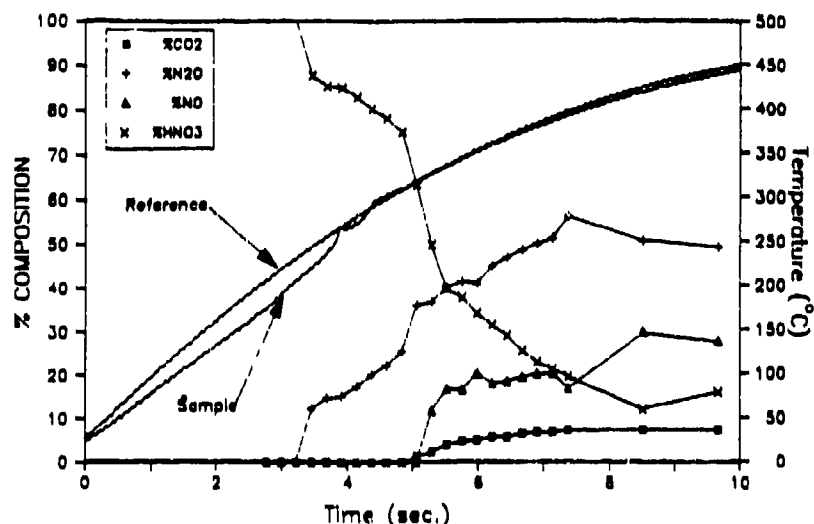


Fig. 5. The relative concentrations of the IR active gas products (excluding H_2O) when $2.0 \mu\text{L}$ of LGP1845 is heated at $dT/dt = 70^\circ\text{C s}^{-1}$ under 15 psi Ar. The reference and sample thermal traces are superimposed on these data.

that endothermic events dominate for the first 3 s of heating. Two effects appear to contribute. These are the extra heat capacity of the filament due to the presence of the sample, and the evaporation of water from the sample. According to the IR spectrum, H_2O is a prevalent product above 100°C but was not quantified for reasons mentioned in the experimental section. After about 3 s, traces of HNO_3 and N_2O are detected in the gas phase. The product HNO_3 (g) results from the endothermic proton transfer reaction of HAN followed by desorption. This process takes place in LGP1845 at about the same temperature as that in pure HAN (Fig. 2). The desorption of HNO_3 (g) and the decomposition of HAN continues until approximately 5 s after the onset of heating. At this time the first evidence of oxidation of the fuel component of LGP1845, TEAN, is detected in the form of CO_2 . This time is close to that at which the sample thermal trace crosses the reference thermal trace, indicating that heat is being generated by the sample and dissipated to the filament as a result of the exothermic oxidation of TEAN. The temperature at which the TEAN decomposition is detected is about 310°C . Although further decomposition of TEAN occurs, the combustion of LGP1845 is not complete at 15 psi Ar under these conditions.

The small amount of "ash" remaining on the filament supports this conclusion.

The products of LGP1845 were more thoroughly oxidized only when the buffer gas pressure was raised. Figure 6 shows the superimposition of the temperature profile and the relative concentrations of the gas products from the thermolysis of $2.0 \mu\text{L}$ of LGP1845 at 200 psi Ar with $dT/dt = 100^\circ\text{C s}^{-1}$. As in Fig. 2 the first products detected are HNO_3 and N_2O , signifying the endothermic decomposition of HAN at about 170°C as the first chemical event. At 4.0 s into the run, the thermal trace reveals a vigorous exotherm beginning at about $240\text{--}50^\circ\text{C}$ corresponding to the release of CO_2 , NO, HCN and CO. The increased level of CO_2 , and the presence of HCN and CO in conjunction with the large exotherm, compared to Fig. 4, at 15 psi suggest that combustion of the sample has essentially occurred.

Figure 7 shows the superimposition of the heating trace and the relative concentrations of the gas products from $1.5 \mu\text{L}$ of LGP1845 at a still higher static Ar pressure of 500 psi and $dT/dt = 110^\circ\text{C s}^{-1}$. The initial gas products detected are still HNO_3 and N_2O , which appear at 170°C and correspond to the endothermic decomposition of HAN. At about 3 s after the onset of heating, the

HERMAL DECOMPOSITION OF LPG1845

87

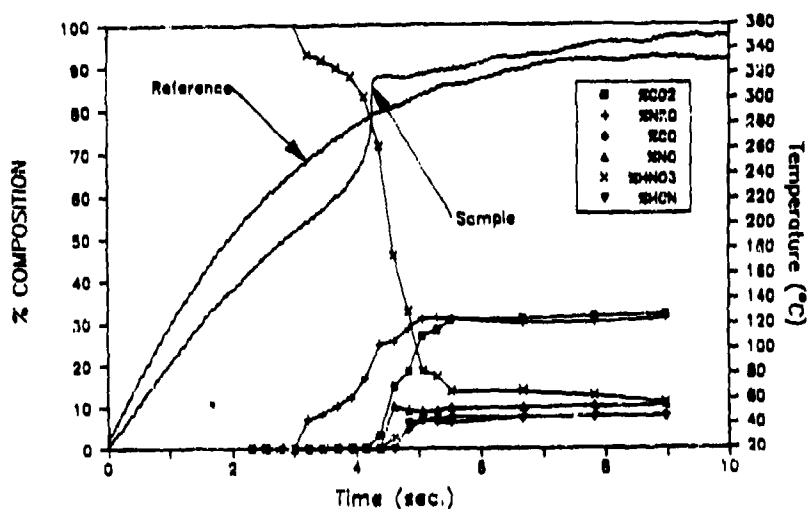


Fig. 6. The relative concentrations of the IR active gas products (excluding H_2O) when $2.0 \mu L$ of LPG1845 is heated at $dT/dt = 100^\circ C s^{-1}$ under 200 psi Ar. The reference and sample thermal traces are superposed.

thermal trace reveals a vigorous exotherm that corresponds to the evolution of CO_2 . The temperature of the exotherm onset is $240^\circ C$. However, unlike decomposition at lower pressures, decomposition at 500 psi results in CO_2 being the dominant detected product, which suggests that nearly complete combustion of the sample has occurred. The product HNO_3 appears to be the

principal initial oxidant of the fuel by this method of detection.

Figure 8 shows the results of pyrolysis for $1.5 \mu L$ of LPG1845 at 1000 psi Ar with $dT/dt = 120^\circ C s^{-1}$. As before, the decomposition of HAN initially produces HNO_3 and N_2O . At approximately 2 s, a large quantity of CO_2 is detected, which coincides with the vigorous ignition ex-

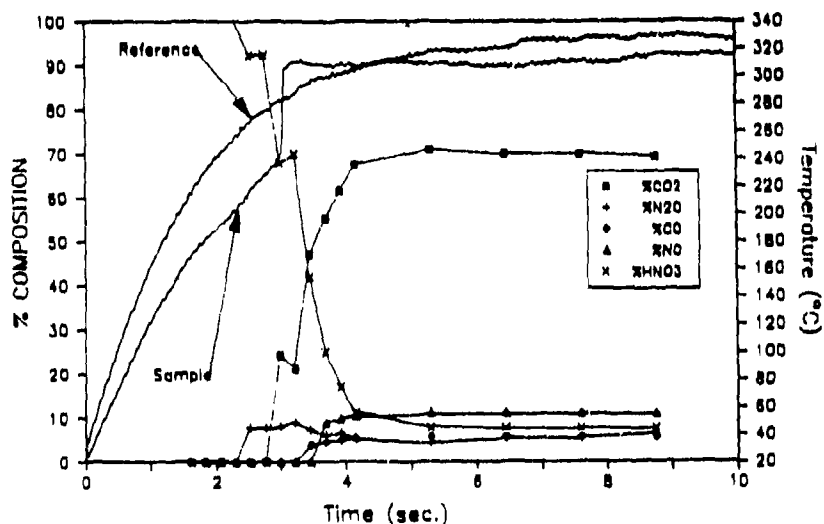


Fig. 7. The relative concentrations of the IR active gas products (excluding H_2O) when $1.5 \mu L$ of LPG1845 is heated at $dT/dt = 110^\circ C s^{-1}$ under 500 psi Ar. The reference and sample thermal traces are superposed.

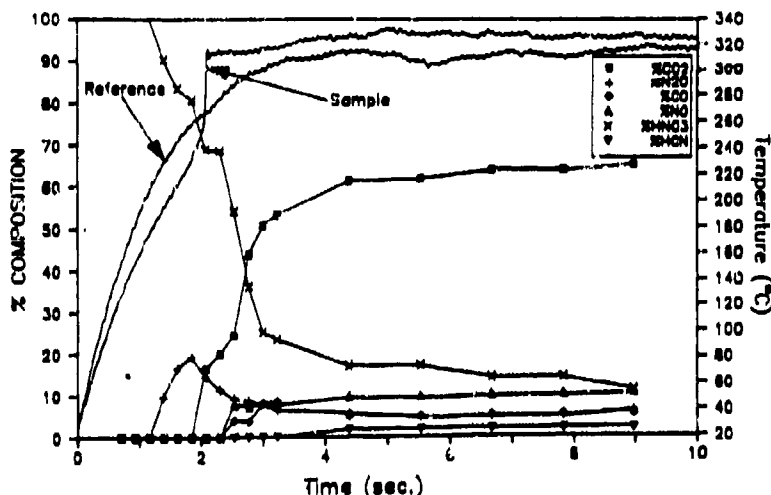


Fig. 8. The relative concentrations of the IR active gas products (excluding H_2O) when $1.5 \mu L$ of LGP1845 is heated at $dT/dt = 120^\circ C s^{-1}$ under 1000 psi Ar. The reference and sample thermal traces are superimposed.

otherm at $240\text{--}50^\circ C$. The relatively large amount of CO_2 , and the lack of HCN, signify more efficient combustion of the propellant at these higher pressures.

A phenomenological model of the chemical events taking place in the decomposition and ignition of LGP1845 may be constructed from these studies. Four main events can be identified that vary in duration and differentiation depending on the heating rate and the static applied pressure. The first step is the endothermic evaporation of solvent water, which concentrates the sample. The second step is the endothermic decomposition of HAN as manifested in the transfer of protons between NH_3OH^+ and NO_2^- to produce HNO_2 (g). Some N_2O is also detected at about this time. This reaction takes place in the range $160\text{--}70^\circ C$. The third step is the partial decomposition of TEAN, which is marked by the formation of small quantities of HCN and NO. Above atmospheric pressure and up to the 1000-psi limit of this study, this step occurs in the range $240\text{--}50^\circ C$. The fourth step is the ignition of the sample as defined by the vigorous exotherm and the formation of CO_2 , CO, H_2O , and, undoubtedly, N_2 , which is not IR active.

The steps of this general formalism for the decomposition of LGP1845 occur to varying

degrees, depending on the heating rate and pressure. The effect of increasing the heating rate is to speed the reaction through all of these steps toward combustion. The effect of increasing the pressure is to reduce the amount of water driven off by raising the evaporation temperature, and to significantly curtail the gas-phase evidence for the decomposition of HAN. Only at the lower heating rates (less than $90^\circ C s^{-1}$) and moderate pressures (under 200 psi) can all of these decomposition steps be differentiated by the RSFTIR-thermal profiling method. As the heating rate and the pressure are increased, the time separating the steps becomes smaller. At pressures close to 1000 psi and heating rates above $150^\circ C s^{-1}$, only steps two and four can be clearly differentiated by this experimental technique. Increasing the applied pressure on the sample raises the evaporation temperature of the water, and appears to cause the temperatures at which HAN decomposes to become more similar to the TEAN-oxidizer exotherm.

We are grateful to Dr. Nathan Klein (BRL) for supplying the samples used in this study and for helpful discussions. We are pleased to acknowledge the support of the Army Research Office on DAAG29-84-K-0198.

THERMAL DECOMPOSITION OF LPG1845

89

REFERENCES

1. Cronin, J. T., and Brill, T. B., *Appl. Spectrosc.*, 41:1147 (1987).
2. Klein, N., BRL-TR-2641, Ballistic Research Laboratory, Aberdeen Proving Ground, MD (1985).
3. Oyumi, Y., and Brill, T. B., *Combust. Flame* 62:213 (1985).
4. Klein, N., in *Proceedings ICT Internationale Jahrestagung*, 167-180 (1984).
5. Norman, G., personal communication, 1986.
6. Cronin, J. T., and Brill, T. B., *J. Phys. Chem.* 90:178 (1986).
7. Rosser, W. A., Inami, S. H., and Wise, H., *J. Phys. Chem.* 67:1753 (1963).
8. Oyumi, Y., and Brill, T. B., *Combust. Flame* 68:209 (1987).
9. Birk, A., and Reeves, P., BRL-TR-2780, Ballistic Research Laboratory, Aberdeen Proving Ground, MD (1987).

Received 8 September 1987; revised 28 January 1988

20

Raman Spectroscopy of the Species
in Concentrated Aqueous Solutions of $Zn(NO_3)_2$, $Ca(NO_3)_2$,
 $Cd(NO_3)_2$, $LiNO_3$ and $NaNO_3$ up to $450^\circ C$ and 30 MPa.

Peter D. Spohn and Thomas B. Brill*
Department of Chemistry
University of Delaware
Newark, DE 19716

Abstract

The Raman spectra of aqueous $Zn(NO_3)_2$ (4.50m), $Ca(NO_3)_2$ (5.48m), $Cd(NO_3)_2$ (4.12m), $LiNO_3$ (9.42m) and $NaNO_3$ (6.82m) were recorded from $26^\circ C$ to $450^\circ C$. Selected NO_3^- band profiles were analyzed by asymmetry analysis, Fourier transformation, and curve resolution to establish the number of species and the lineshapes. The divalent cations produce two species and, like the monovalent cations, shift from the dominance of solvent separated ion pairs at lower temperatures to contact ion pairs at higher temperatures. The transition for $LiNO_3$ is not smooth, exposing the competition between the change in the dielectric constant of water and the strong associating power of Li^+ . $NaNO_3$ shows strong temperature sensitivity of the bound ion pair compared to the solvent separated ion pair. In $Zn(NO_3)_2$ and possibly $Cd(NO_3)_2$ solutions a structural change is observed at $180-200^\circ C$ suggesting a large shift in the $O_h \rightleftharpoons T_d$ equilibrium involving the cation coordination sphere. $Ca(NO_3)_2$ has a less organized and more ionic interaction sphere, while $Cd(NO_3)_2$ has the most tightly held ion pairs of the three divalent cations. No detailed general model appears to describe these salts in solution at high temperature.

Introduction

An understanding of concentrated aqueous salt solutions ($\text{H}_2\text{O}/\text{salt} < 12:1$) at high temperature is important in geochemistry and corrosion problems. However, new technological concepts, such as hazardous waste disposal in supercritical water and the combustion of aqueous liquid gun propellants, demand that more be known about the structure of salts in water at high temperature. Although thermodynamic measurements have been made on salt solutions at high temperatures¹ and extensive Raman spectroscopy has been conducted on metal nitrate solutions at room temperature², only aqueous $\text{Zn}(\text{NO}_3)_2$ appears to have been studied up to 300°C .³ Thus, little is known about associations at the molecular level in water in the high temperature regime.

To investigate this problem a Raman spectroscopy cell capable of withstanding salt solutions up to 500°C and 35 MPa was designed and constructed.⁴ Described in this paper is the Raman spectroscopy of aqueous nitrate solutions of Ca^{2+} , Zn^{2+} , Cd^{2+} , Li^+ and Na^+ from 50 to 450°C in order to describe their behavior at the molecular level. Lineshape analysis, Fourier transformations, and curve resolution are important for this study because of the broadened bands at high temperature. These analyses lead to conclusions about the general behavior of dissolved salts in aqueous solution above the critical point of pure water.

Experimental

Solutions. Metal nitrate salts were reagent grade and purchased from Aldrich, Mallinckrodt or Fisher Chemical Co. The solutions were prepared gravimetrically from triply distilled water and degassed by heating to near boiling and sealing under nitrogen. A syringe was used to extract samples. To

convert molal to molar concentrations, density measurements were made with a sample sealed in a quartz tube under vacuum and placed in a specially designed Al block.⁵ A cathetometer was used to record the height change of the meniscus at 10°C intervals from 25°C to 400°C. Pertinent parameters of the solutions are given in Table I.

Raman Spectroscopy. The Raman spectra were recorded on a Spex 1401 double monochromator spectrometer interfaced to a Nicolet 1180 computer. A Spectra Physics 4w Ar⁺ laser operating at 4880 or 5145 Å with 0.6- 1.35w power was used for excitation. Generally 10-100 scans were averaged at 2 cm⁻¹ resolution. Nine point smoothing⁶ improved the signal quality without altering the band profiles. The homebuilt cell used is described elsewhere.⁴ No decomposition or precipitation of the sample occurred up to the 450°C limit of this study.

Data Analysis and Curve Resolution. The digitized spectral data were transferred to an IBM-PC through a Metrabyte DAS-16 converter board. The contour parameters (asymmetry analysis) were calculated using an in-house program based on the product of centered Gaussian and Lorentzian functions as described by Pitha and Jones.⁷ The sum functions for the component bands were also calculated. No significant difference between the areas and peak positions was found when the product and sum functions were compared. Therefore the product functions were used. The maximum and centroid wavenumber, the semi-half bandwidth (SHBW), and incomplete second (μ_2) and third (μ_3) moments were calculated. Tables detailing the results are found in the supplementary material. Following the asymmetry analysis, fast Fourier transformation⁸ was performed to obtain phase information on ν_1 . These data were plotted using F-CURVE⁹ and LOTUS (1-2-3 and Freelance Plus). Finally, the curve resolution was performed based on the principle of sequential simplex optimization¹⁰⁻¹⁵ with modifications to accommodate Raman spectra. The

coefficient of determination(1), as well as other fit parameters, were used as a test of the fit.

$$R^2 = 1 - \frac{\sum[(y_{\text{data}} - y_{\text{curve}})^2]}{\sum[y_{\text{data}}^2]} \quad (1)$$

The curved resolved modes at each temperature (position, width, shape and area) are contained in the supplementary material.

Spectral Analysis

Zn(NO₃)₂. Spectra of NO₃⁻ salt solutions have been assigned previously.^{3,4,16-22} Raman spectra of 4.50m Zn(NO₃)₂ were recorded in the 25-375°C range at an initial pressure of 28.9±0.4 MPa. The NO₃⁻ and Zn-O regions reveal the presence of Zn-ONO₂⁺ contact ion pairs (hereafter referred to as the "bound" species) at higher temperature.^{3,4} Solvent separated ion pairs, Zn·H₂O·NO₃⁺ (hereafter referred to as the "free" species), dominate at room temperature. Assuming that the molar scattering coefficient of NO₃⁻ is constant in these solutions³, the relative concentrations can be extracted from the symmetric stretch (ν₁) or the in-plane bending mode (ν₄) of the NO₃⁻ ion. Unlike ν₄, ν₁ is singly degenerate and therefore is not complicated by the effects of reduction in symmetry upon complexation. Figure 1 shows the temperature dependence of the ν₁ mode. When the area of the bound NO₃⁻ component is divided by the total area of the ν₁ or ν₄ region at each temperature, Figure 2 suggests that the concentration of the bound species varies linearly with temperature.^{3,4} Further analysis (vide infra) reveals this not to be the case. For the salts in this study ν₁, instead of ν₄, was chosen for more detailed lineshape analysis and curve resolution because of its greater intensity and single degeneracy.

An asymmetry analysis of ν_1 was performed at 25°C intervals from 50°C to 375°C. The SHBW (Figure 3) slowly increases at a constant rate until about 180°C. Above 180°C it increases at a much faster rate. The bandwidth of each component of ν_1 is expected to increase with temperature, but major slope breaks indicate a change in the number of species or the coordination geometry.^{7,23,24} μ_2 and μ_3 indicate how the wings of the band change with temperature. Unlike μ_3 , which is zero for a symmetrical band, μ_2 has no absolute reference point. μ_2 and μ_3 were calculated at various intervals of the SHBW (j values) and did not increase with $j > 4$. A plot of μ_3 versus temperature, shown in Figure 4, indicates that a change in the structure of the solution occurs in the vicinity of 180-200°C. μ_2 exhibits similar behavior.

Curve resolution of ν_1 is complicated by the fact that the band shape changes and broadens with increasing temperature. However, Fourier transformation²²⁻²⁷ (Figure 5) provides an initial indication of the number of species and their approximate separation, position and amount. At least two components are present. In the spectrum at 50°C the phase oscillates with negative angle and low amplitude indicating that the second component has a low concentration. As T increases the amplitude of the increases and period decreases showing that the second component increases in concentration and the separation of the two components increases. Upon curve resolution the coefficient of determination of 0.999 at each temperature indicates that the ν_1 region can be accurately described by two components.

Line broadening occurs by populating higher rotational levels at higher temperature, but does not complicate the curve resolution because it causes comparable broadening in both components. Moreover, the closeness of fit of the centered product of the Gaussian and Lorentzian functions suggests that there are no anomalous changes in the wings of ν_1 .

Figure 6 shows that the energy of the solvent separated (free) species decreases linearly with increasing temperature while the contact ion pair exhibits a slope break in its energy in the 180-200°C range. Figure 7 shows the relative area of the bound component versus temperature. Contrary to previous conclusions based on fewer data points and a less rigorous analysis,^{3,4} the bound component does not increase linearly with temperature. Instead a slope break occurs in the 180-200°C region. Since no other species is present in the spectrum above 200°C, it is probable that an internal rearrangement occurs in the bound complex ion in this temperature range.

A change in the linewidth and contour of the resolved bands largely reflects changes in the vibrational relaxation with temperature. The linewidth of the bound species is approximately twice that of the free species, but both increase in width with temperature. The bound mode is 98% Lorentzian at 50°C and 38% Gaussian at 375°C. The free species is 32% Gaussian at 50°C and 100% Lorentzian at 375°C. Based on the linewidth, the bound species relaxes faster than the free species at all temperatures studied. This is attributable to perturbation of the symmetry of the NO_3^- ion by the cation which dephases the vibrational motion and causes faster relaxation. Its increasingly Gaussian character is consistent with this in that the NO_3^- ion acts more "solid-like" in the bound state.^{22,25} The free NO_3^- becomes less perturbed at elevated temperatures. This is in part because the solution density and solvent dielectric constant²⁸ decrease with increasing temperature which reduces the perturbing influence of the solvated Zn^{2+} ion. In addition, the Zn^{2+} ion is more strongly hydrated²⁹ and coordinated to NO_3^- at higher temperature giving the free NO_3^- more vibrational freedom. Hence, it relaxes more slowly and has more Lorentzian character at elevated temperature.

Ca(NO₃)₂. Raman spectra of 5.48m Ca(NO₃)₂ were collected up to 450°C with an initial pressure of 28.7±0.3 MPa. Unlike Zn(NO₃)₂, there are no Ca-O modes detected in the low wavenumber region which indicates that the degree of ionic association is greater than for aqueous Zn(NO₃)₂. The spectral changes in the ν_1 , ν_3 and ν_4 regions with temperature are also not as dramatic as with Zn(NO₃)₂⁴. These regions have been discussed extensively at room temperature as a function of concentration,^{2,18,24,30-33} where free and bound species are believed to be present. As the temperature increases, the splitting of ν_3 and the increased intensity on the low wavenumber side of ν_1 (Figure 8) both indicate enhanced Ca-ONO₂⁺ interaction.^{2,24,30} On the other hand, ν_4 is insensitive to temperature as shown in Figure 9 even though it has been used extensively before to determine the relative concentrations of species at room temperature.^{2,18,24,31-34}

An asymmetry analysis of ν_1 was performed at 25°C intervals from 25°C to 450°C. The band centroid and maximum decrease in unison with increasing temperature indicating that the asymmetry of the band is constant. μ_2 and μ_3 increase gradually with temperature. Figure 10 reveals that the SHBW increases linearly to about 160°C and then increases at a faster, but steadily changing, rate above 160°C. The spectral data do not provide clues for this behavior and no other band parameters exhibited discontinuities. However, the phase data for ν_1 at three selected temperatures (Figure 11) reveal that at least two components are present. At lower temperatures the phase oscillates to a positive angle with low intensity and has a longer period than at elevated temperature. Thus, the separation of the two components and the intensity of the second component both increase with temperature. Curve resolution of ν_1 reveals that the band is fit by two components to a coefficient of determination of 0.999 or better. A plot of the wavenumber maxima of the two

components is shown in Figure 12. A bound NO_3^- species would be expected to split ν_1 on the low wavenumber side. However, its width is similar to that of ν_1 of the free NO_3^- species indicating that there is little covalent interaction between Ca^{2+} and NO_3^- that changes the rate of the vibrational relaxation. In accordance with this, the lineshape of the bound species is approximately 100% Lorentzian at room temperature and 80% Lorentzian at 400°C. The free species is approximately 70% Lorentzian at room temperature and 100% Lorentzian at 400°C. The more Gaussian lineshape above 300°C indicates that the bound NO_3^- ion is more perturbed (polarized) of the two forms. This concurs with the increased splitting observed in ν_3 of the bound NO_3^- at higher temperature. Figure 13 shows that the concentration of bound NO_3^- increases linearly with temperature.

$\text{Cd}(\text{NO}_3)_2$. The Raman spectrum of $\text{Cd}(\text{NO}_3)_2$ has been described at room temperature as a function of concentration.²³ Presented here is the behavior of 4.12m $\text{Cd}(\text{NO}_3)_2$ from 50-400°C under an initial pressure of 29±1MPa. All of the NO_3^- fundamentals are temperature dependent. ν_1 shown in Figure 14 becomes increasingly asymmetric on the low wavenumber side, while ν_4 (Figure 15) exhibits an increase in the higher wavenumber component. Figure 16 shows that the ν_3 asymmetric stretch has two components at 1320 and 1447 cm^{-1} at 26°C. These split further to 1305 and 1468 cm^{-1} at 375°C, but their relative intensities do not change. There is intensity centered between these bands at 26°C due to the solvent separated ion pair.²³ The split components thus originate from symmetry perturbation of the bidentate oriented, bound NO_3^- ion.²³ The $\text{Cd}(\text{H}_2\text{O})_4^{2+}$ breathing mode at 350 cm^{-1} gradually shifts to lower wavenumber and diminishes in intensity with increasing temperature. All of these trends are consistent with the presence of at least two components and a greater amount of the bound NO_3^- component at higher temperatures.^{3,18,21-23,35}

18

The bound species contains the most strongly symmetry perturbed NO_3^- ion of the three divalent cations studied.

An asymmetry analysis of ν_1 shows that the peak maximum is on the high wavenumber side of the centroid and that the maximum and centroid exhibit a parallel, but slightly non-linear, decrease in wavenumber with increasing temperature. Unlike $\text{Zn}(\text{NO}_3)_2$, the SHBW of this solution gradually increases with temperature without a slope break. μ_2 is essentially unaffected by temperature while μ_3 increases up to about 225°C and then decreases again. Hence, the band contour first becomes less symmetrical and then more symmetrical up to 400°C .

The above asymmetry analysis does not clearly reveal a region where a change in the composition of the solution takes place. Fourier transformation of ν_1 shown in Figure 17 is more informative. At least two components are present. The phase oscillates to a negative angle with low intensity at 50°C . The amplitude of the oscillation increases up to about 200°C . Between 200 and 400°C the amplitude and period are similar. This information guides the curve resolution which shows that the mode is accurately fit by two components according to the coefficient of determination of 1.000. Figure 18 shows the wavenumber dependence of the maximum of the free and bound components. The position of the free component decreases in energy with increasing temperature, while the bound component increases in energy up to 125°C and then decreases in the $125\text{-}400^\circ\text{C}$ range. The lineshape of the free species is relatively constant at 52% Lorentzian over this temperature range compared to 49% in a $\text{Cd}(\text{NO}_3)_2 \cdot 12\text{H}_2\text{O}$ glass.²³ The bound component is approximately 76% Lorentzian. Paralleling the Zn^{2+} and Ca^{2+} solutions, the linewidth of the free NO_3^- component is less than that of the bound component indicating that the bound component has faster vibrational relaxation. The area of the bound component

compared to the total area of ν_1 as a function of temperature is shown in Figure 19. The bound component consumes 85% of the NO_3^- above 150°C .

LiNO_3 . Raman spectra of 9.42m LiNO_3 were recorded in the $25\text{--}445^\circ\text{C}$ range under an initial pressure of 27 ± 1 MPa. Previously, aqueous LiNO_3 has been studied as a function of concentration at room temperature.^{25,26,33} Figures 20 and 21 show the ν_1 and ν_4 regions of NO_3^- , respectively. Similar undramatic changes occur in the asymmetric stretch, ν_3 . Although the changes are not large, the spectra are consistent with increased $\text{Li}^+ \cdots \text{NO}_3^-$ association at elevated temperature. Three species have been found to be present in aqueous LiNO_3 at room temperature.^{25,26,33} These are the solvated ion, the solvent separated ion pair, and the contact ion pair. Above 7M only the latter two are present.^{25,33} The band in the 740cm^{-1} region (Figure 21) indicates that direct anion-cation contact^{3,16,18,22,36-38} is present. ν_3 is split by approximately 64cm^{-1} at all temperatures. This is only slightly greater than the 56cm^{-1} splitting predicted for LiNO_3 at infinite dilution.^{26,33} The constancy of this separation indicates that the symmetry perturbation of the NO_3^- ion is relatively independent of concentration and temperature in the presence of Li^+ .

With the above observations in mind, an asymmetry analysis was performed on ν_1 . The maximum and centroid decrease in energy with increasing temperature in a parallel fashion. The SHBW increases with upward curvature from 26 to 250°C . Above 250°C the increase is linear. Figure 22 shows the phase data from the Fourier transformation of ν_1 . At 26°C at least two components are present. The phase oscillates to a positive angle with low intensity and long period. At 200°C the phase angle is greater but the period is similar. Above 250°C the oscillation dampens until above 375°C where it is essentially zero. The increase in oscillation intensity up to 250°C indicates that the second

component is increasing in concentration. In the 250-375°C range the second component is decreasing in concentration. Above 375°C the linearity of the phase indicates that only one component is present. By curve resolution of ν_1 in the 50-375°C and 375°-445°C ranges, the coefficient of determination indicates that the mode is adequately described by two and one component, respectively. Both components decreases in wavenumber in unison with increasing temperature. The lower energy mode has been assigned previously to the solvent separated (free) ion pair, while the upper mode is the contact ion pair.^{25,26} The area of the contact ion pair compared to the total area of ν_1 is shown in Figure 23. The majority of the NO_3^- ions are in contact with Li^+ at all temperatures, but the amount decreases between 100-225°C and then increases to 100% at 375°C. The fluctuation in the concentration of this species is the result of the competition among several variables. Initially, the decrease in the density and increase in the thermal motion with temperature expands the average anion-cation separation. At some temperature, however, this factor is overridden by the decrease in the dielectric constant of the water which leads to more association between the anion and cation. Hence, the concentration of the bound species could fluctuate as observed for LiNO_3 .

NaNO_3 . Solutions of NaNO_3 as a function of concentration have been examined at room temperature.^{22,26,39} In this work a 6.82m NaNO_3 solution was studied in the 25-450°C range at an initial pressure of 30.3 ± 0.7 MPa. Figures 24 and 25 show the ν_1 and ν_4 ranges, respectively. The behavior visually resembles that of LiNO_3 , but, after detailed curve resolution, is found not to be the same. The results of the asymmetry analysis of ν_1 reveal that the maximum and centroid decrease in energy at the same rate until about 200°C where the maximum decreases at a slower rate. The SHBW is relatively constant until about 200°C, where it begins to decrease rapidly. This behavior reflects

the increasing asymmetry of ν_1 above 200°C. The Fourier transformation of ν_1 at various temperatures is shown in Figure 26. The phase data at 50°C oscillate to positive angles with low intensity and long period. The period increases until about 175°C where the phase angle is about zero indicating that only one component is resolvable. Above 225°C, at least two components are resolved again, but the phase angle is negative. Thus, the positions of the major and minor components switch as the temperature increases, but both components remain at all temperatures studied. This behavior differs from LiNO_3 .

According to the curve resolution, ν_1 is fit by two components in the 50-150°C and 225-450°C ranges and one component at 175 and 200°C where the bands overlap. Figure 27 shows the repositioning of the peak maxima. The greater temperature sensitivity of the contact ion pair is attributable to increased polarization (or directional orientation) of the bound NO_3^- compared to the free NO_3^- as the temperature is increased. At higher temperature the lower the dielectric constant of H_2O allows NO_3^- to compete more effectively with H_2O for coordination sites on the Na^+ ion. Hence, it is more polarized at high temperature. There is also an increase in the concentration of the bound species with temperature. Because of the stronger coupling of the ions, the vibrational relaxation of the bound NO_3^- ion increases with temperature giving rise to a large increase in the linewidth with temperature.

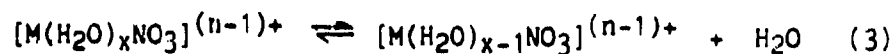
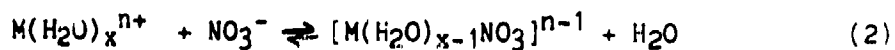
Discussion

In all of the salts studied in this work, the bound (contact ion pair) NO_3^- has a greater linewidth than the free (solvent separated) NO_3^- . This is consistent with the expectation that the bound species will have faster vibrational relaxation owing to its greater degree of polarization. Likewise, the increasingly Gaussian character of the bound species and increasingly

Lorentzian character of the free species at higher temperatures are consistent with the degrees of interaction with the cation expected for these forms of NO_3^- . This pattern also provides confidence that the vibrational modes are properly assigned to these ions.

In previous work^{3,40} it has been assumed that the Raman intensity is proportional to the concentration of the two NO_3^- species (C_{free} and C_{bound}) resolved from ν_1 . The degree of association, $\alpha(\text{bound}) = (1 - C_{\text{bound}})/C_{\text{total}}$, can thus be determined as a function of the molar concentration (calculated from Table I) as the temperature is increased. The results are shown in Figure 28. The general pattern of decreasing $\alpha(\text{bound})$ with increasing concentration is opposite what is observed^{33,41-43} as the concentration is increased at constant temperature. Changes in the molar concentration that are produced by increasing the temperature are clearly overridden by the decrease in the dielectric constant of water.

Apparent enthalpy and entropy values can be extracted from mass law equilibrium quotients by the van't Hoff equation for various models of these solutions.⁵ However, insight beyond the above comments indicates only that the outer sphere-inner sphere equilibrium (2) and the free-bound equilibrium (3) give linear plots.



For the divalent cations studied, reaction (2) gives the most broadly satisfactory description of the temperature dependence of the Raman spectra. The composition progresses from predominately solvent separated ion pairs at room temperature to predominately contact ion pairs at high temperature.

Octahedral \rightleftharpoons tetrahedral rearrangements that are known to occur with various ions at temperatures above 180°C⁴⁴⁻⁴⁷ are a plausible explanation for the slope breaks in the Cd²⁺ and Zn²⁺ data, but further details are not ascertainable from the spectra. That Ca²⁺ is less strongly hydrated than Zn²⁺ and Cd²⁺⁴⁸ is evident by the absence of modes attributable to Ca(H₂O)₆²⁺ in the Raman spectrum. Hence, reactions (2) and (3) may be competitive in the Ca(NO₃)₂ solution. There are no slope breaks in the Ca(NO₃)₂ data. Likewise, NaNO₃ has a less organized and less tightly held second coordination sphere making reaction (3) the most suitable description. LiNO₃ appears to be a special case as a result of the large hydration energy of Li⁺ and its ability to organize a second and third coordination sphere.⁴⁸ The competition between this factor, the change in the dielectric constant of water with temperature, and the ion mobility leads to complex competitive effects in the structure of the solution species. However, for both NaNO₃ and LiNO₃ there is a pattern of increasing presence (although not linearly in the case of LiNO₃) of contact ion pairs and a decreasing presence of solvent separated ion pairs as the temperature is increased. In addition, the strength of the anion-cation interaction in the contact ion pairs increases with temperature. Although each salt has its own special characteristics, this broad behavior is evident in all of the salts studied.

Supplementary Material

Tables giving the peak and centroid maxima, SHBW, and incomplete second and third moments for each salt as a function of temperature; tables giving the curve resolved position, width, shape, area, and R² values for ν_1 of each salt (11 pages). Ordering information is given on any current masthead page.

Acknowledgments

We are grateful to the U. S. Army Research Office for financial support on DAAG20-84-K-0198. Helpful discussions on various aspects of this work with R. H. Wood, J. H. Noggle, and S. D. Brown were most appreciated.

References

1. For example see Majer, V.; Gates, J.A.; Inglese, A.; Wood, R.H. J. Chem. Thermodynamics, 1987, 20, 2159. Tanger, J.C.; Helgeson, H.C., Am. J. Science, 1988, 288, 19. Pitzer, K.S.; Bischoff, J.L.; Rosenbauer, R.J. Chem. Phys. Letters, 1987, 60, 134. Marshall, W.L. Pure and Appl. Chem. 1985, 57, 283.
2. For a review, see Irish, D.E.; Brooker, M.H. in Advances in Infrared and Raman Spectroscopy, Vol. 2, Chapter 6, Clark, R.J.H. and Hester, R.E. Eds. Heyden, London, 1976.
3. Irish, D.E.; Jarv, T. Appl. Spectrosc. 1983, 37, 50.
4. Spohn, P.D.; Brill, T.B. Appl. Spectrosc. 1987, 41, 1152.
5. Spohn, P.D. Ph.D Dissertation, University of Delaware, Dec. 1988.
6. Savitsky, A.; Golay, M.J.E. Anal. Chem. 1964, 36, 1127.
7. Pitha, J.; Jones, R.N. Can. Spectry, 1966, 11, 14; Can. J. Chem., 1966, 44, 3031.
8. Noggle, J.N. Personal Communication, University of Delaware, 1986.
9. Noggle, J.N. Program F-CURVE (LEDS Publishing Co.), 1986.
10. Nelder, J.A.; Mead, R. Comput. J. 1965, 7, 308.
11. O'Neill, R. Appl. Statistics, 1971, 13, 338.
12. Toman, J.J.; Brown, S.D. Anal. Chem., 1981, 53, 1497.
13. Chambers, J.M.; Ertel, J.E. Appl. Statistics, 1974, 23, 250.
14. Benyon, P.R. Appl. Statistics, 1976, 25, 97.
15. Hill, I.D. Appl. Statistics, 1978, 27, 380.
16. Jones, R.N.; Seshadri, K.S.; Jonathan, N.B.W.; Hopkins, J.W. Can. J. Chem. 1963, 41, 750.
17. Davies, A.R.; Irish, D.E. Inorg. Chem. 1968, 7, 1699.

18. Irish, D.E.; Davies, A.R.; Plane, R.A. J. Chem. Phys. 1969, 50, 2262.
19. Bulmer, J.T.; Irish, D.E.; Odberg, L. Can. J. Chem. 1975, 53, 3806.
20. Jarv, T.; Bulmer, J.T.; Irish, D.E. J. Phys. Chem., 1977, 81, 649.
21. Sze, Y-K.; Irish, D.E. J. Solution Chem. 1978, 8, 395.
22. Frost, R.L.; James, D.W. J. Chem. Soc. Farad. Trans. I, 1982, 78, 3223.
23. Carrick, M.T.; James, D.W. and Leong, W.H. Aust. J. Chem. 1983, 36, 223.
24. James, D.W.; Frost, R.L. Aust. J. Chem. 1982, 35, 1793.
25. Frost, R.L.; James, D.W. J. Chem. Soc. Farad. Trans. I, 1982, 78, 3235.
26. Frost, R.L.; Appleby, R.; Carrick, M.T.; James, D.W. Can. J. Spectrosc. 1982, 27, 82.
27. James, D.W.; Carrick, M.T.; Frost, R.L. J. Raman Spectrosc. 1982, 13, 115.
28. Heger, K.; Uematsu, M.; Franck, E.U. Ber. Bunsenges. Phys. Chem., 1980, 84, 758.
29. Franck, E.U. in "Phase Equilibria and Fluid Properties in Chemical Industry" Storvick, T.S.; Sandler, S.I. Eds. ACS Symp. Series 60, 1977, p99.
30. James, D.W.; Armishaw, R.F. Frost, R.L. Aust. J. Chem. 1982, 31, 1401.
31. Hester, R.E.; Plane, R.A. J. Chem. Phys. 1964, 40, 411.
32. Balshaw, B.; Smedley, S.I. J. Phys. Chem. 1975, 79, 1323.
33. Irish, D.E.; Davies, A.R. Can J. Chem. 1968, 46, 943.
34. Irish, D.E.; Chang, G.; Nelson, D.L. Inorg. Chem. 1970, 9, 425.
35. Davies, A.R.; Plane, R.A. Inorg. Chem. 1986, 7, 2565.
36. Irish, D.E.; Walrafen, G.E. J. Chem. Phys. 1967, 46, 378.
37. Miller, J.T.; Irish, D.E. Can. J. Chem. 1967, 45, 147.
38. Hester, R.E.; Krishnan, K. J. Chem. Phys. 1967, 46, 3405.
39. Vollmer, P.M. J. Chem. Phys. 1963, 39, 2236.
40. Janz, G.T.; Muller, M.A. J. Solution Chem. 1975, 4, 285.

41. Sze Y-K.; Irish, D.E. J. Solution Chem. 1978, 7, 417.
42. Carpio, R.; Mehicic, M.; Borsay, F.; Petrovic, C.; Yeager, E. J. Phys. Chem. 1982, 86, 4980.
43. Riddell, J.D.; Lockwood, D.J.; Irish, D.E. Can. J. Chem. 1972, 50, 2951.
44. Angell, C.A.; Gruen, D.M. J. Am. Chem. Soc. 1966, 88, 5192.
45. Ludemann, H.-D.; Franck, E.U. Ber. Bunsenges. Phys. Chem. 1968, 72, 514.
46. Scholz, B.; Ludemann, H.-D.; Franck, E.U. Ber. Bunsenges. Phys. Chem., 1972, 76, 406.
47. Swaddle, T.W.; Fabes, L. Can. J. Chem. 1980, 58, 1418.
48. Horne, R.A. Water and Aqueous Solutions, Wiley Interscience, NY, 1972

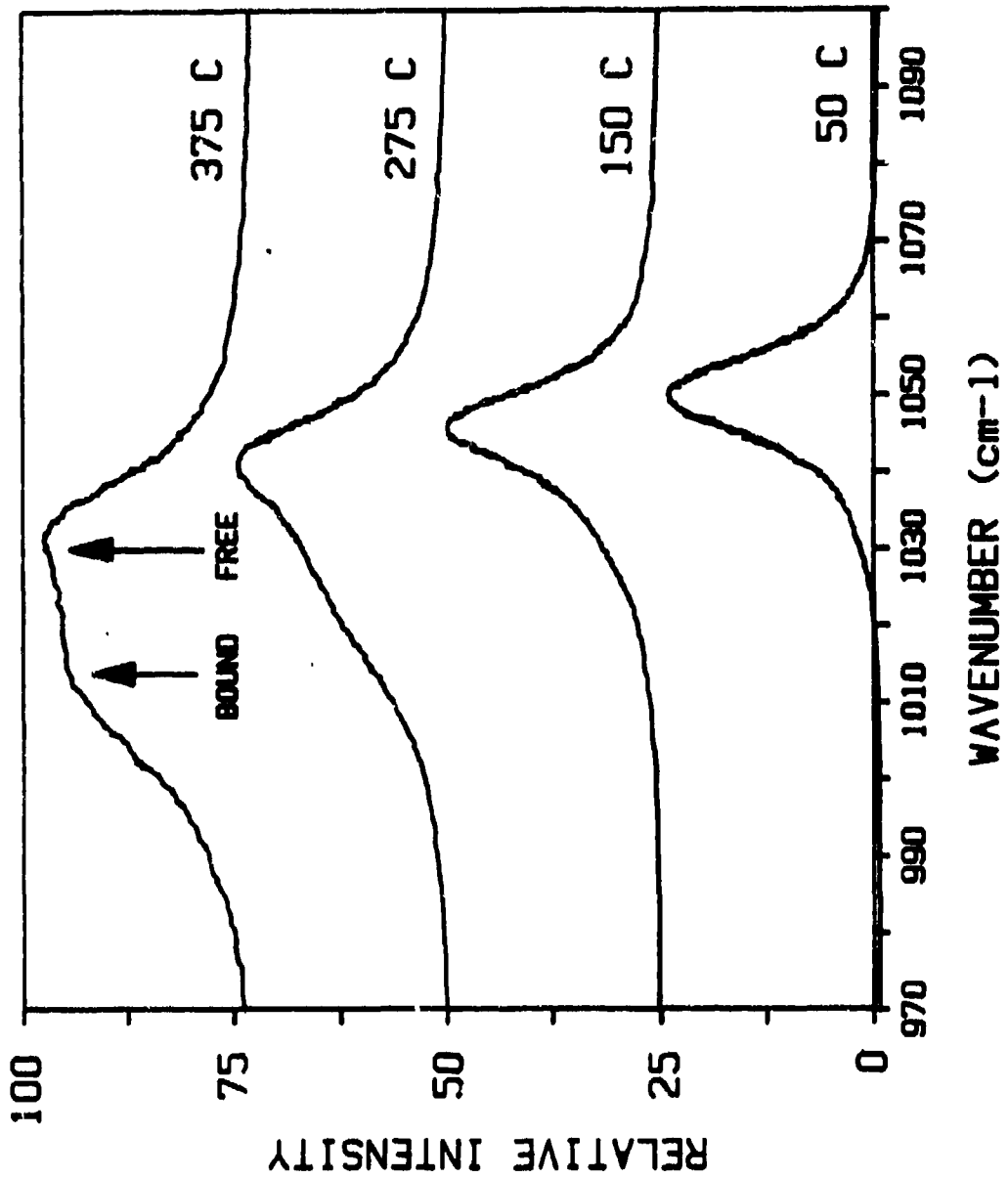
Table I: The Molal Concentration, Initial Density (25°C) and Temperature Dependence of the Density in the 25-375°C Range.

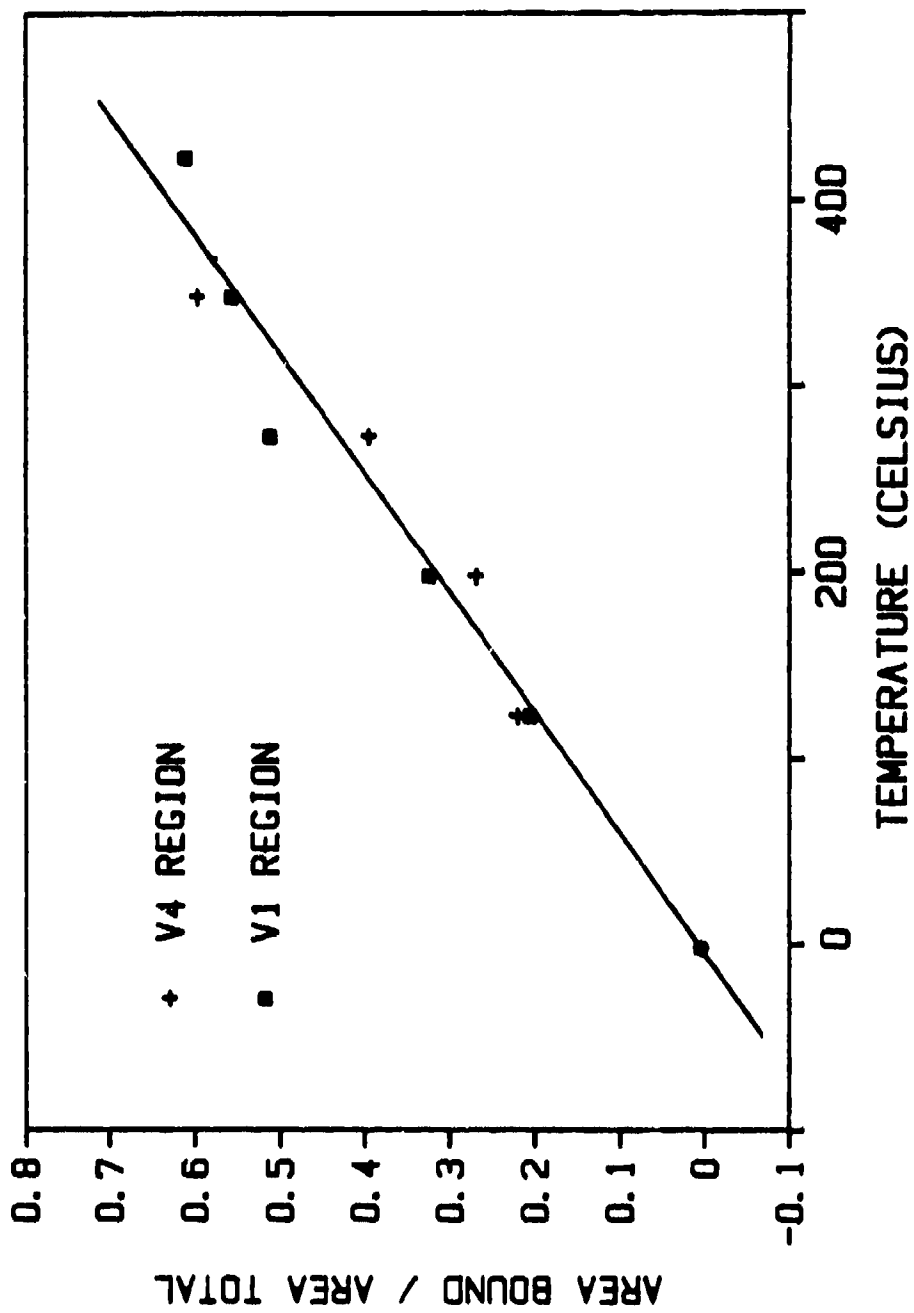
<u>Solution</u>	<u>Conc., m</u>	<u>ρ, gm cc⁻¹ 25°C</u>	<u>$\frac{d\rho}{dT}$, gm cc⁻¹ K⁻¹</u>
Zn(NO ₃) ₂	4.50±0.02	1.651	-1.023 x 10 ⁻³
Ca(NO ₃) ₂	5.48±0.02	1.542	-6.615 x 10 ⁻⁴
Cd(NO ₃) ₂	4.12±0.02	1.720	-6.848 x 10 ⁻⁴
LiNO ₃	9.42±0.02	1.280	-6.738 x 10 ⁻⁴
NaNO ₃	6.82±0.02	1.380	-6.960 x 10 ⁻⁴

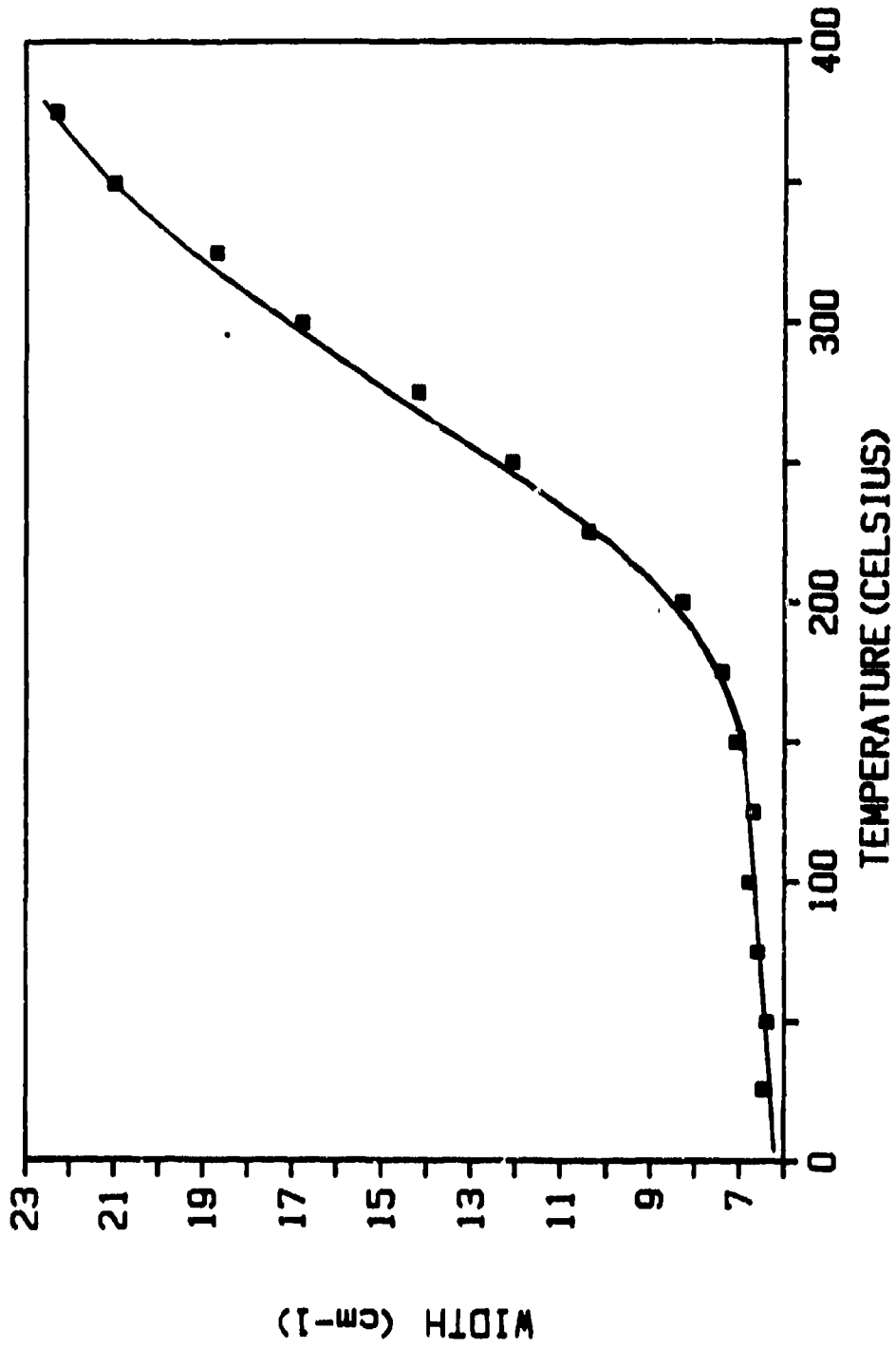
Figure Captions

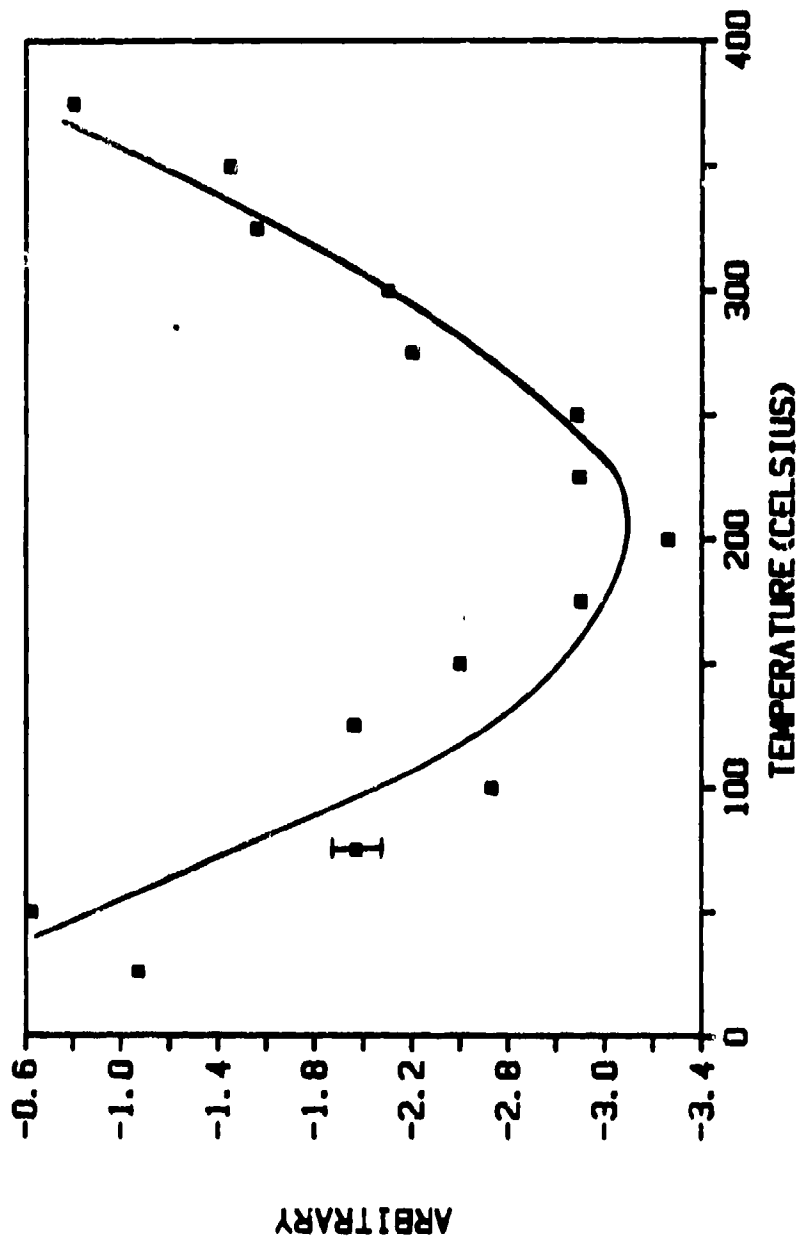
- Figure 1. Selected spectra of ν_1 (NO_3^-) in 4.50m $\text{Zn}(\text{NO}_3)_2$ showing the increase in the concentration of the contact ion pair (bound species) with temperature.
- Figure 2. The relative area of the bound NO_3^- in 4.50m $\text{Zn}(\text{NO}_3)_2$ as a function of temperature evaluated from the ν_1 and ν_4 regions of NO_3^- .
- Figure 3. The SHBW of ν_1 (NO_3^-) in 4.50m $\text{Zn}(\text{NO}_3)_2$ showing a probable structural change in the ionic interactions in the 180-200°C range.
- Figure 4. The incomplete third moment ($j=4$) of ν_1 in 4.50m $\text{Zn}(\text{NO}_3)_2$ showing the lineshape change in the 180-200°C range. The representative error in the plot is shown on one data point.
- Figure 5. Phase data from the Fourier transformation of ν_1 of 4.50m $\text{Zn}(\text{NO}_3)_2$ at three temperatures.
- Figure 6. The band maxima of the free and bound NO_3^- species from curve resolution of ν_1 in 4.50m $\text{Zn}(\text{NO}_3)_2$.
- Figure 7. The relative area of the bound species after curve resolution of ν_1 in 4.50m $\text{Zn}(\text{NO}_3)_2$.
- Figure 8. The temperature dependence of ν_1 (NO_3^-) in 5.48m $\text{Ca}(\text{NO}_3)_2$.
- Figure 9. The relative contribution of the bound component in 5.48m $\text{Ca}(\text{NO}_3)_2$ evaluated in the ν_1 and ν_4 regions. The ν_4 region is not sensitive to the change in composition and, therefore, cannot be used to evaluate the temperature dependence.
- Figure 10. The SHBW of ν_1 of 5.48m $\text{Ca}(\text{NO}_3)_2$ including the representative error on one data point. A subtle composition change may occur in the vicinity of 160°C.
- Figure 11. Phase data from the Fourier transformation of ν_1 of 5.48m $\text{Ca}(\text{NO}_3)_2$.
- Figure 12. Band maxima of the free and bound components of ν_1 in 5.48m $\text{Ca}(\text{NO}_3)_2$ from curve resolution.
- Figure 13. The relative concentration of bound NO_3^- as function of temperature in 5.48m $\text{Ca}(\text{NO}_3)_2$.
- Figure 14. The temperature dependence of $\nu_1(\text{NO}_3^-)$ in 4.12m $\text{Cd}(\text{NO}_3)_2$.
- Figure 15. The temperature dependence of $\nu_4(\text{NO}_3^-)$ in 4.12m $\text{Cd}(\text{NO}_3)_2$ showing the increased contribution of bound NO_3^- in the high wavenumber side.

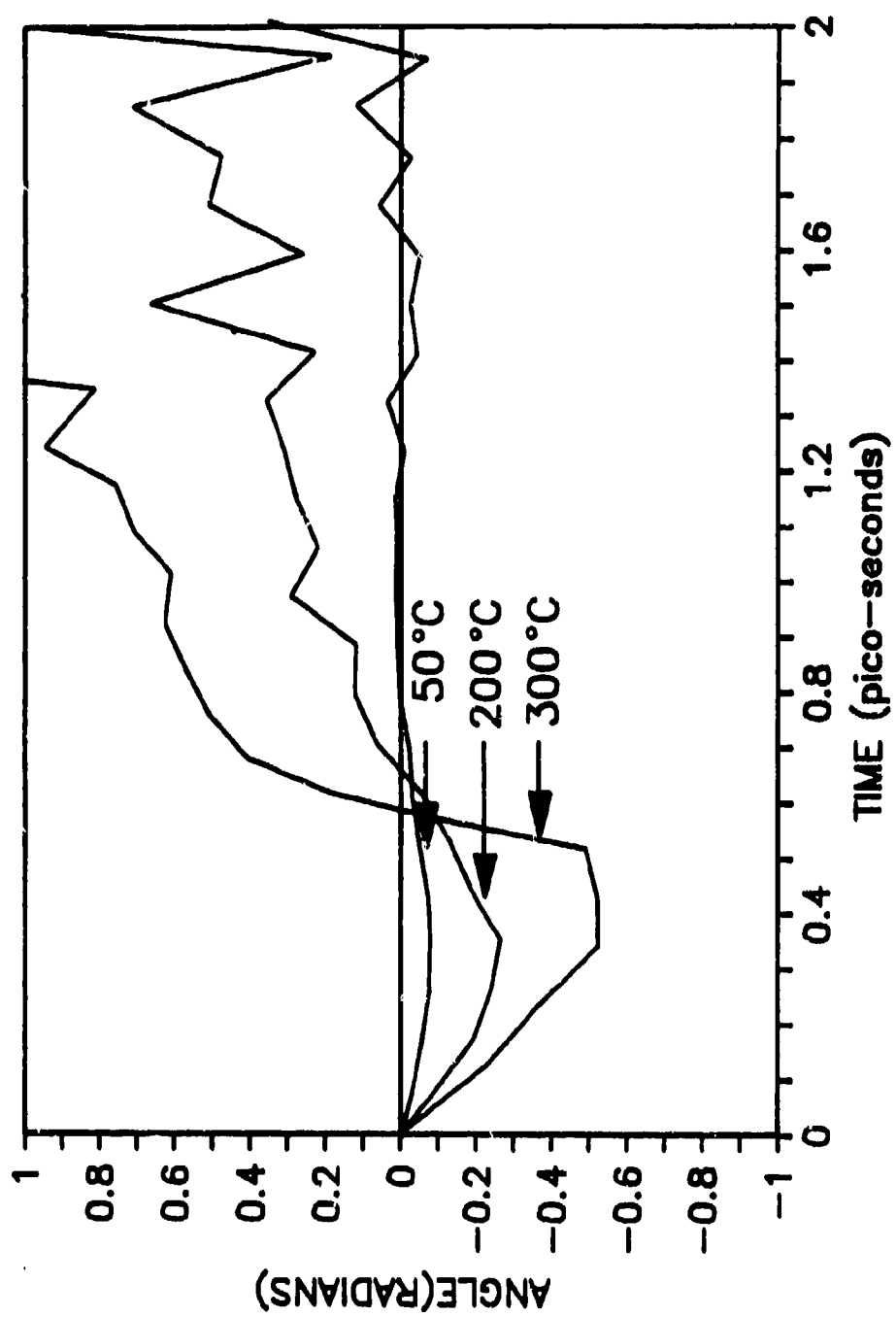
- Figure 16. The temperature dependence of the $\nu_3(\text{NO}_3^-)$ mode in 4.12m $\text{Cd}(\text{NO}_3)_2$ showing the predominate change in the line splitting.
- Figure 17. Selected phase data from the Fourier transformation of ν_1 of 4.12m $\text{Cd}(\text{NO}_3)_2$.
- Figure 18. Maxima of the bound and free NO_3^- components curve resolved from ν_1 of 4.12m $\text{Cd}(\text{NO}_3)_2$.
- Figure 19. The relative area of the bound component of ν_1 after curve resolution of 4.12m $\text{Cd}(\text{NO}_3)_2$.
- Figure 20. The temperature dependence of $\nu_1(\text{NO}_3^-)$ of 9.42m LiNO_3 .
- Figure 21. The temperature dependence of $\nu_4(\text{NO}_3^-)$ of 9.42m LiNO_3 .
- Figure 22. Selected phase data from the Fourier transformation of ν_1 of 9.42m LiNO_3 .
- Figure 23. The relative concentration of the bound NO_3^- from curve resolution of ν_1 of 9.42m LiNO_3 .
- Figure 24. The temperature dependence of $\nu_1(\text{NO}_3^-)$ of 6.82m NaNO_3 .
- Figure 25. The temperature dependence of $\nu_4(\text{NO}_3^-)$ of 6.82m NaNO_3 showing the increased contribution of the bound component on the high wavenumber side.
- Figure 26. Phase data at selected temperatures from ν_1 in 6.82m NaNO_3 .
- Figure 27. Band maxima from curve resolution of ν_1 in 6.82m NaNO_3 showing representative errors on selected data points.
- Figure 28. The variation in the degree of association, $\alpha(\text{bound})$, with the change in concentration induced by the change in temperature.

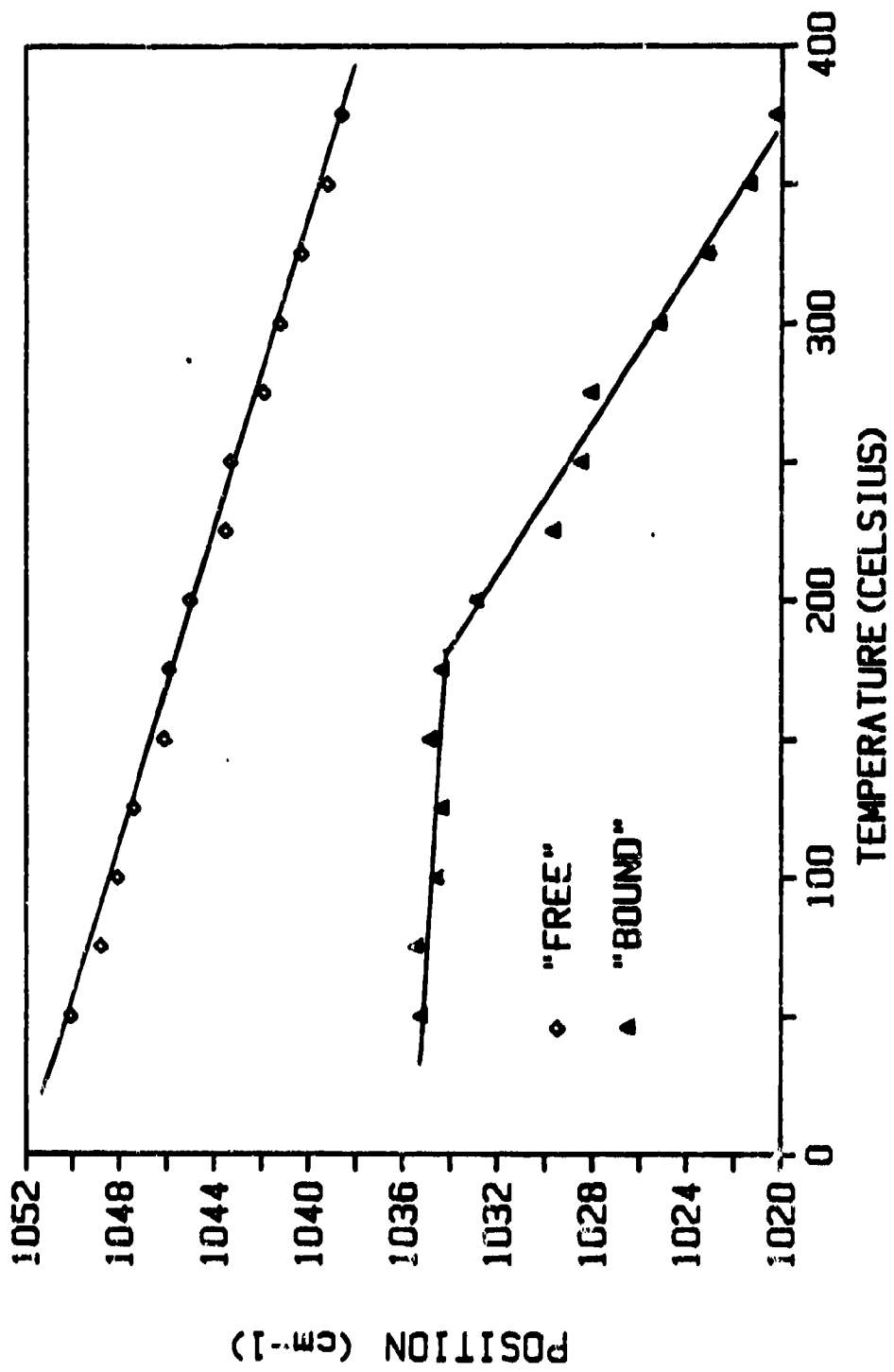


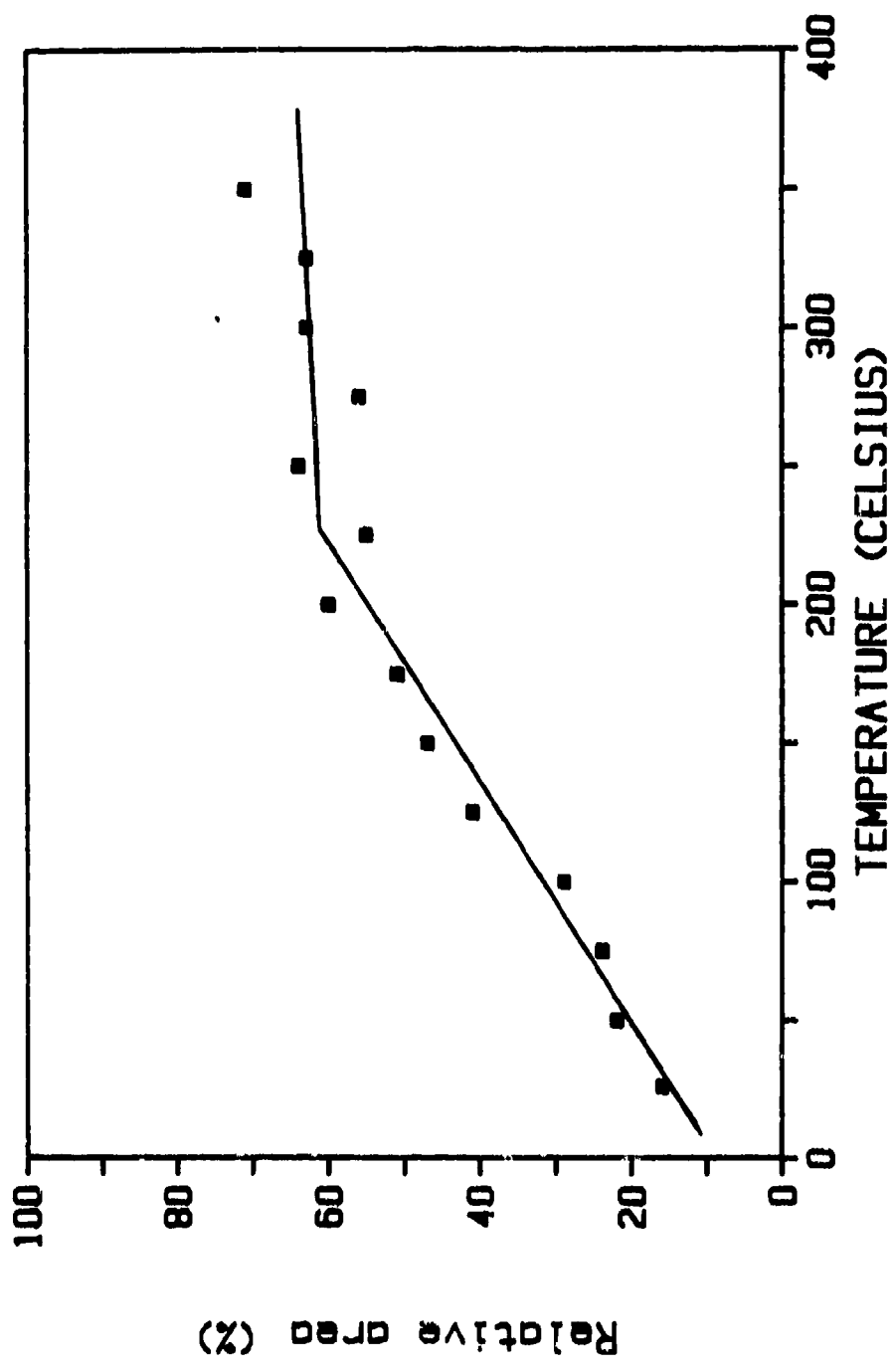


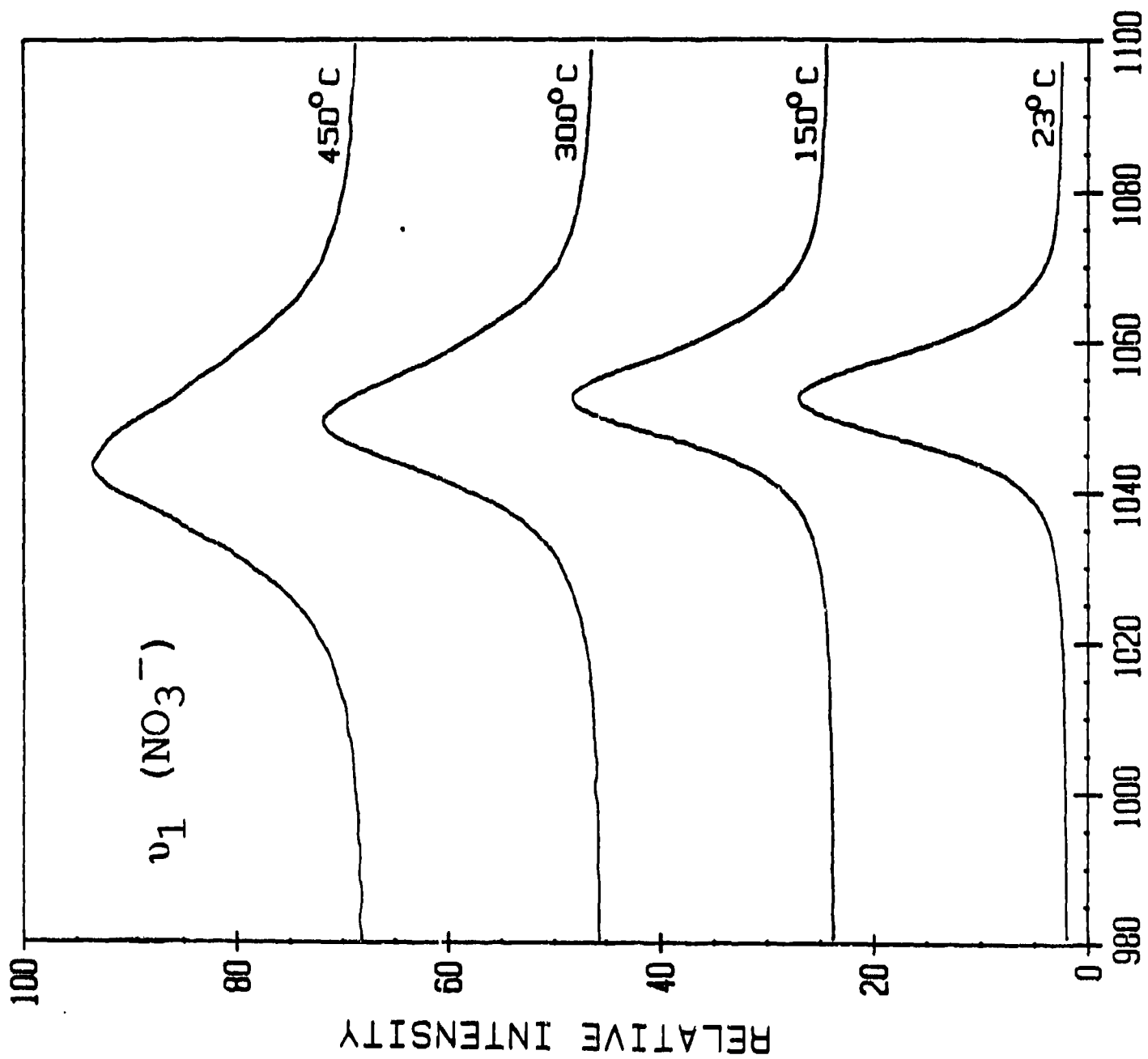




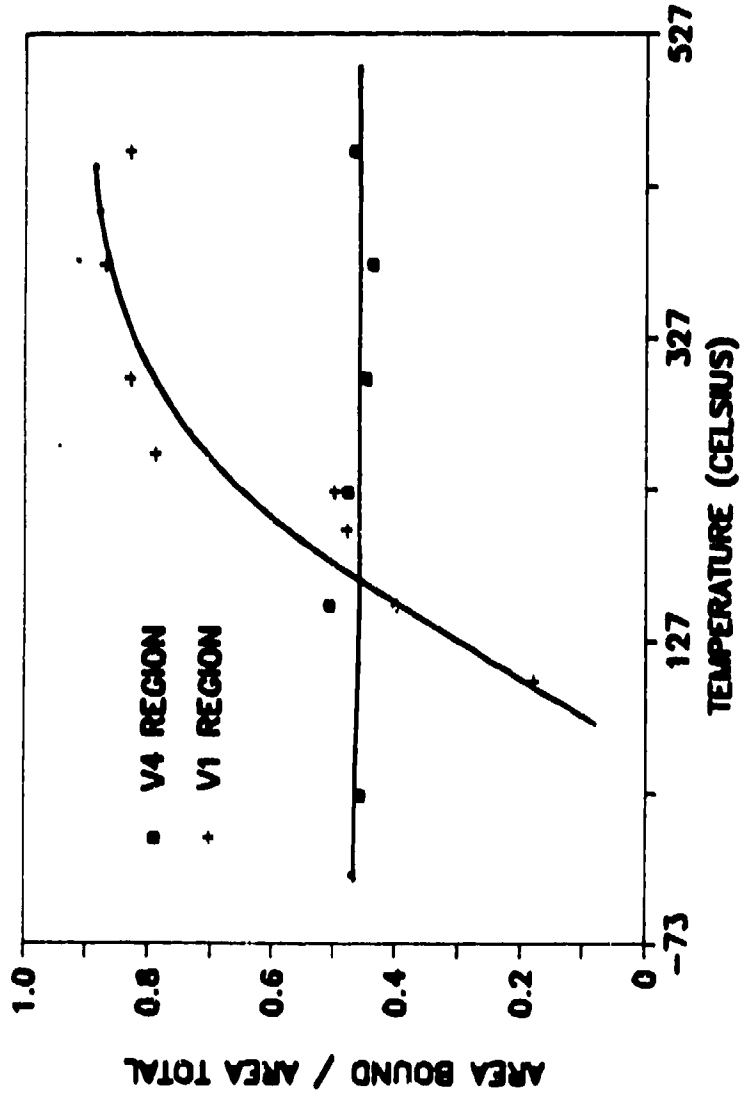


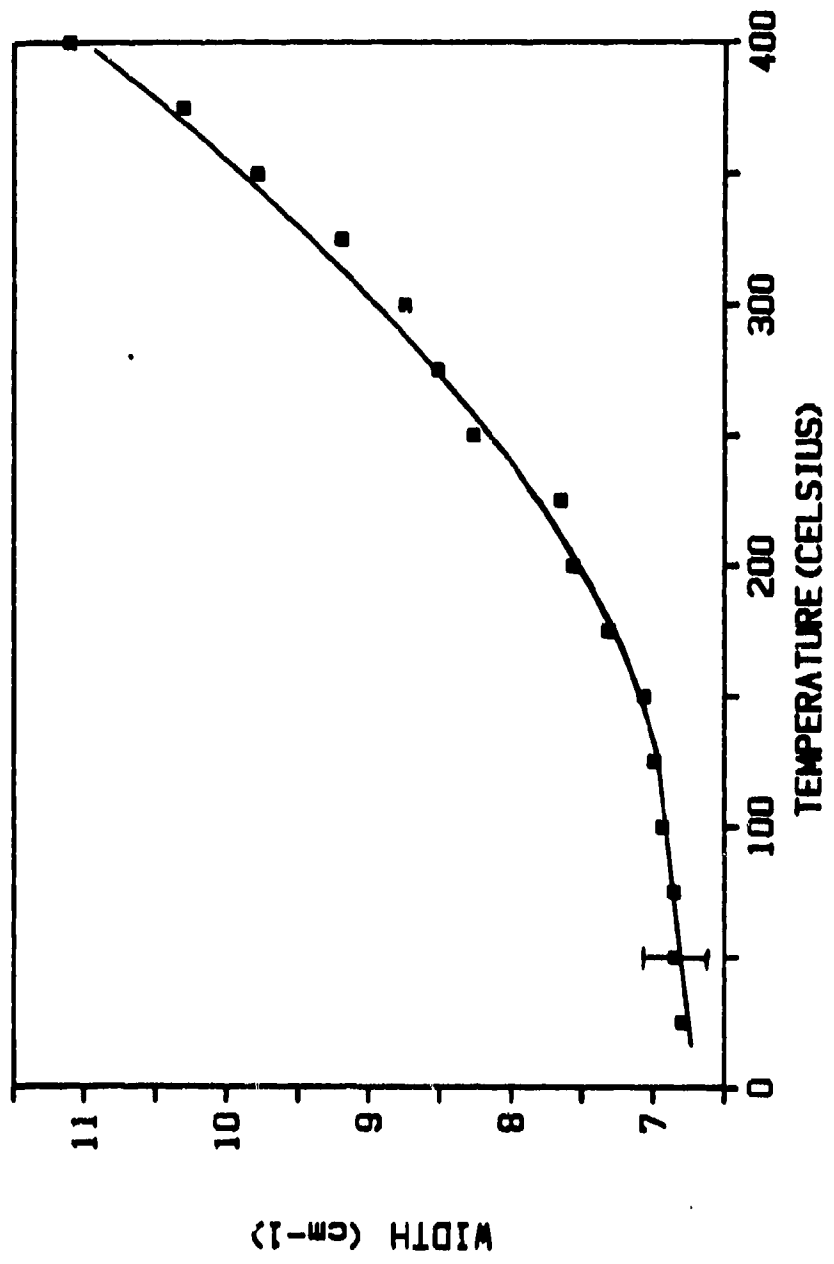


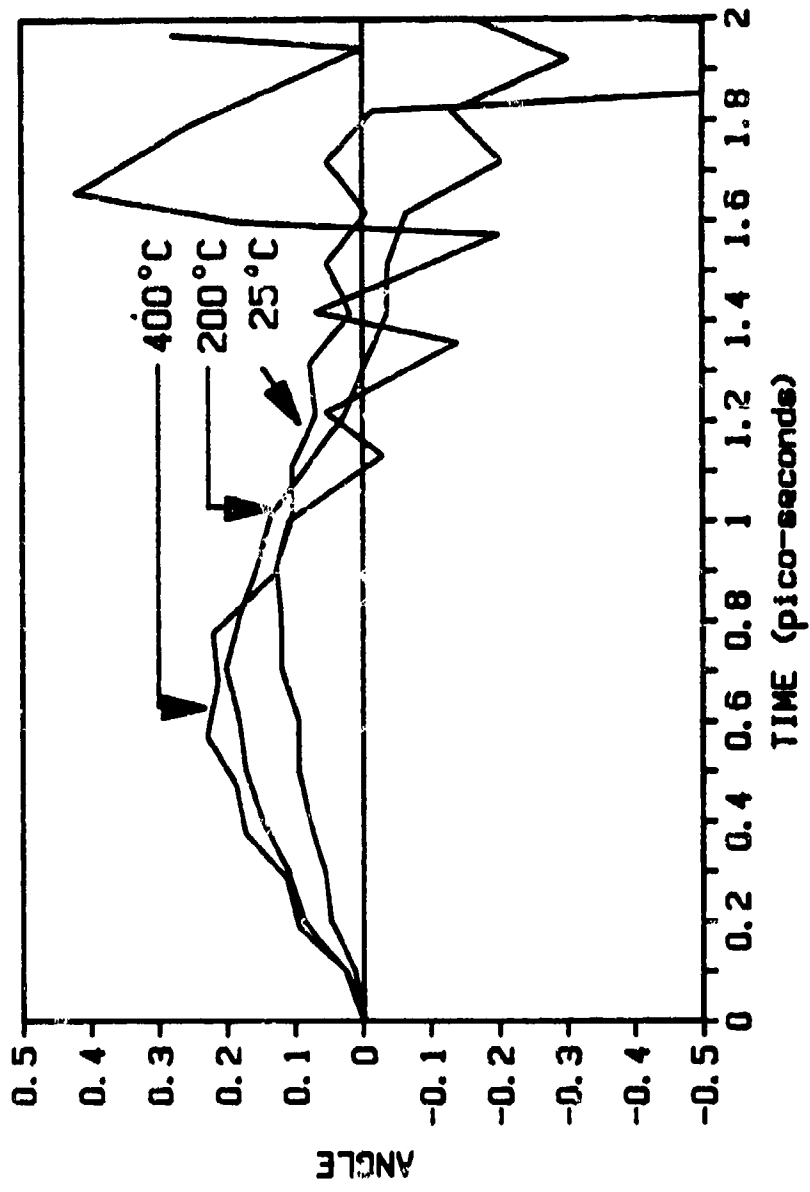


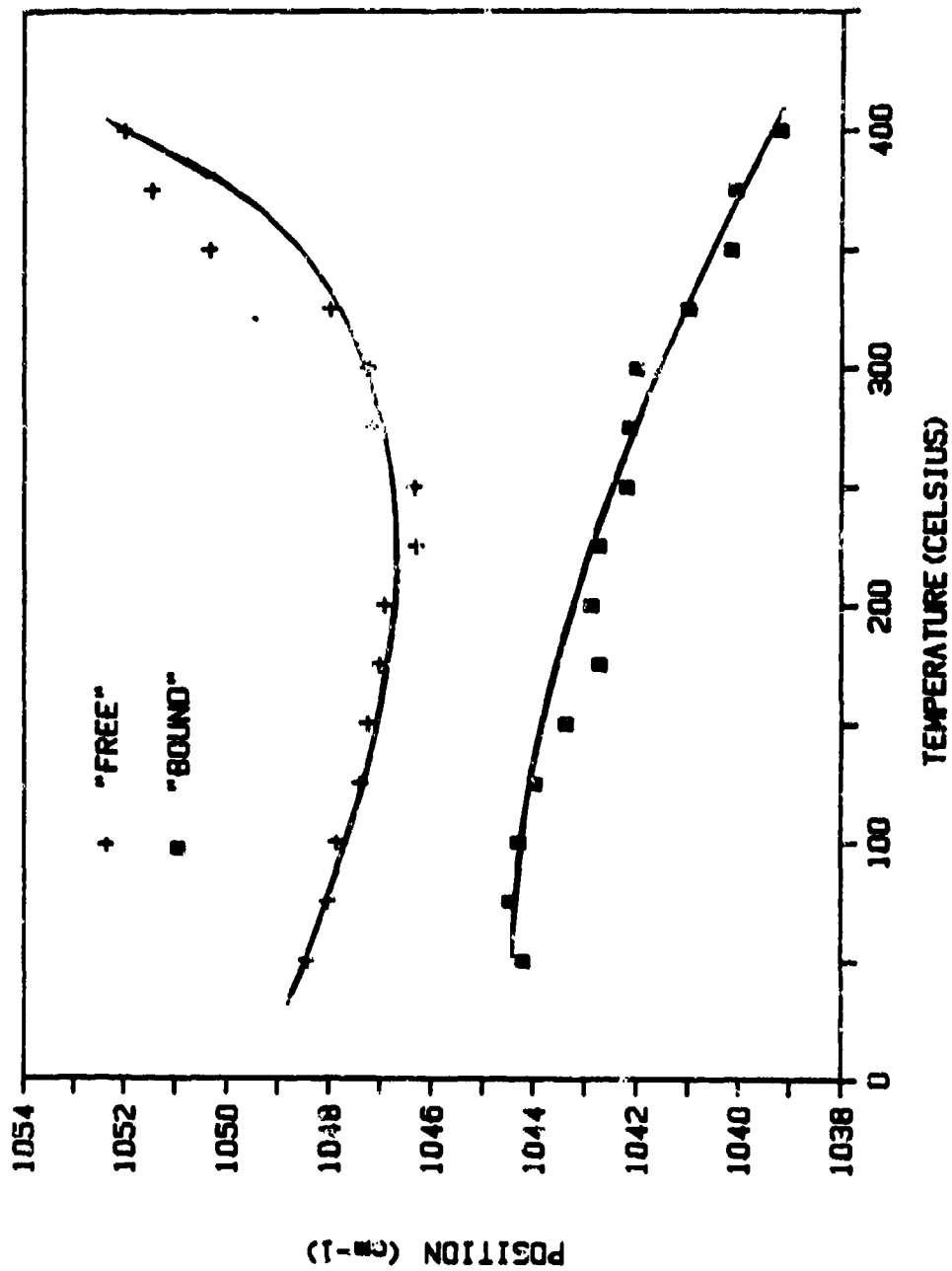


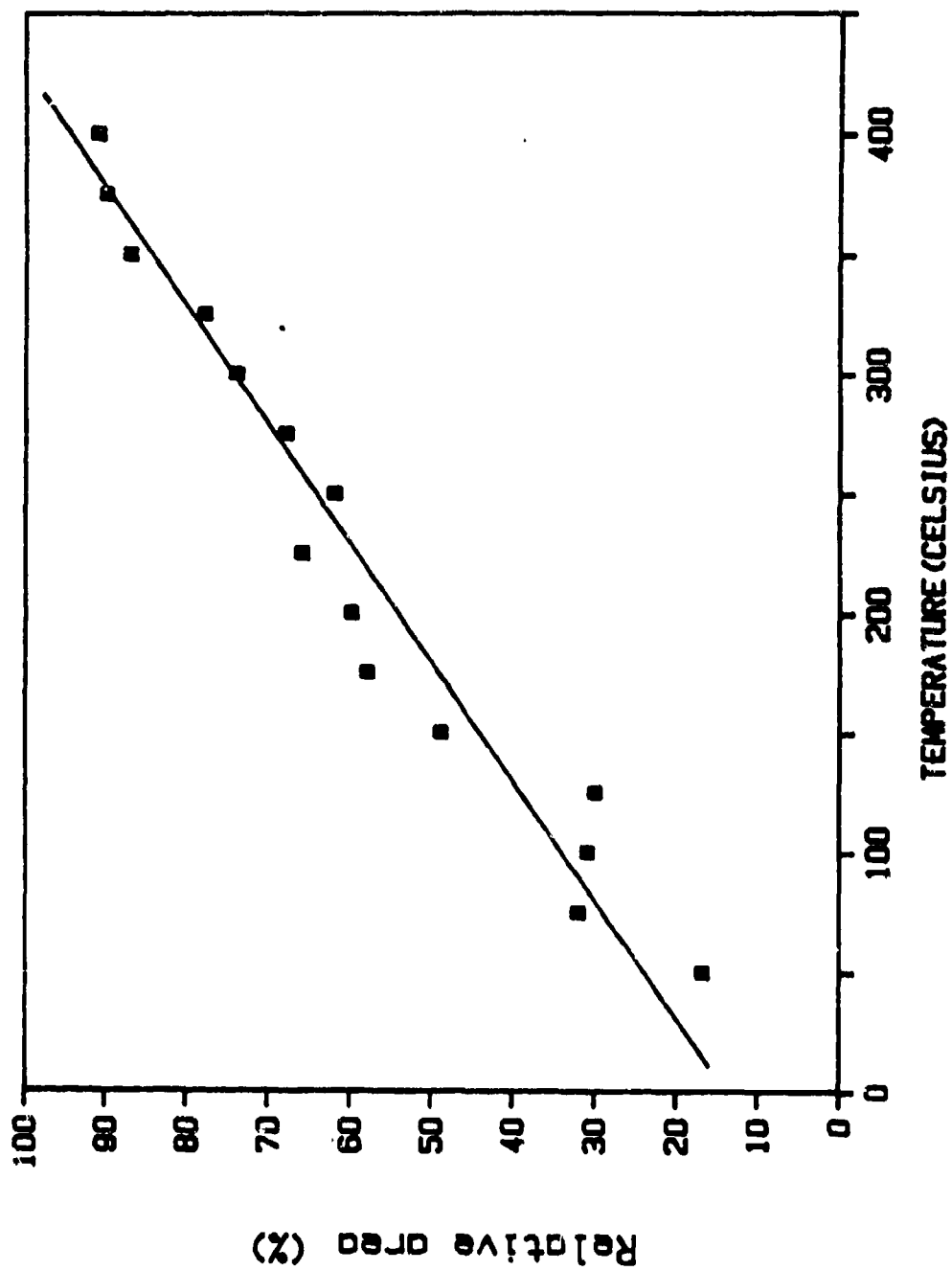
WAVENUMBER (cm⁻¹)

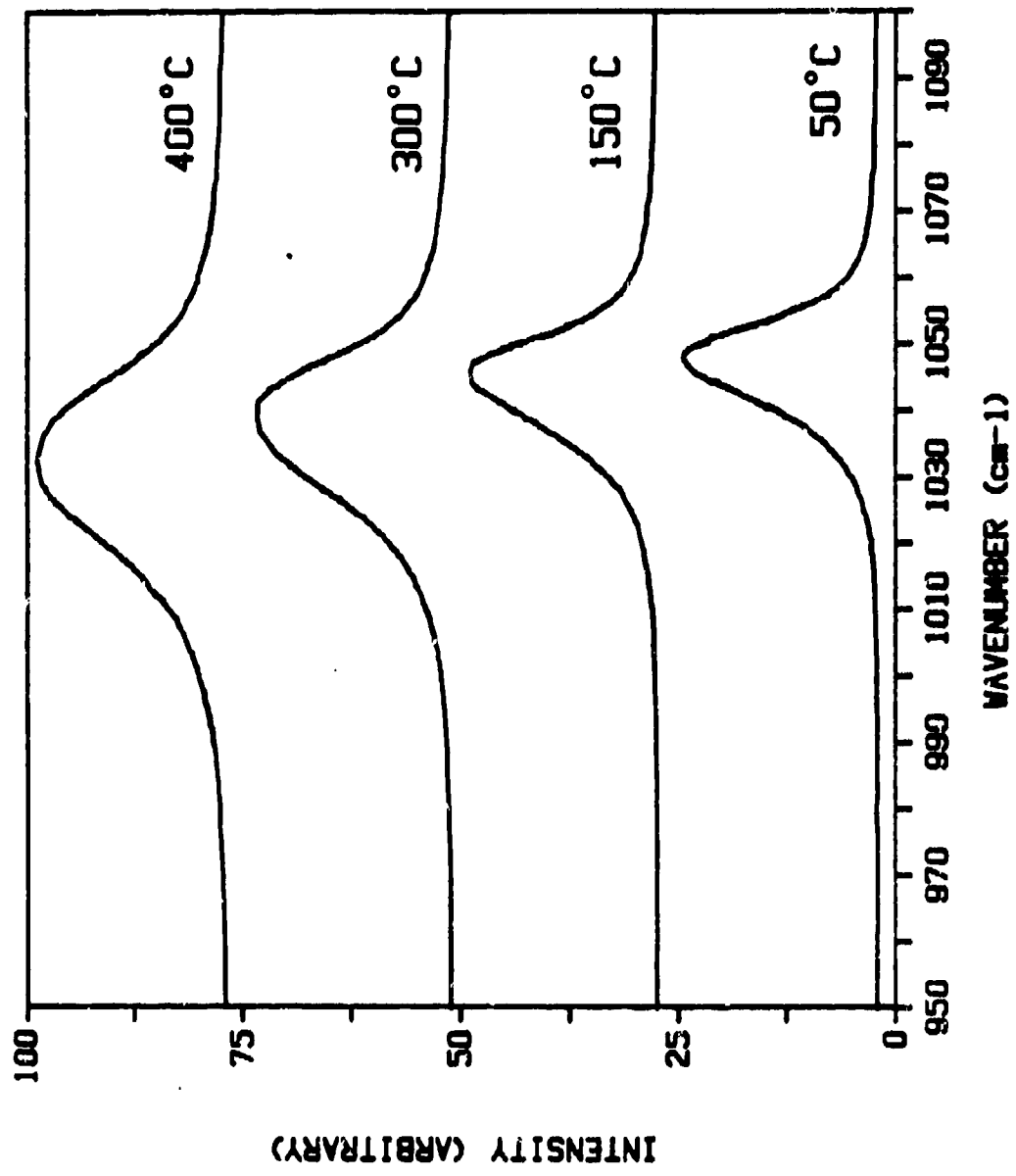


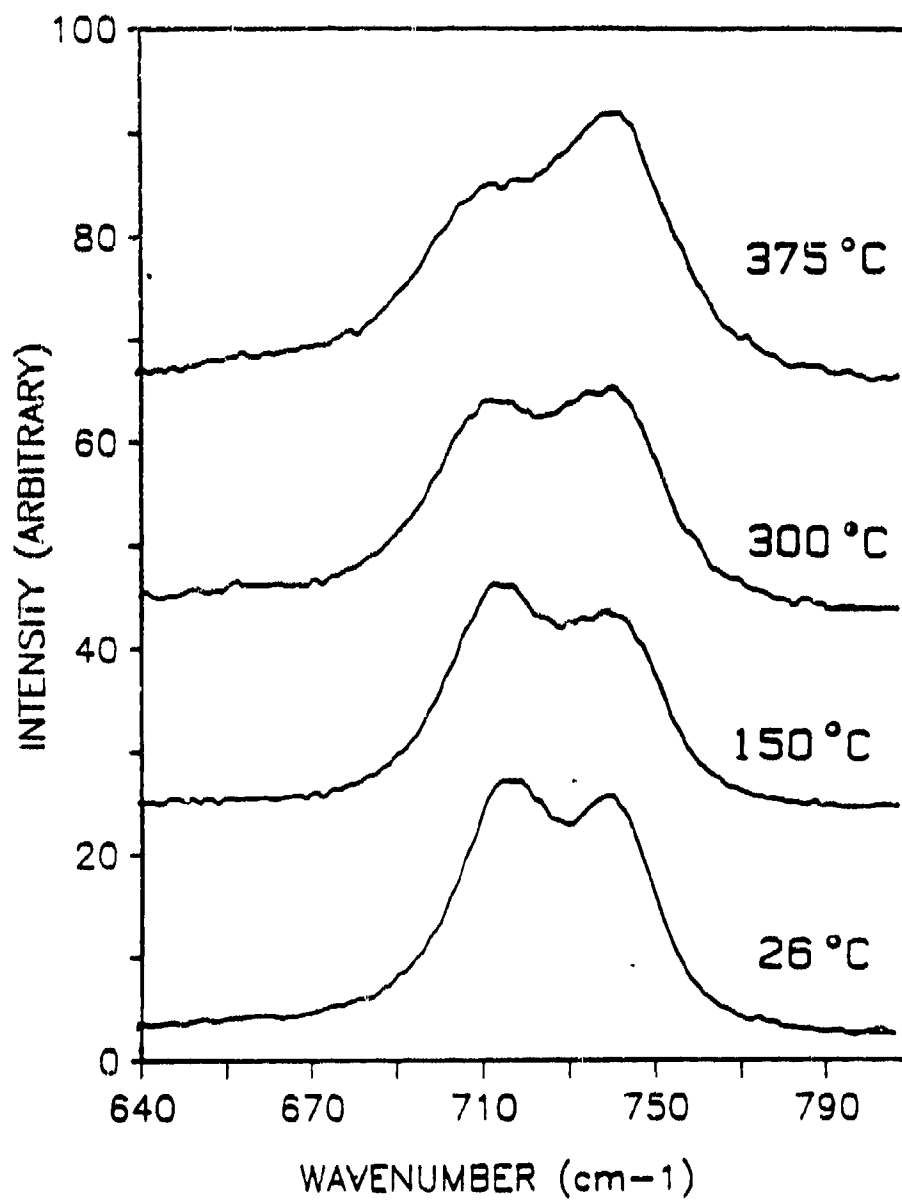


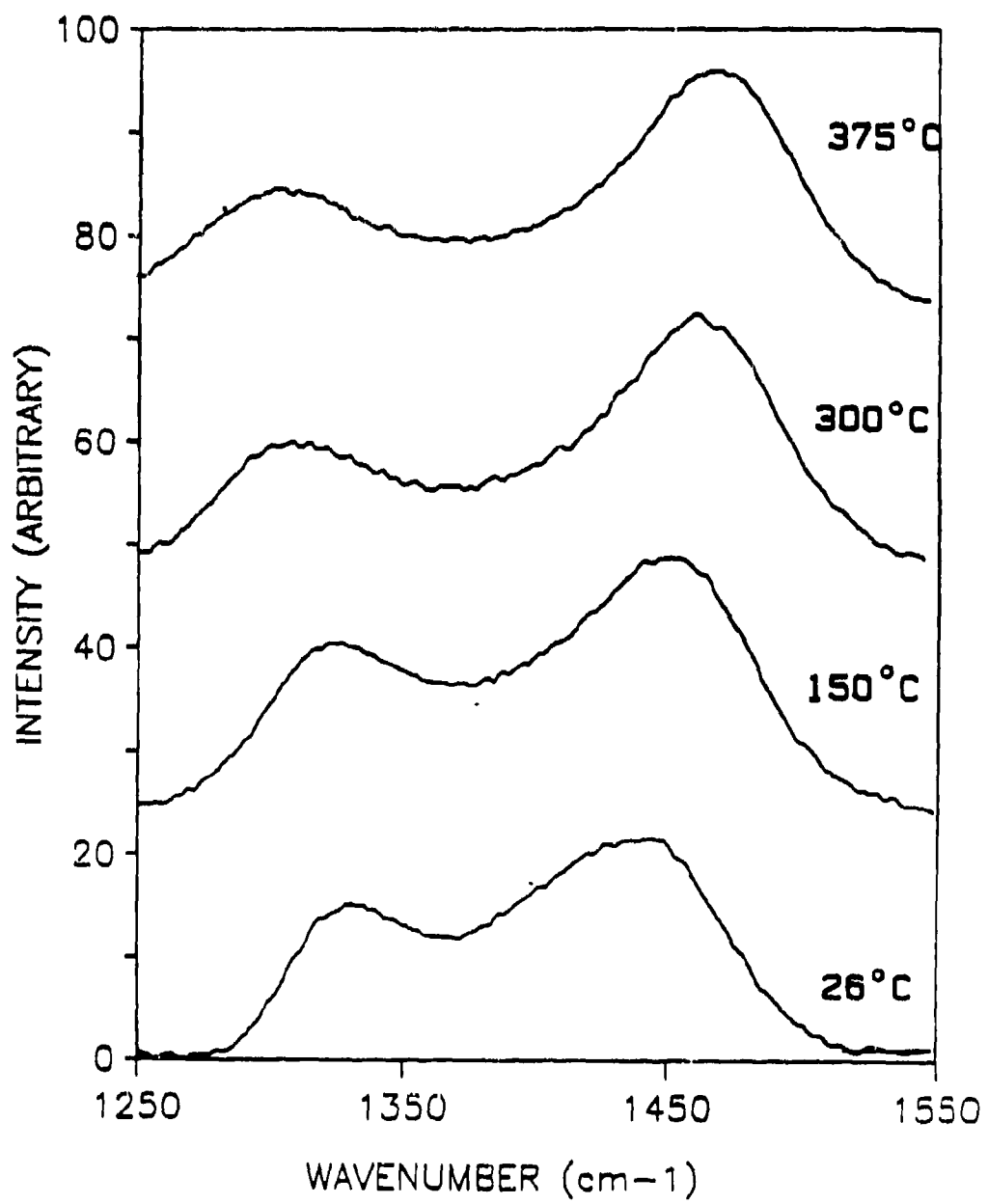


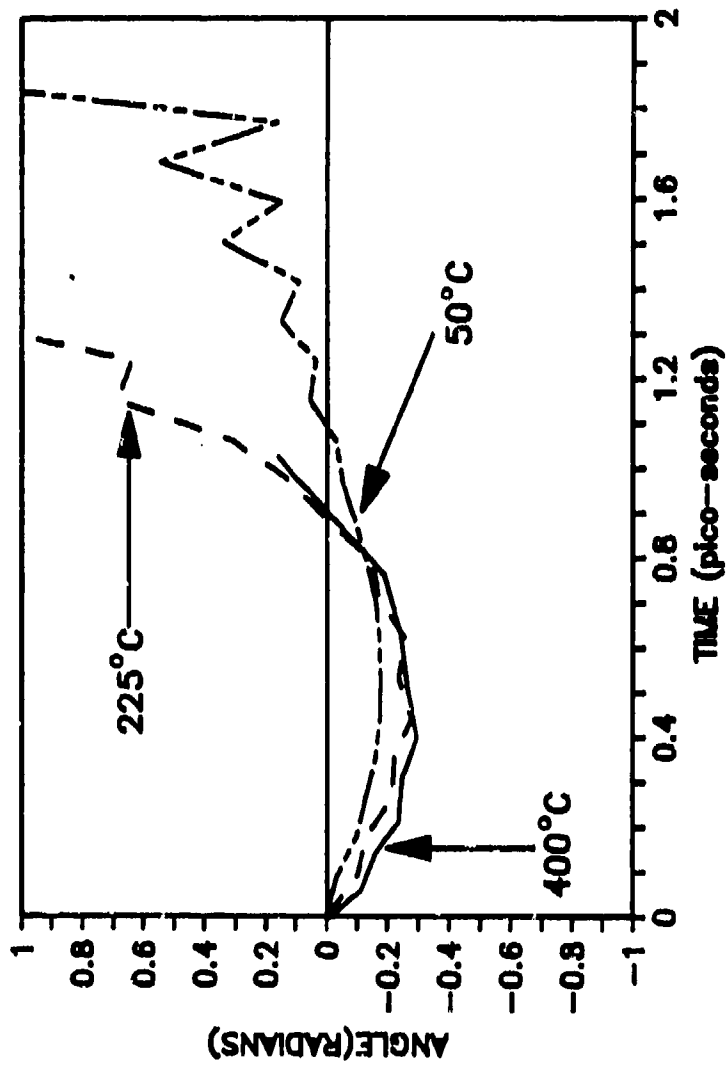


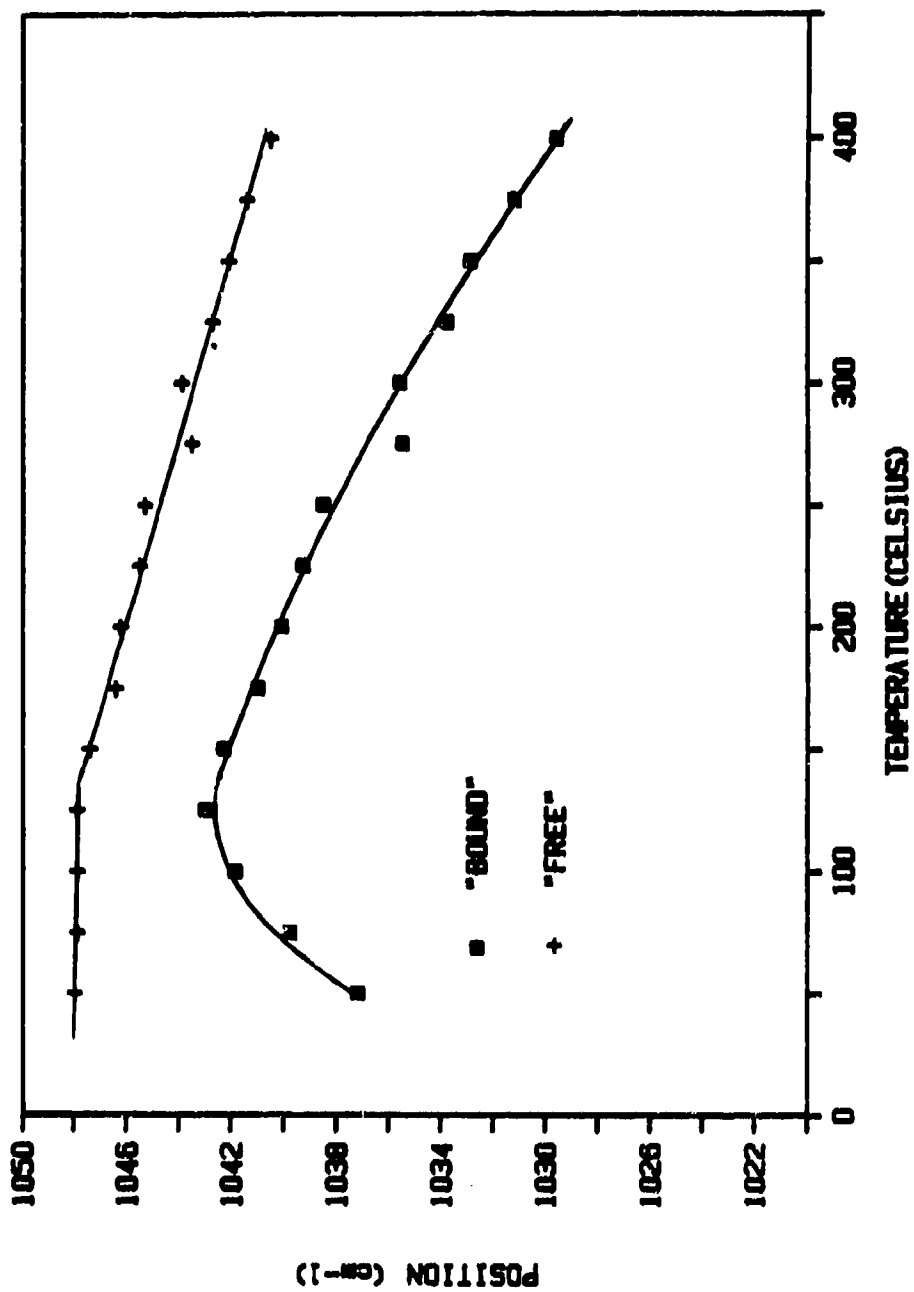


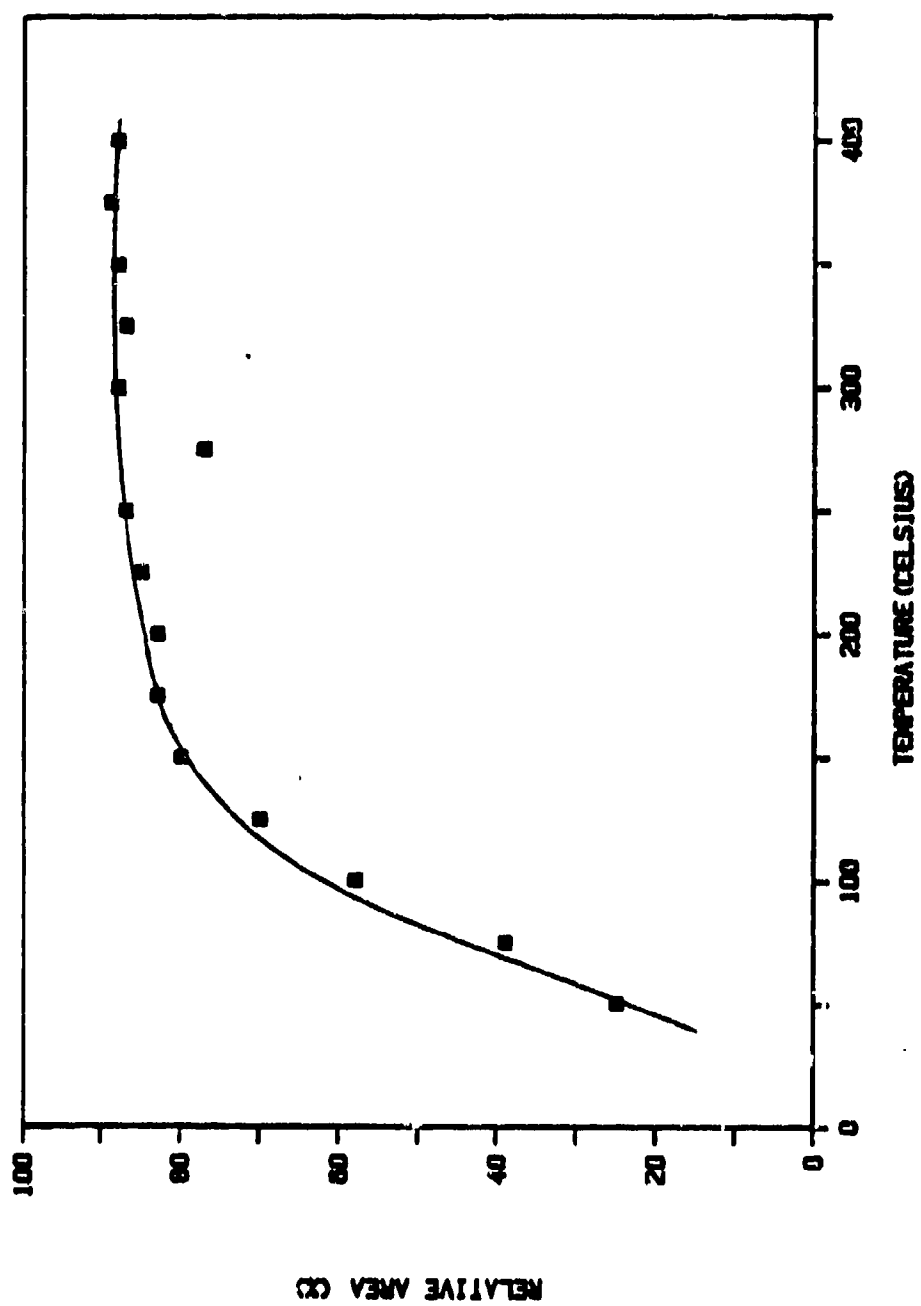


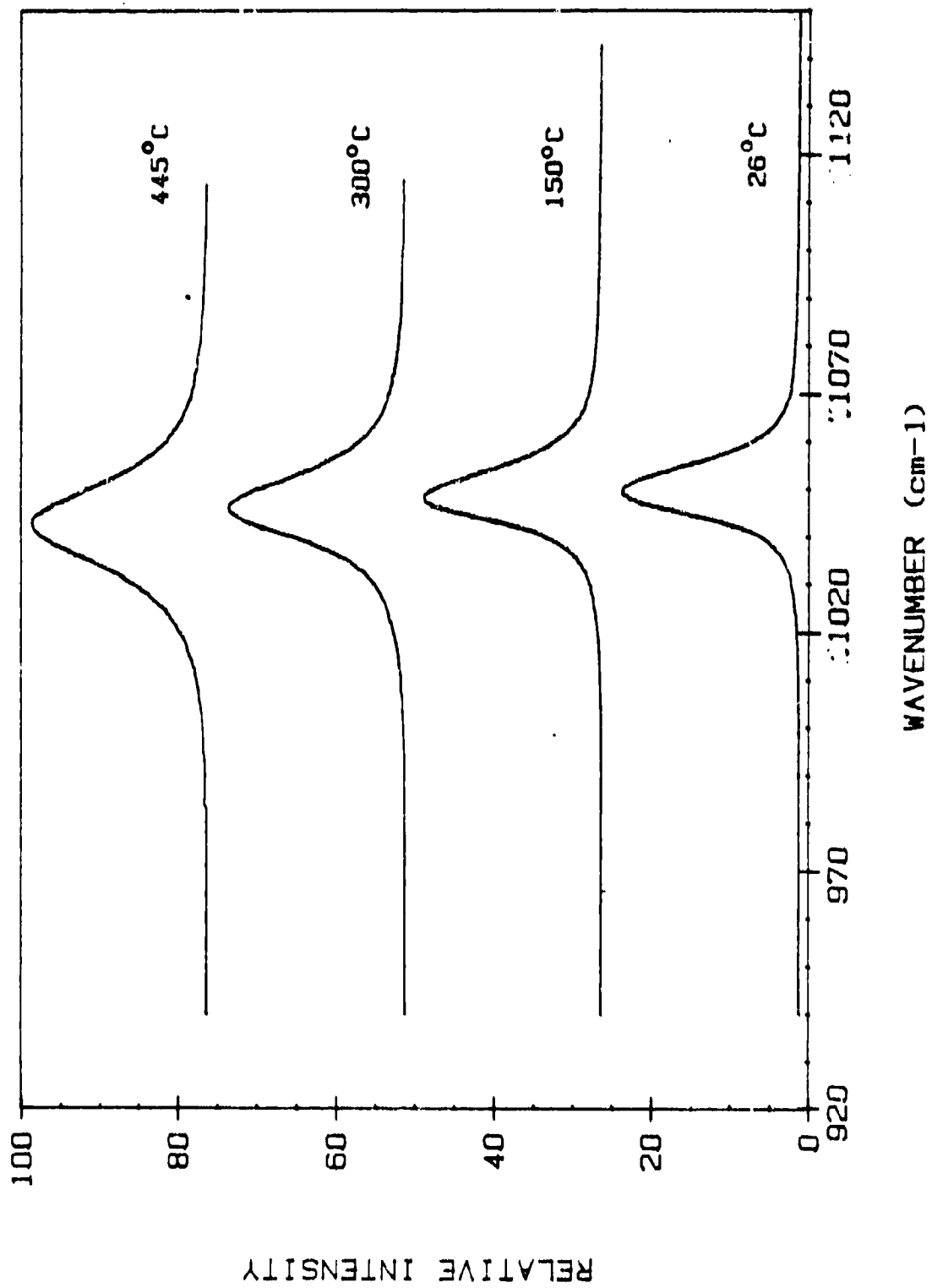


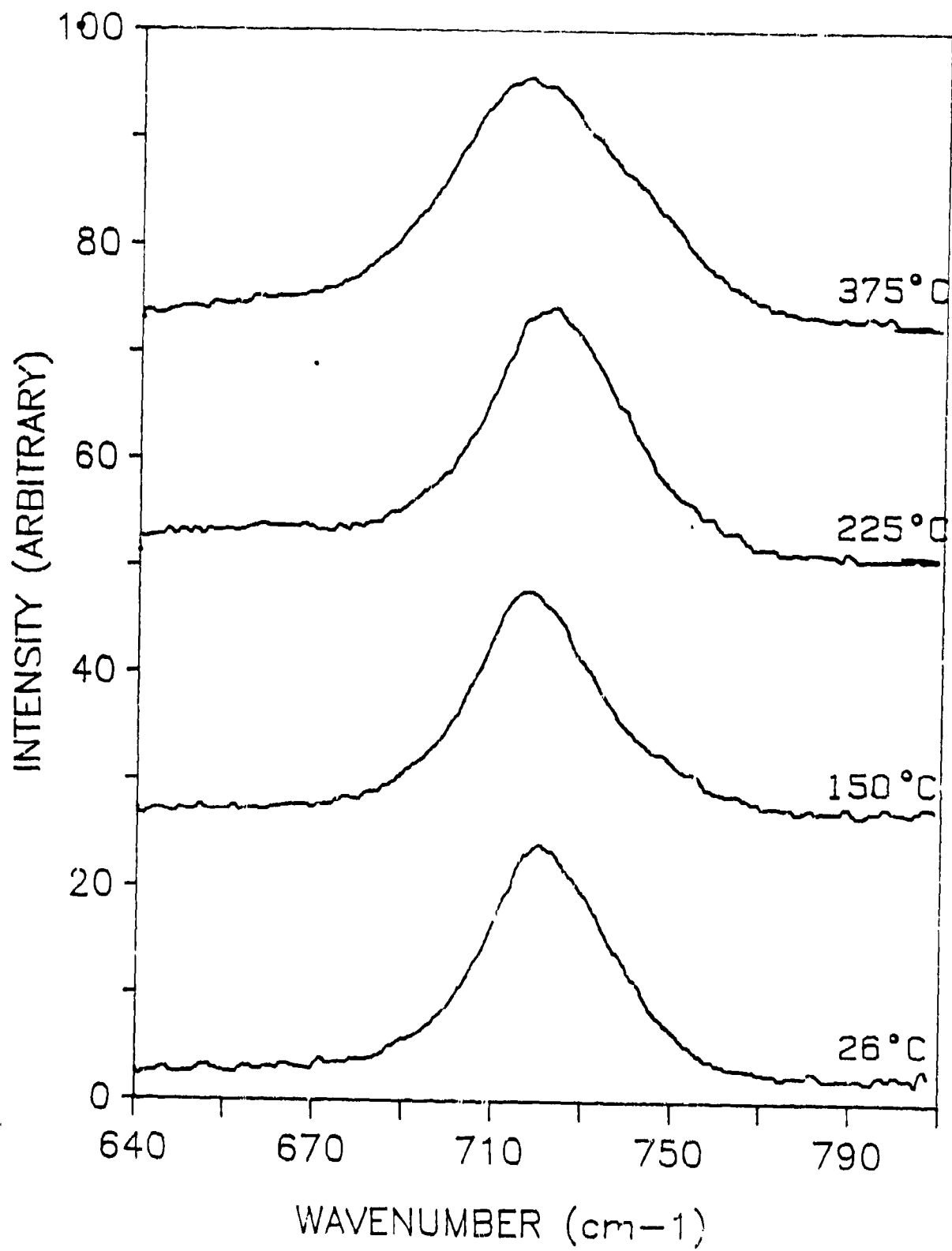


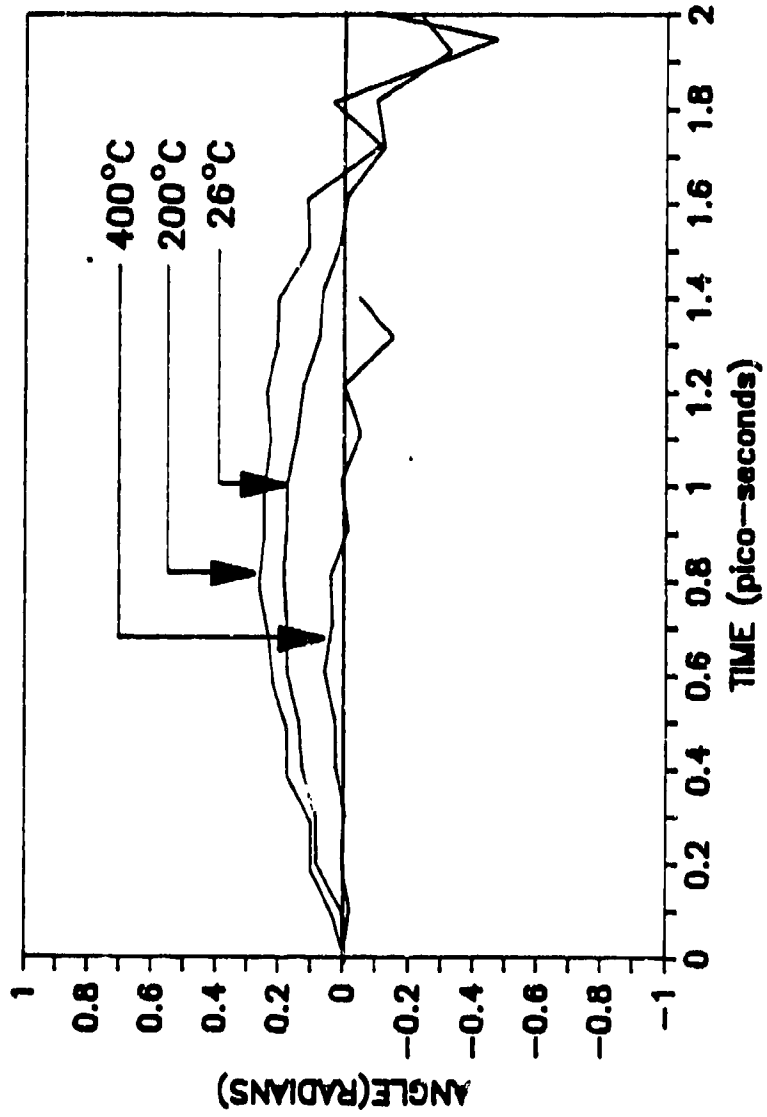




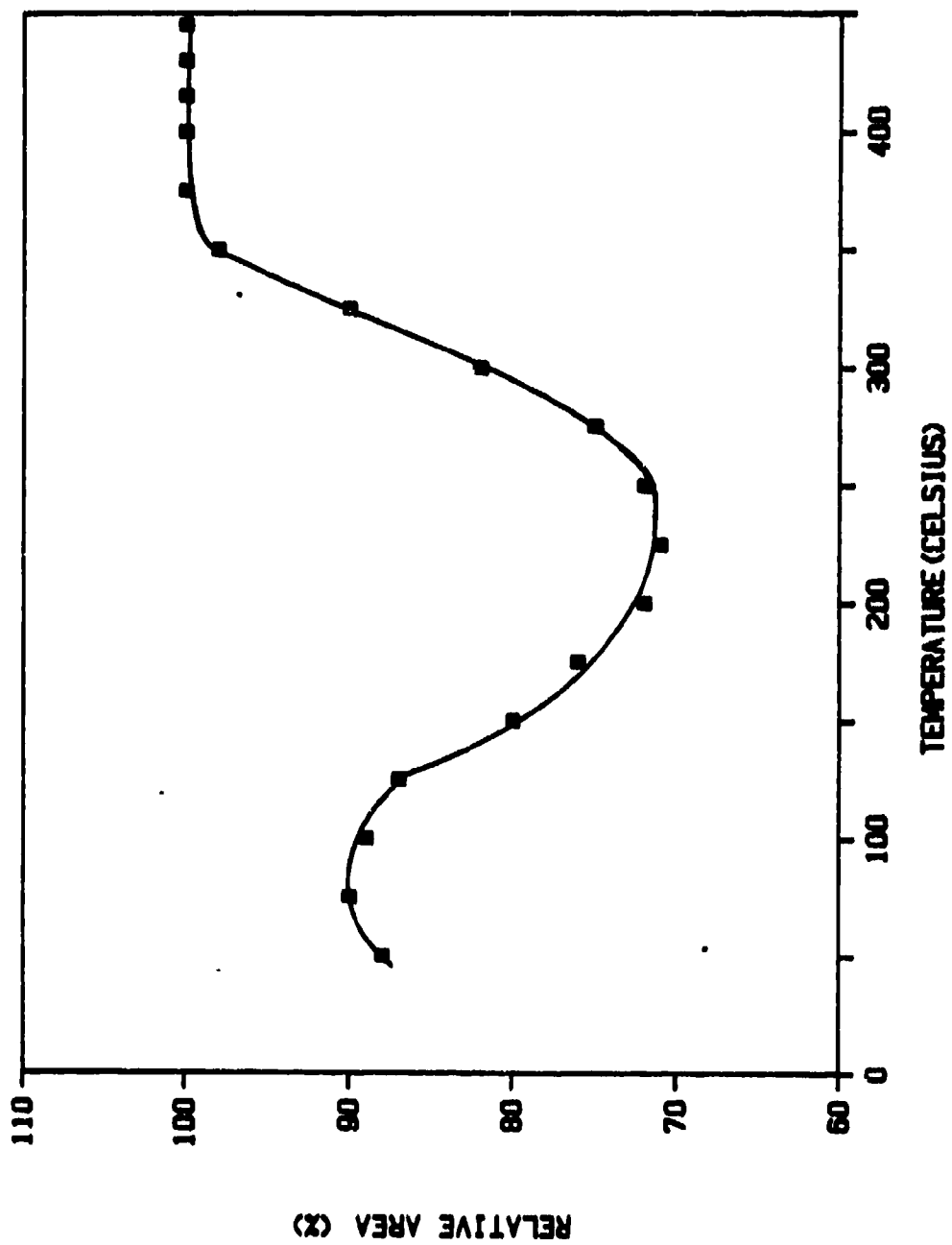


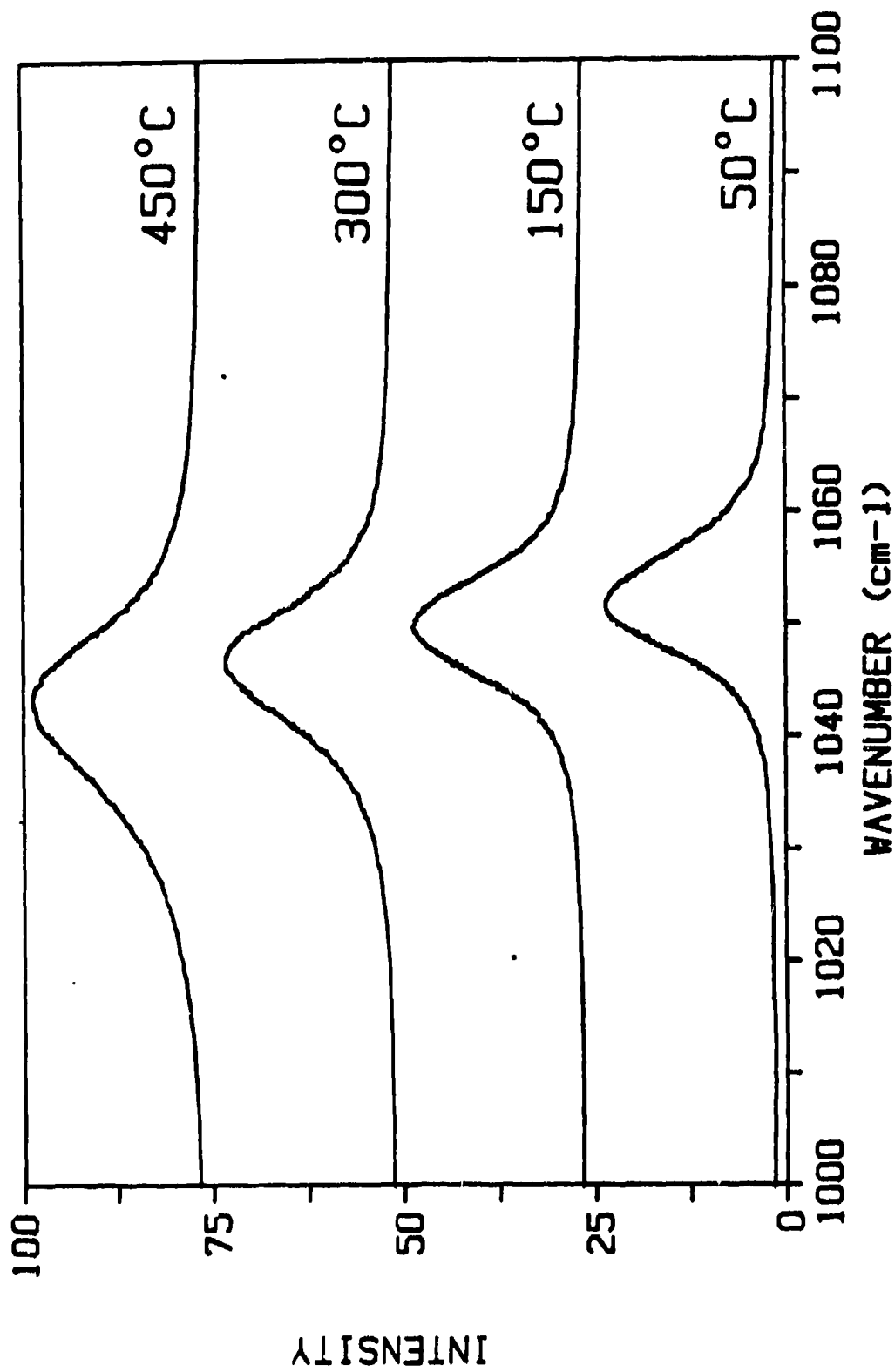


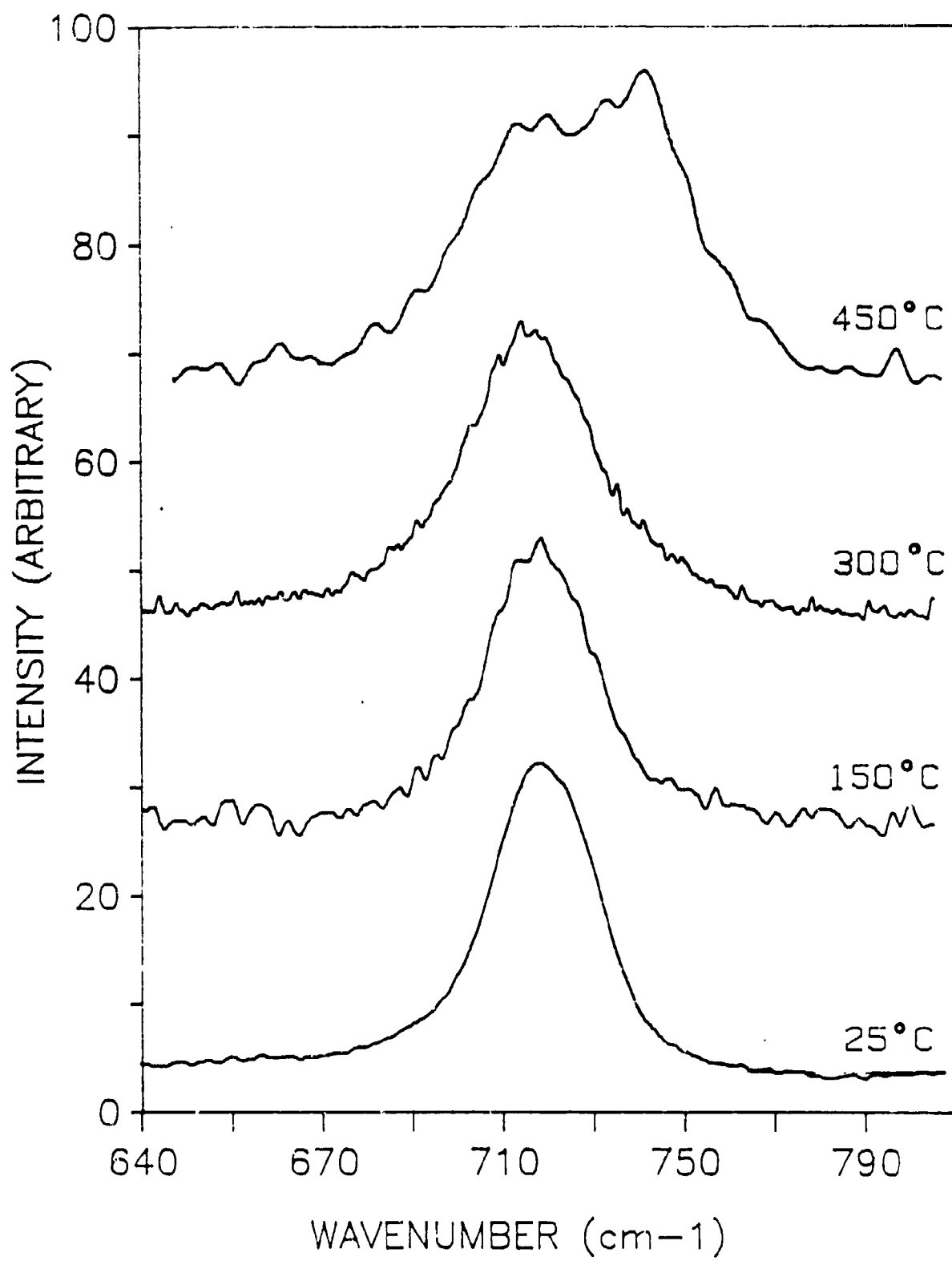


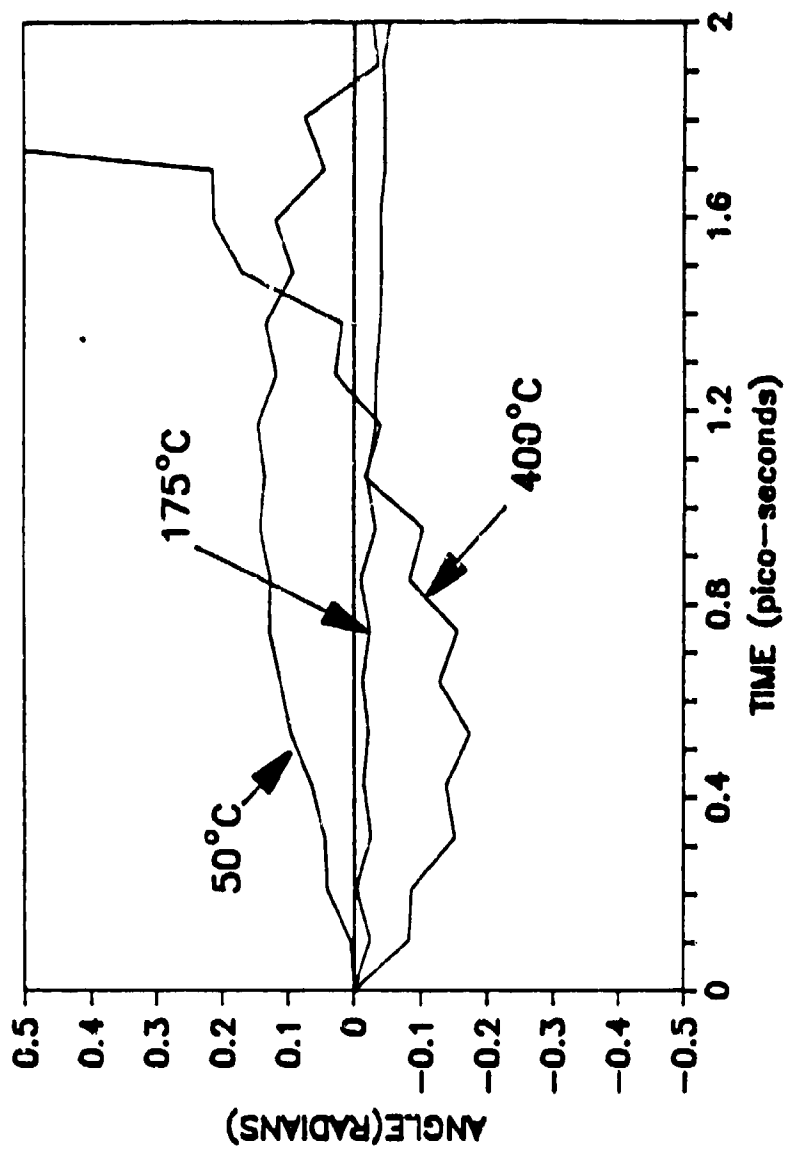


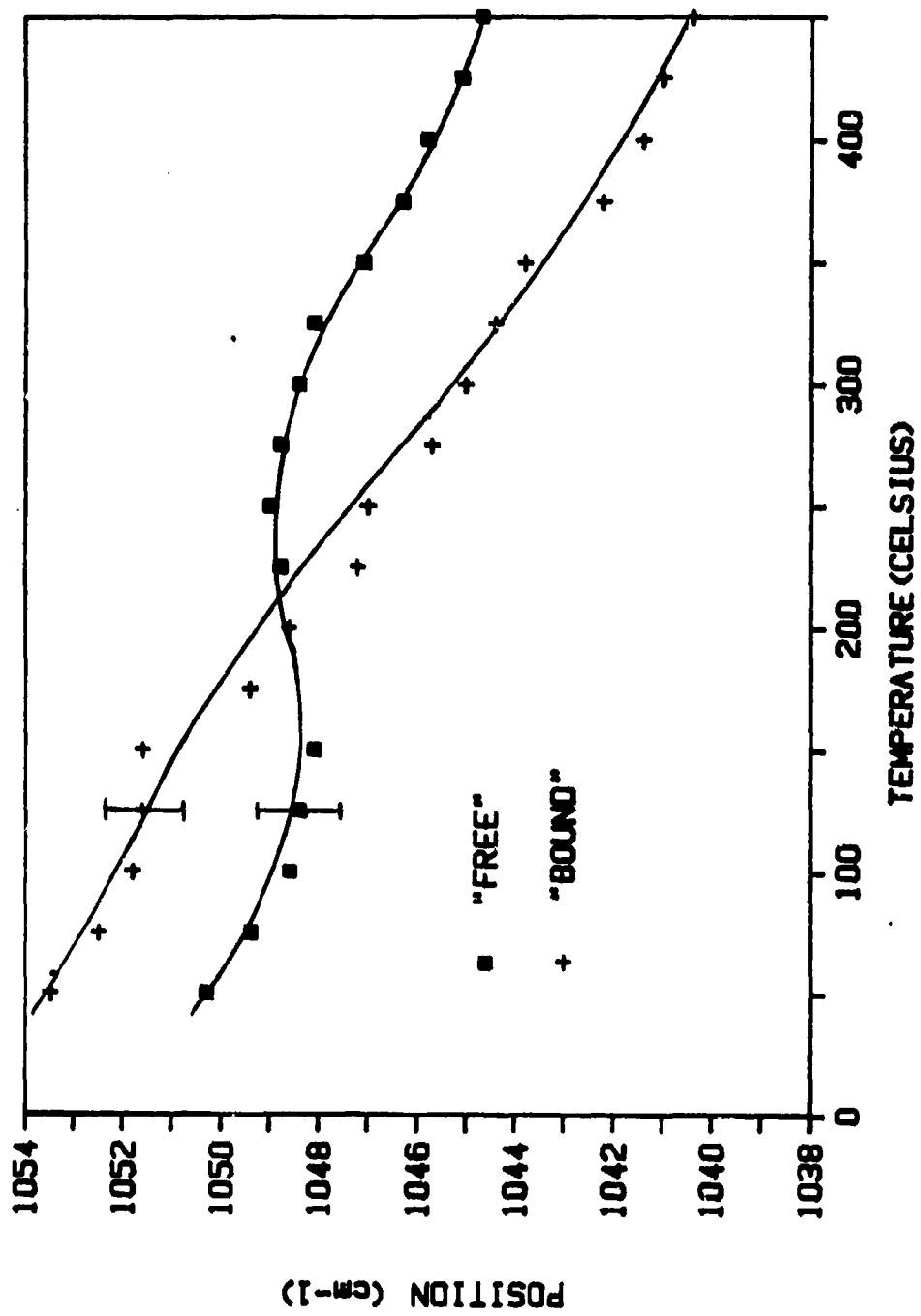
4:1

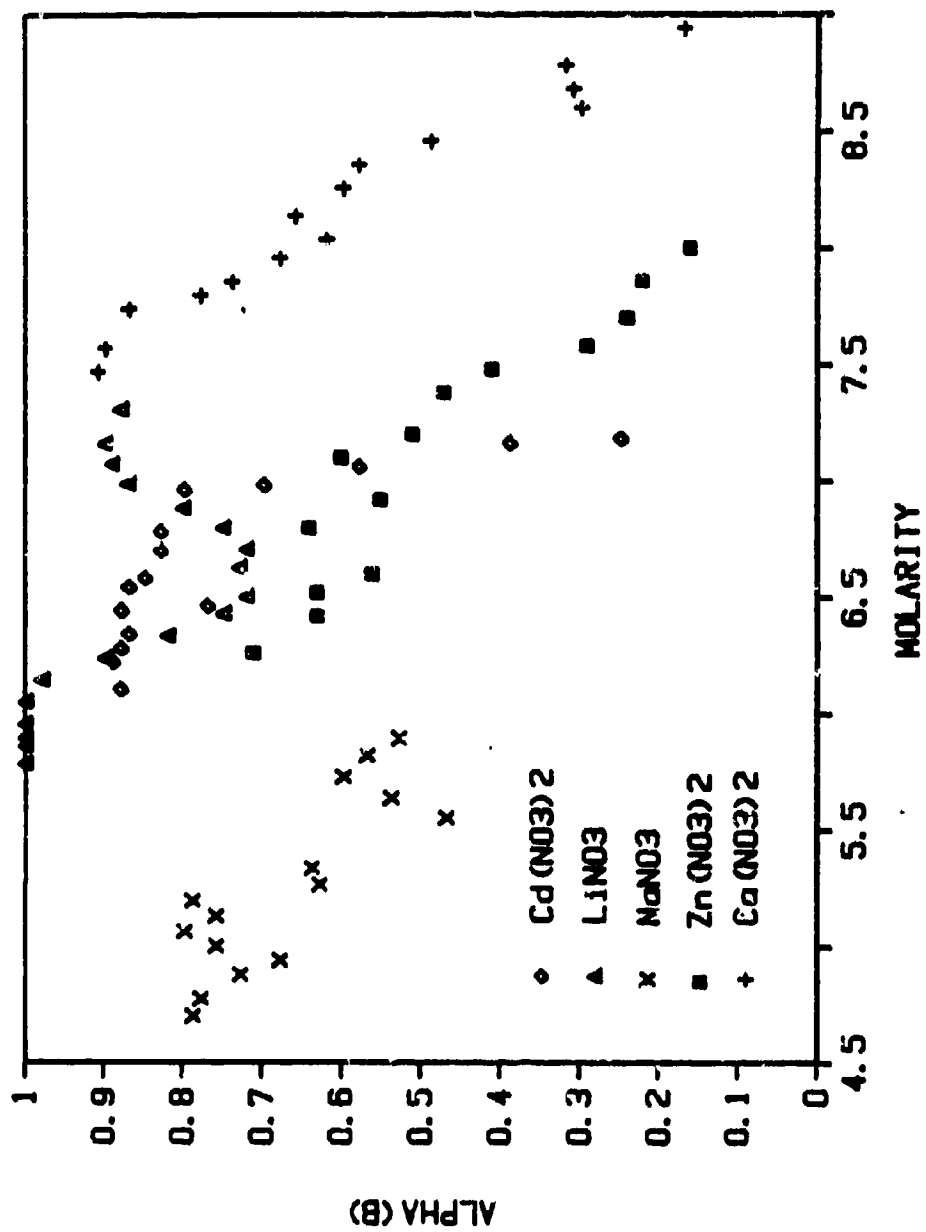












THERMAL DECOMPOSITION OF ENERGETIC MATERIALS 32.
ON THE INSTANTANEOUS MOLECULAR NATURE OF AQUEOUS
LIQUID GUN PROPELLANTS AT HIGH TEMPERATURE AND
PRESSURE BEFORE THERMAL DECOMPOSITION

T. B. Brill[†], P. D. Spohn and J. T. Cronin

Department of Chemistry

University of Delaware

Newark, DE 19716

ABSTRACT

By analogy with recent studies on the molecular behavior of concentrated aqueous nitrate salt solutions at high pressure and temperature, hydroxylammonium nitrate-based liquid propellants would be expected to contain relatively covalent, contact ion pairs the instant before chemical decomposition ensues at high temperature and pressure. This may accentuate the first step of the decomposition process which appears to be proton transfer.

INTRODUCTION

The early reaction schemes that might occur in aqueous nitrate salt solutions are of interest for gaining a complete phenomenological description of ignition/combustion in hydroxylammonium nitrate(HAN)-based liquid gun propellants (i.e. LGP1845, LGP1846, NOS305).¹ In practice, the propellant is pressurized and ignited as a dense spray of liquid droplets. Hence, many of these droplets experience a very rapid temperature and pressure rise before complete gasification ensues. For this reason, the behavior of concentrated aqueous solutions of nitrate salts above the critical point of pure water (374°C, 3200 psi) is of interest. The results might be projected to describe the behavior of thermally less stable solutions of HAN and alkylammonium nitrates. HAN solutions decompose above 140°C under slow heating conditions so that the ionic properties during an instantaneous surge to much higher temperature and pressure would be difficult to investigate experimentally. Unfortunately, few studies give a molecular description of aqueous nitrate salt solutions in the high pressure and temperature regime.²

Recently, the first broad-based study of the Raman spectra of concentrated aqueous nitrate salt solutions containing mono and divalent cations was completed.³ By drawing on these and other data, a simple molecular description based on experiment can be put forth for how the salt components of liquid gun propellants might be expected to behave when they are subjected to a high pressure and temperature transient before the onset of massive decomposition.

DO LGP DROPLETS EXPERIENCE A HIGH TEMPERATURE?

The endotherm synchronous with the loss of H₂O from LGP1845 is strongly dependent on the applied pressure.⁴ Figure 1 shows that significant loss of water (endotherm) occurs in the 180-220°C range when 500 psi Ar is applied.⁴ This temperature range is lower than, but similar to, the boiling temperature of pure water subjected to about the same applied pressure. A complicating feature in LGP1845 is the fact that HNO₃(g) is formed from the decomposition of HAN. HNO₃ forms by an endothermic reaction which occurs approximately simultaneously with the water evolution. Therefore, for the purpose of illustrating that LGP1845 requires a high temperature to drive off water when under high pressure, dT_b/dP for pure water up to the critical point (Figure 2)⁵ is a useful qualitative analogy. Note that the boiling point of water reaches a quite high value under pressures that are an order of magnitude smaller than those that occur in a liquid propellant gun chamber. The critical point for aqueous salt solutions would be expected to be above that of pure water. Therefore, by inference, liquid LGP droplets in the thermal wave could experience a high instantaneous temperature while subjected to a high instantaneous pressure.

A MODEL FOR LGP BEHAVIOR AT HIGH TEMPERATURE

Because concentrated HAN solutions in water decompose above 140°C, extremely fast diagnostics and temperature jump methods would be needed to ascertain the molecular behavior at high temperature and pressure. A more tractable experiment is to use a stable nitrate salt of a monovalent ion, such as NaNO₃, in place of HAN. NaNO₃ is thermally stable in aqueous solution to at least 450°C.

Concentrated NO_3^- salt solutions contain solvent separated ion pairs and contact ion pairs at room temperature.⁶ As the temperature is increased to 450°C under 30 MPa, lineshape analysis, Fourier transformation, and curve resolution of the symmetric NO_3^- stretch permits the change in the concentration of the contact ion pairs and the solvent separated ion pairs to be resolved. Figure 3 shows the concentration of the contact ion pairs in 6.82m NaNO_3 as a function of temperature. Note that as the temperature is increased the tendency is to form contact ion pairs. In fact, this behavior is general to all nitrate salts studied to date (Li^+ , Na^+ , Zn^{2+} , Ca^{2+} , Cd^{2+})^{2,3} and largely originates from the decrease in the dielectric constant of H_2O (and, hence its ion solvating power) with increasing temperature.⁷ Thus, ionic salts in solution become increasingly molecular and have increasingly more covalent interaction between the anion and cation as the temperature increases. This same phenomenon can be expected to occur with the ions comprising a liquid gun propellant. HAN and the alkylammonium nitrate fuel will become more covalent, molecular-like ion pairs at higher temperatures.

How the hydroxylammonium and nitrate ions instantaneously come together in solution is a matter of conjecture. No doubt there is a strong statistical component. However, there is no question as to how they prefer to associate because the crystal structure of HAN is known.⁸ As shown in Figure 4 the association is dominated by discrete hydrogen bonds. As the NO_3^- and NH_3OH^+ ions relax toward one another at high temperature with less of the competition of mediating hydrogen bonding with H_2O , it would be expected that proton transfer between the anion and cation, and between the cation and H_2O would be enhanced. It then follows that proton transfer between the anion and cation leading to HNO_3 should be (and is)⁴ the first detected chemical reaction in the

decomposition of HAN-based liquid gun propellants.

ACKNOWLEDGMENT

We are grateful to the Army Research Office for support of this work on DAAG20-84-K-0198.

REFERENCES

1. N. Klein, BRL-TR-2641, Ballistic Research Laboratory, Aberdeen Proving Ground, MD, 1985.
2. D. E. Irish and T. Jarv, Appl. Spectrosc., 37 (1983) 50.
3. P. D. Spohn and T. B. Brill, J. Phys. Chem., submitted.
4. J. T. Cronin and T. B. Brill, Combust. Flame, 74 (1988) 81.
5. "Handbook of Chemistry and Physics", 68th Edition, R. C. Weast (Ed.) CRC Press, Inc. (1987).
6. For example see D. E. Irish and M. H. Brooker in "Advances in Infrared and Raman Spectroscopy", R. J. H. Clark and R. E. Hester (Eds.) Chapter 6, p 212, W. J. MacKay, Ltd. 1976.
7. K. Heger, M. Uematsu, and E. U. Franck, Ber. Bunsenges. Phys. Chem., 84 (1980) 758.
8. A. L. Rheingold, J. T. Cronin, T. B. Brill, and F. K. Ross, Acta Cryst., C43 (1987) 402.

FIGURE CAPTIONS

FIGURE 1

The thermal profile of 1.5 μL of LGP1845 superposed on the quantified gas products when the sample is heated at $110^\circ\text{C}/\text{sec}$ under 500 psi Ar. Note the endotherm corresponding, in part, to evolution of H_2O in the $180\text{-}220^\circ\text{C}$ range.

FIGURE 2

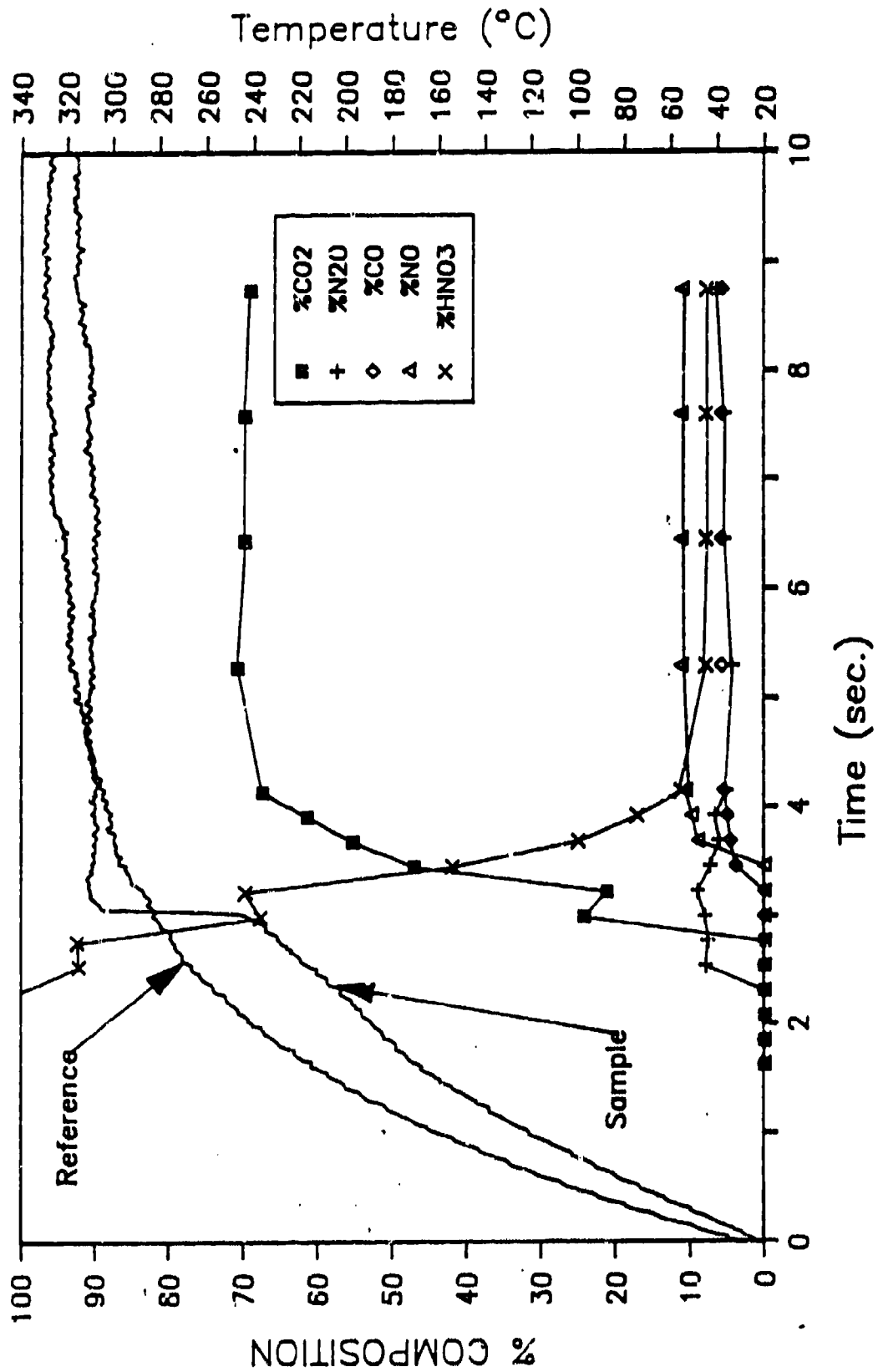
The boiling temperature of pure H_2O as a function of the applied pressure.

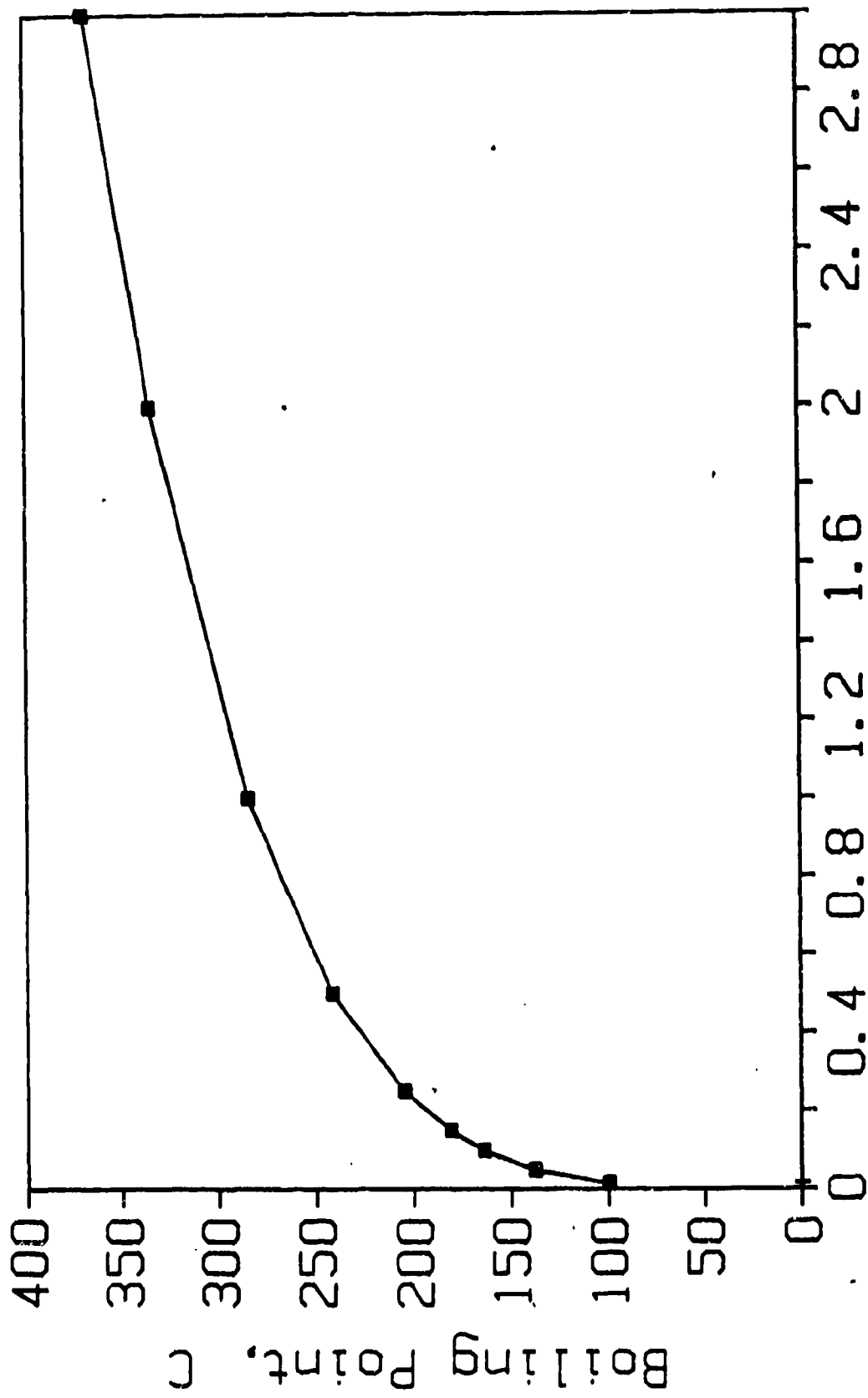
FIGURE 3

The relative concentration of the $\text{Na}^+\cdots\text{NO}_3^-$ contact ion pair as a function of temperature in 6.82m NaNO_3 .

FIGURE 4

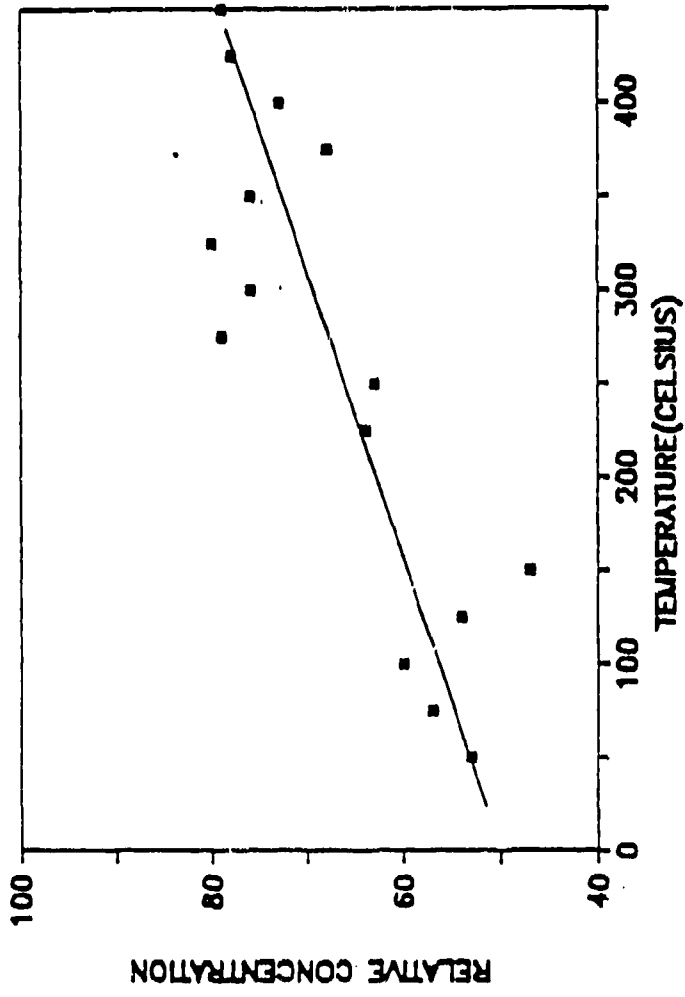
The packing of NO_3^- ions about one NH_3OH^+ ion in solid $[\text{NH}_3\text{OH}]\text{NO}_3$.

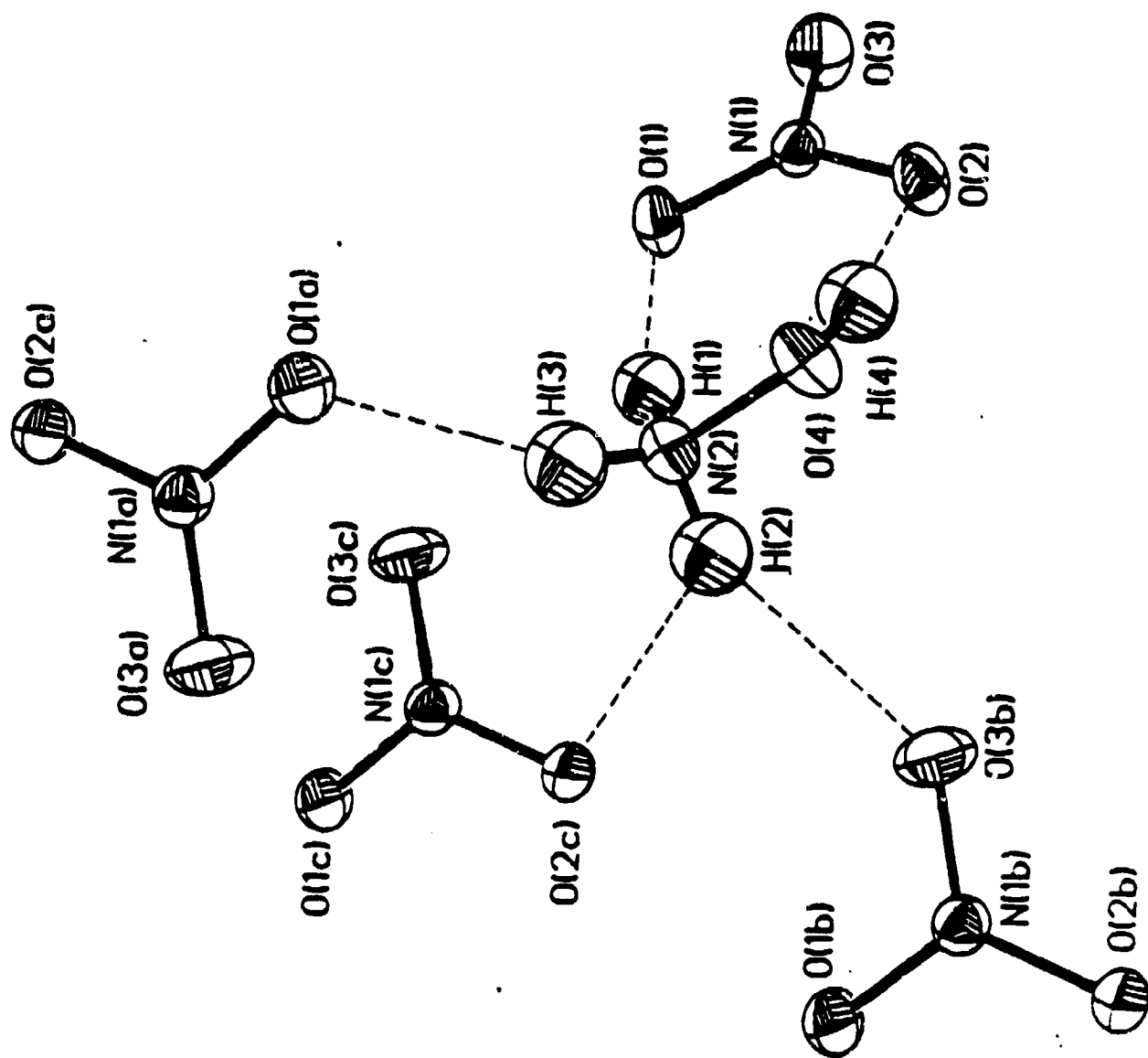




Applied Pressure, $\text{psi} \times 10^{-3}$

Fig 3





A Raman Spectroscopy Cell for Aqueous Solutions to 500°C and 34.5 MPa

P. D. SPOHN and T. B. BRILL*

Department of Chemistry, University of Delaware, Newark, Delaware 19716

The design of a Raman spectroscopy cell capable of maintaining aqueous solutions at temperatures up to 500°C and pressures up to 34.5 MPa (5000 psi) is described. The apparatus is illustrated with the chemical interactions that take place in aqueous $\text{Ca}(\text{NO}_3)_2$ and $\text{Zn}(\text{NO}_3)_2$ under these conditions.

Index Headings: High pressure; High temperature; Raman spectroscopy; Spectroscopic techniques.

INTRODUCTION

Spectroscopic research into the fundamental properties of materials under extreme conditions requires unique types of sample cells. A number of such cells, designed for containing liquid solutions at elevated temperature and pressure, have been described.¹ The nature and concentration of solutions that can be examined is limited by the presence of corrodible surfaces in the cell and the maximum temperature limit. We sought a cell that was small in size in the sample region, that was straightforward to align and use, and that permitted the sample to be changed without disassembly. We also sought pressures and temperatures higher than is customary. Described herein is a new corrosion-resistant cell meeting these objectives and useful for obtaining Raman spectra at temperatures up to 500°C while under hydrostatic pressure up to 34.5 MPa. Some spectroscopic results from this cell are illustrated with descriptions of the changes that occur in $\text{Ca}(\text{NO}_3)_2$ and $\text{Zn}(\text{NO}_3)_2$ solutions as a function of temperature and pressure. Raman spectroscopy has been shown to provide information on the geometry, equilibrium distributions, and interactions between constituents of such solutions.² The high temperatures reached place the liquids near or into the supercritical region. This domain is of interest for research in the geothermal industry,³ for studies of reactions in supercritical water,⁴ and for work with liquid propellants.⁵

EXPERIMENTAL

Instrumentation. All spectra were recorded with the use of a Spex Model 1401 double-monochromator spectrometer with a Spectra-Physics Model 164 4-W argon-ion laser source. The laser was tuned to 488.0 nm with a power output of 0.6 to 1.35 W. The monochromator slit widths were set at 150 μm . The spectrometer was calibrated by the use of the 218-, 314-, and 459- cm^{-1} bands of CCl_4 . The vibrational frequencies are accurate to within $\pm 1 \text{ cm}^{-1}$ in a relative sense and $\pm 2 \text{ cm}^{-1}$ in an absolute sense. The spectra were obtained with the use

of photon counting. Spectra were recorded with this system interfaced to a Nicolet 1180 data acquisition system. Decreases in ground-state vibrational population led to weaker spectra at the elevated temperatures. Multiple scanning and computer treatment greatly improved the data.

Sample Container and Pressure Seals. Figure 1 shows the essential features of the sample cell. The optical region consists of a polished single-crystal sapphire capillary disk (0.378 in. o.d. \times 0.2 in.) with a polished inner bore (0.0635 in. i.d.) obtained from Insaco Incorporated, Quakertown, PA. This sapphire was supported between two tantalum rods (0.130 in. o.d., 0.028 in. i.d. \times 5 in.) with 45° beveled ends (Ultramet Corp., Pacoima, CA). As detailed in Fig. 2, the sapphire disk was sealed against the tantalum rods by a washer of 0.5-mm-thick gold foil, which compensated for any irregularities in the contact surfaces. This seal withstood internal hydrostatic pressure in excess of 35 MPa, when less than 10 pounds/in.² of inward pressure was applied to the tantalum rods by the retaining screws.

The 316 stainless-steel support pieces (Figs. 1 and 2) support the tantalum rods through the set screws and transmit heat to the sapphire sample container from resistive heating cables (ARI Industries Incorporated) which wrap them. The relatively small size of the support pieces and sample compartment permitted uniform heating of the sample in the sapphire.

The high-temperature portion of the cell was isolated from the aluminum endplates and retaining screws by machinable Corning MACOR ceramic plates (1.5 in. \times 1.5 in. \times 0.5 in.). The aluminum endplates (5 in. \times 3 in. \times 0.5 in.), through which water was circulated, cooled the retaining screws, allowing the cell to be aligned and manipulated while at elevated temperature. The coil springs allowed for expansion and contraction of the support pieces, tantalum rods, and sapphire disk, so that the pressure seal was maintained. The cell was additionally insulated by glass wool. The focusing and collection optics of the spectrometer were cooled by a nitrogen stream when required.

Pressure and Temperature Generation and Measurement. As shown in Fig. 3, pressure in the cell was generated by a ConstaMetric 1 metering pump (LDC/Milton Roy). The pump was connected to the tantalum rods by $\frac{1}{8}$ -in. S.S. tubing and S.S. Swagelok connectors. Pressure was measured by a Perma-Cal pressure gauge (0–10,000 psi, 0.25% accuracy) connected in-line. Located between the pressure gauge and the pump output was a check valve. Directly preceding the cell was a high-pressure sample injector (Rheodyne Model 7125), secured for sample input. The exit side of the cell was connected to

Received 20 April 1987

* Author to whom correspondence should be sent.

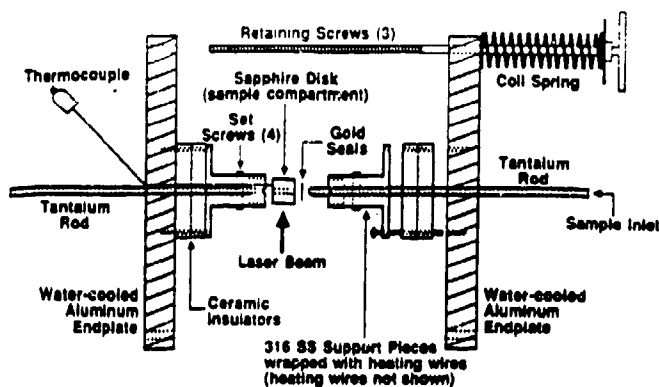


FIG. 1. The essential features of the high-pressure/high-temperature cell drawn to scale.

a metering valve, which was opened for sample input and closed for pressurizing of the system.

We heated the sample by wrapping the support pieces (Fig. 1) with resistive heating cables (0.040-in. o.d. \times 2.5 ft) consisting of an Inconel sheath containing two nickel/chromium/iron wires that were insulated from each other and from the sheath by compacted magnesia. The cables provide approximately 75- Ω resistance per cable.

Power was supplied and temperature monitored by an Electronic Control Systems Model 6414 time-proportioning digital temperature controller. The range of the controller was 0 to 1000°C when an iron/constantan (J-type) thermocouple was used. The thermocouple contacted the sapphire disk through one support piece (Fig. 1). A second monitoring thermocouple attached to the side of the sapphire recorded the same temperature.

Cell Assembly and Maintenance. Prior to our assembling the cell, all seal materials were cleaned thoroughly. The sapphire, gold foil, and beveled ends of the tantalum rods were first cleaned with distilled, deionized water. The final washes were with spectroscopic grade methanol, which left no residue. The sapphire and tantalum rod ends were frequently inspected for chips and scratches that would make sealing the cell more difficult.

We aligned and fastened together the stainless-steel support pieces, ceramic insulators, and aluminum endplates to give two equivalent endpieces (hereafter referred to as sapphire support groups). A tantalum rod was centered inside each sapphire support group and secured by the set screws. The thermocouple could be inserted prior to or after assembling of the cell.

We cut gold foil into square sections (approx. 0.25 in.²) and then shaped them by pressing a scribe (Starret Model No. 70B) through the section into a block of wood. The foil was then cleaned and one section set on top of the sapphire. One of the sapphire support groups was lowered onto the sapphire until the beveled end of the tantalum rod pressed into and centered the sapphire. The half-assembled cell, with the sapphire bore facing upwards, was then placed vertically in a wood-block holder. A second section of gold foil was laid on top of the sapphire and the other sapphire support group lowered onto it. Once in place, the retaining screws were tightened until the seals were formed.

The assembled cell was mounted horizontally in a slightly modified Spex kinematic sample mount. The la-

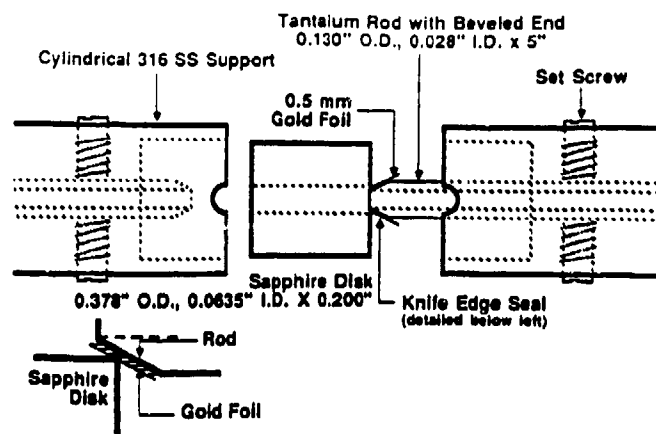


FIG. 2. An expanded view (to scale) of the optical "window" region of the cell, illustrating how the seal contact is made. For purposes of viewing, the right-hand Ta rod is shown protruding. When the cell is assembled, this Ta rod is recessed, as shown by the left-hand Ta rod. The lower insert expands this contact seal region still more.

ser beam entered from the bottom, and scattered light was collected at 90°. The cell was pressurized as desired, after alignment. Temperature was then increased as desired, and final alignment was made. Because of the small sample size (100 μ L), pressure changes with temperature were negligible (approx. 100 psi for a 475°C change).

We sealed the heating cable ends with ceramic cement to keep the magnesia dry. However, dielectric breakdown and/or cracking of the ceramic occurred after about 20 heating cycles. The cables were resealed after one inch of cable had been removed from each end. The heating cables could then be used for another 20 cycles. Because of scoring, the tantalum rods had to be rebeveled in a lathe with a small file after each cell disassembly. Sapphire etching or cracking occasionally occurred at elevated temperature and will be discussed momentarily.

RESULTS AND DISCUSSION

There are many advantages to be achieved with this cell design. The simplicity with which the seals are formed and pressure is generated makes it possible to assemble the cell in a short period of time. Once assembled and aligned, the cell can be cycled repeatedly from low to high temperature without having to be disassembled or realigned. Samples are changed and the cell flushed by the flow system, without disassembly. One can monitor the cleanliness and alignment of the cell by examining

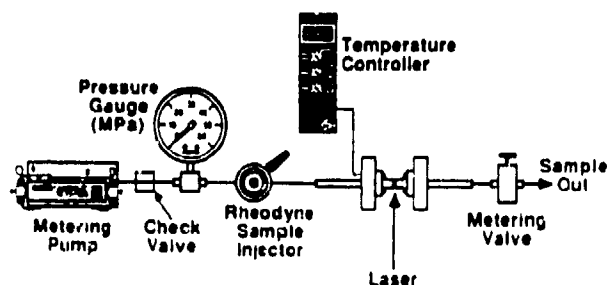


FIG. 3. A schematic of the sample injection and pressuring system used with this cell.

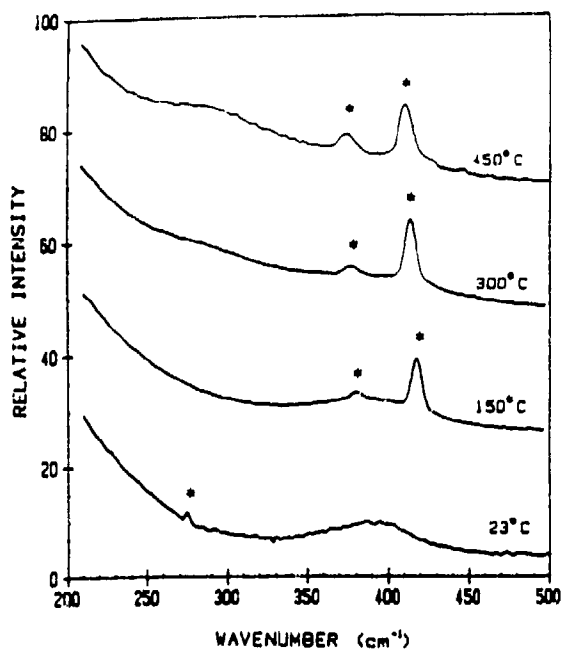


FIG. 4. The $Zn(H_2O)_6^{2+}$ region ($\sim 385\text{ cm}^{-1}$) and $Zn^{2+}-ONO_2^-$ stretch ($\sim 292\text{ cm}^{-1}$) as a function of temperature. The starred absorptions result from sapphire.

a sample known to contain an intense vibrational absorption.

The main problem encountered has been cracking, scratching, the etching of the sapphire surfaces. Sapphire is considered to be very corrosion resistant,¹ but our sapphire disks occasionally etched when pure water was heated above 300°. The salt solutions studied so far have not etched the sapphire at any temperature—although

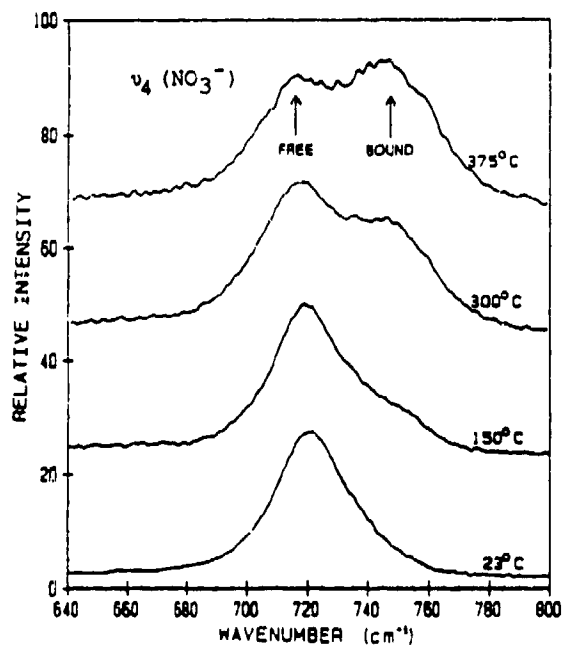


FIG. 5. The temperature dependence of the $\nu_4(NO_3^-)$ in plane bending mode, showing the increased amount $Zn^{2+}-ONO_2^-$ of contact-ion pairing at higher temperature.

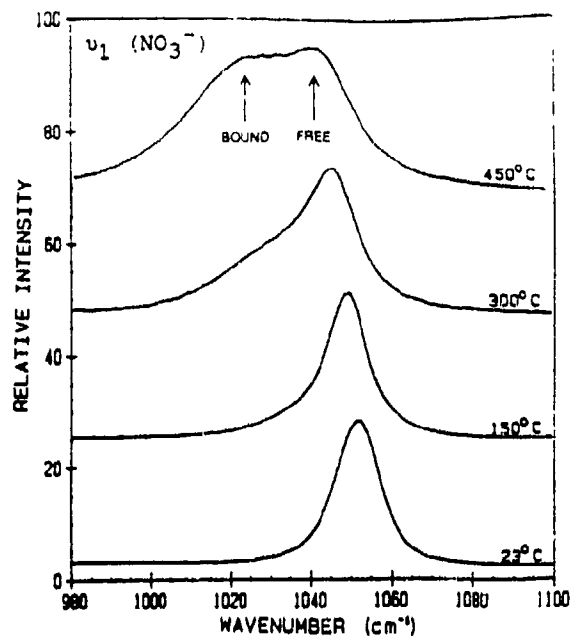


FIG. 6. The temperature dependence of the $\nu_1(NO_3^-)$ symmetric stretch, showing the increased contact-ion pairing of aqueous $Zn(NO_3)_2$ as the temperature is raised.

$Al(NO_3)_3$ and $Ga(NO_3)_3$ were not studied, because the spectral quality degraded at the elevated temperatures. Precipitation of the salt or etching of the sapphire may have occurred. The coil springs and the use of reasonably thick gold foil reduced the cracking and chipping of the sapphire due to thermal expansion. The cell was usually disassembled whenever temperatures above 375°C were examined, a procedure which also seemed to decrease the frequency of sapphire cracking.

The cell has been held at 450°C and 32 MPa for 8 h, without difficulty. Decreases in signal strength, due to lowered ground-state populations, and increased noise, due to sapphire fluorescence at elevated temperatures, were compensated for by an increase in the number of scans taken and computer treatment of acquired spectra. The studies reported herein were limited to 450°C, al-

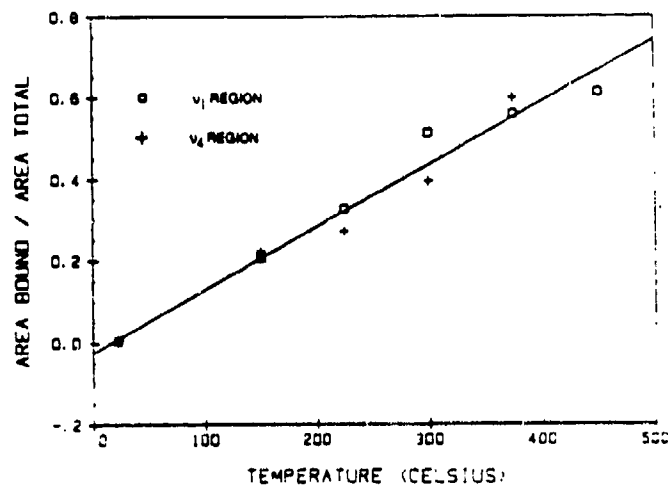


FIG. 7. The amount of contact-ion pairing of NO_3^- in aqueous $Zn(NO_3)_2$ increasing linearly with temperature.

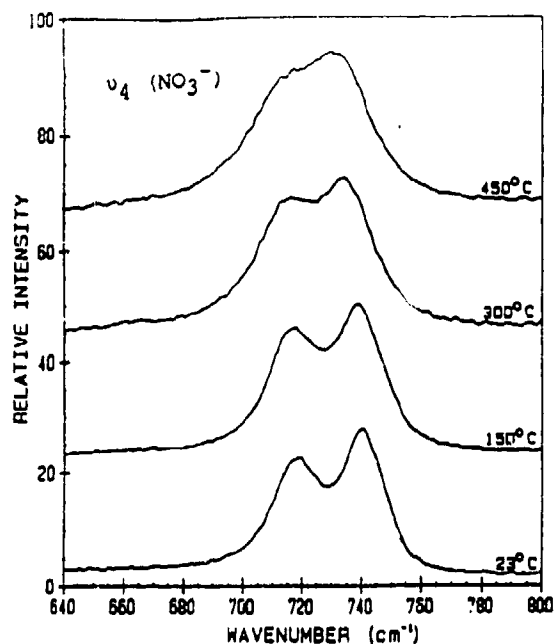


FIG. 8. The $\nu_4(\text{NO}_3^-)$ region of aqueous $\text{Ca}(\text{NO}_3)_2$, showing that contact-ion pairing that occurs at room temperature changes little with temperature.

though excellent spectra have been recorded at 500°C and 34.5 MPa—which approaches the practical working limit of the design.

Illustrating the use of this cell, Figs. 4–6 show Raman spectra of a 4.50 mol/kg solution of $\text{Zn}(\text{NO}_3)_2$ over a temperature range of 25 to 450°C at 28.9 MPa. $\text{Zn}(\text{NO}_3)_2$ has been previously studied up to a temperature of 300°C under 11 MPa of hydrostatic pressure.⁶ Of interest are the intensity changes of five new bands as the temperature is raised. A polarized absorption at 385 cm^{-1} , which has been attributed to the A_{1g} breathing mode of $\text{Zn}(\text{H}_2\text{O})_6^{2+}$,⁷ is known to decrease in intensity and increase in frequency as the temperature is increased. As the intensity of this mode decreases, there are concomitant increases in the intensity of three other absorptions. The M- ONO_2 stretch is observed in solution at approximately 270 cm^{-1} .^{8,9} As shown in Fig. 4, an increase in intensity occurs at 292 cm^{-1} , which can be attributed to the $\text{Zn}^{2+}\text{-ONO}_2^-$ stretch.^{6,10} At the same time there are increases in the intensity of absorptions at 740 cm^{-1} and 1038 cm^{-1} . The 740- cm^{-1} band appears as a shoulder on the ν_4 in-plane deformation mode of the free nitrate ion at 719 cm^{-1} (Fig. 5). According to Fig. 6, the 1038- cm^{-1} band appears on the low-frequency side of the NO_3^- symmetric stretch (ν_1) and was resolved with the use of a simplex nonlinear regression-curve resolving routine.¹¹ The ν_3 asymmetric NO_3^- stretch region of the spectra also exhibits some changes. Two absorptions were present under ambient conditions, at 1328 and 1418 cm^{-1} . Gradually replacing these absorptions as the temperature was elevated were two absorptions at 1305 and 1492 cm^{-1} .

Spectral changes in the ν_3 region occurred up to 300°C, but not between 300°C and 450°C. However, temperatures above 300°C caused an increase in the amount of bound nitrate, as evidenced by the increased intensity

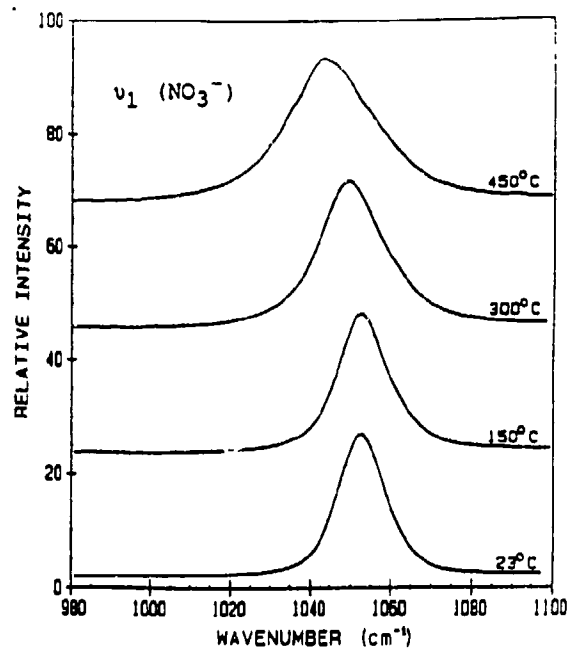


FIG. 9. The ν_1 symmetric stretch of NO_3^- as a function of temperature, showing increasing absorption asymmetry as the temperature is increased.

in the ν_1 and ν_4 regions. Curve resolving of the ν_1 and ν_4 regions provided information on the relative concentrations of the species.⁶ The area of the bound (contact ion pair) NO_3^- absorption divided by the total area of ν_1 or ν_4 was plotted vs. temperature (Fig. 7). Area changes for the two regions are approximately linear over the temperature range examined.

Figures 8 and 9 show the spectra of 5.5 mol/kg $\text{Ca}(\text{NO}_3)_2$ over a similar temperature range. Differences between the $\text{Ca}(\text{NO}_3)_2$ and $\text{Zn}(\text{NO}_3)_2$ spectra are numerous. At room temperature the $\text{Ca}(\text{NO}_3)_2$ solution shows complete splitting of the in-plane ν_4 bending mode (Fig. 8), which is representative of direct cation-anion contact.⁶ There is little change in ν_4 as the temperature is increased. No

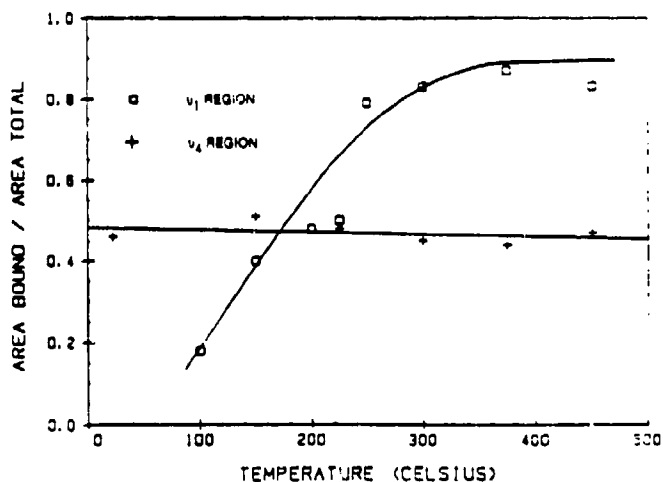


FIG. 10. The ratio of bound vs. free NO_3^- in aqueous $\text{Ca}(\text{NO}_3)_2$ as judged by the ν_1 and ν_4 absorptions of NO_3^- . The data suggest that ν_4 is not reliable for ascertaining differences in the contact-ion pairing.

$\text{Ca}^{2+}\text{-NO}_3^-$ stretch in the 300-cm^{-1} region is observable at any temperature, even though there is evidence from $\nu_1(\text{NO}_3^-)$ of direct ion contact. As the temperature is increased, the ν_1 symmetric stretch of NO_3^- becomes unsymmetrical, suggesting that the free NO_3^- and contact ion-pair NO_3^- bands are resolvable in this region (Fig. 9). After curve resolving of the ν_1 and ν_2 regions, the spectral changes can be described by the area changes vs. temperature (Fig. 10). The area for the bound species in the ν_1 region does not change significantly with temperature, but changes linearly with temperature up to 300°C in the ν_2 region. The changes in the ν_2 spectra were therefore attributed to thermal line broadening instead of to changes in the equilibrium distribution of the NO_3^- species. The splitting of the NO_3^- asymmetric stretch (ν_3) increases by 50 cm^{-1} for $\text{Ca}(\text{NO}_3)_2$ from 23°C to 450°C , while for $\text{Zn}(\text{NO}_3)_2$ the increase is 115 cm^{-1} over the same temperature range. Thus, the spectral changes for aqueous $\text{Zn}(\text{NO}_3)_2$ are much more marked than those for aqueous $\text{Ca}(\text{NO}_3)_2$.

We are continuing to examine other aqueous inorganic nitrate salts to characterize the behavior of the ions above 300°C .

ACKNOWLEDGMENTS

We are grateful to Drs. R. H. Wood and W. B. Daniels for helpful consultations concerning the cell design. Mr. George Rutynowski machined various parts of the cell. The Army Research Office generously supported this work under DAAG29-84-K-0198.

1. M. Buback, D. A. Crerar, and L. M. Vogel, in *Hydrothermal Experimental Techniques*, H. L. Barnes and G. C. Ulmer, Eds. (John Wiley and Sons, New York), in press.
2. D. E. Irish and M. H. Brooker, in *Advances in Infrared and Raman Spectroscopy*, J. H. R. Clark and R. E. Hester, Eds. (Heyden, London, 1976), vol. 2, pp. 212-311.
3. T. W. Swaddle, *Chem. Can.* **32**, 21 (1980).
4. B. Subramaniam and M. A. McHugh, *I&EC Proc. Des. Dev.* **25**, 1 (1986).
5. N. Klein, BRL-TR-2641 (Ballistics Research Laboratory, Aberdeen Proving Ground, Maryland, 1985).
6. D. E. Irish and T. Jarv, *Appl. Spectrosc.* **37**, 50 (1983).
7. J. T. Bulmer, D. E. Irish, and L. Odberg, *Can. J. Chem.* **53**, 3806 (1975).
8. D. E. Irish, A. R. Davis, and R. A. Plane, *J. Chem. Phys.* **50**, 2260 (1969).
9. A. R. Davis and D. E. Irish, *Inorg. Chem.* **7**, 1699 (1968).
10. Y. K. Sze and D. E. Irish, *J. Solution Chem.* **8**, 395 (1978).
11. J. Noggle, Program F-CURVE (LEDS Publishing Co.), 1986.

Thermal Decomposition of Energetic Materials 26. Simultaneous Temperature Measurements of the Condensed Phase and Rapid-Scan FT-IR Spectroscopy of the Gas Phase at High Heating Rates

J. T. CRONIN and T. B. BRILL*

Department of Chemistry, University of Delaware, Newark, Delaware 19716

Rapid-scan infrared spectroscopy (RSFT-IR) with better than 100-ms temporal resolution has been used to quantify the gas decomposition products of energetic materials in real time at various heating rates up to 800°C/s and under buffer gas pressures of 1 to 1000 psi. A new method is described that permits simultaneous real-time recording of the temperature of the condensed phase and of the IR spectra of the gaseous products under the above conditions. Endothermic and exothermic events in the condensed phase can now be correlated with the evolved gases under conditions approaching those of combustion. The design and procedure for using the cell are given and are applied to the thermalolysis of 1,7-diazido-2,4,6-trinitro-2,4,6-triazaheptane (DATH) and pentaerythrityltetrammonium nitrate (PTTN).

Index Headings: Infrared; Instrumentation, thermal analysis; Thermal decomposition; Spectroscopic techniques.

INTRODUCTION

The thermal decomposition of materials in the condensed phase leading to gas products is complicated by the fact that the event is a complex, heterogeneous, physicochemical process. Gas, liquid, and solid zones may be simultaneously present, with reactions occurring in each phase. Also, heat is absorbed and released in the condensed phase as a result of many parallel reactions. De-

spite this complexity, fast thermal decomposition demands attention because it is one of the major processes that exist during combustion and thermal explosions.

We have investigated the fast thermal decomposition of many exothermically decomposing materials using a home-built pyrolysis cell¹ which permits real-time *in situ* analysis by FT-IR spectroscopy of the gas products evolved when 1 to 2 mg of sample are electrically heated at rates of 25 to 400°C/s under static Ar pressures of 1 to 1000 psi. Given the complexity of thermal decomposition reactions, it might be surprising that any patterns at all can be found. Qualitative relationships have been uncovered between the parent molecular structure and the gases detected in the initial 0.2 s of decomposition. These include a measure of understanding of the formation of NO₂,^{2,3} HONO,⁴ NO,⁴ CH₂O,⁵ N₂O,⁵ and NH₃,⁶ the influence of pressure on the first detected gas products;⁷ the effect of trigger linkages;⁸ the effect of cyclization on the decomposition products;⁹ oscillating processes;¹⁰ and the transition from decomposition to deflagration.¹¹

The thrust of this research is extended in this paper to the description of a method for real-time thermal profiling of the condensed phase at the same time the real-time IR analysis of the evolved gases is being made. Most importantly, these analyses are made at initial heating rates of up to 400°C/s. Although operating at a

Received 20 April 1987.

* Author to whom correspondence should be sent.

Thermal Analysis Cell

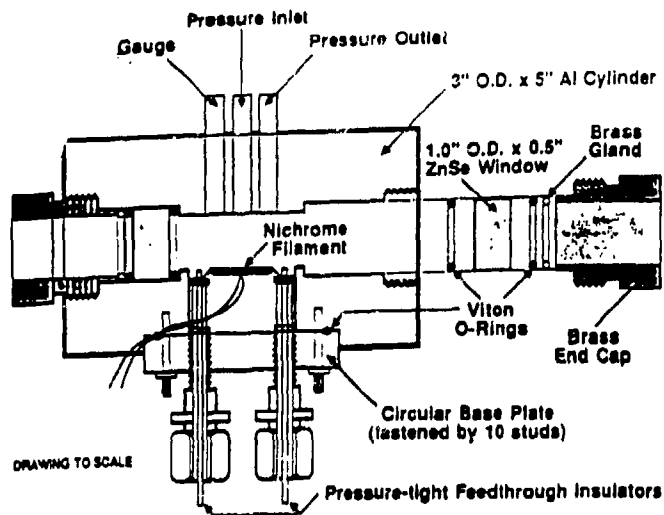


FIG. 1. A drawing to scale of the thermal profiling/RSFT-IR cell. The IR beam passes along the long axis of the cell.

much faster heating rate in this work, the thermal profiling aspect of this experiment resembles the slower method of differential thermal analysis. Fast techniques for measuring the temperature¹²⁻¹⁶ and weight changes^{17,18} have been employed by others in their efforts to study various types of thermal decomposition processes. However, to our knowledge, fast thermal profiling of the time-dependent temperature changes of the condensed phase has not been previously coupled to concurrent infrared spectroscopy. This combination has been achieved in this work and permits the endothermic and exothermic events taking place in the condensed phase to be associated with the gas products that are liberated.

EXPERIMENTAL

The variable-pressure fast-heating-rate thermolysis cell based on that of Karpowicz¹⁹ and the simplified design of Oyumi and Brill¹ is sketched in Fig. 1. The 0.5 × 1.0-in.-diameter ZnSe windows (II-VI Corp., Saxonburg, PA) have an unsupported area of about 0.5 in.², giving them a maximum gas pressure tolerance of about 5000 psi (34.5 MPa). For safety reasons, the pressure used did not exceed 1000 psi. This cell was also used at reduced pressures to 0.048 psi. The internal volume of the cell is 1.2 in.³

It was necessary to calibrate the temperature of the nichrome or platinum filament at each buffer gas pressure, because the rate of heat dissipation from the filament changed with the static pressure. We accomplished calibration by spot welding a 0.005-in. type-E thermocouple to the center underside of the filament and measuring its output on a Nicolet 4094 digital oscilloscope. Filament temperature vs. time curves were constructed at each pressure. The close correspondence of the melting point of several standard compounds confirmed the accuracy of the calibration. The absolute accuracy of the heating rate and final filament temperature was about ±4%.

Heating rates that could be adjusted, as desired, within the range of 10 to 800°C/s were achieved. In practice,

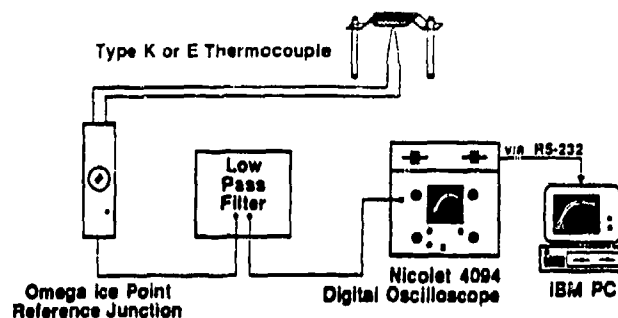


FIG. 2. A diagram of the thermal analysis portion of the cell showing the filament (Fig. 1) to which the thermocouple is spot-welded. With the appropriate interface and software, the digital oscilloscope can be bypassed.

however, 400°C/s has been the upper limit we have used. The highest heating rates were achieved with 0.025-in.-thick platinum filaments. Ramp heating of the filament was carried out until the final filament temperature (T_f) was reached. T_f depended on the heating rate, but, once reached, it remained constant for the duration of the experiment (normally 10 s). As the pressure was increased, we also had to increase the current to the filament to maintain a constant heating rate.

The IR beam was focused several millimeters above the surface of the filament. The height of the filament with respect to the IR beam was varied and was found not to influence the first-detected pyrolysis product concentrations. Moreover, at atmospheric pressure the convection of the gases upon firing of the filament was visually observed to be vigorous and swirling. The gases in the cell mixed at least as fast as the analysis was performed. These gases expanded into the cool buffer gas atmosphere.

Figure 2 shows a block diagram of the components that make up the thermal analysis component of the cell. The leads of the thermocouple spot welded to the center underside of the filament were brought out at the O-ring between the base plate and the body of the cell. The wires were connected through an Omega ice point reference junction to a home-built low-pass filter. This filter removed the 60-Hz signal created by the pyrolyzer, which otherwise overwhelmed the signal of the thermocouple. The thermocouple signal in millivolts vs. time was recorded and stored on the disk of a Nicolet 4094 digital oscilloscope. The thermal traces were transferred to an IBM PC for processing. Using a macro written for Lotus 1-2-3, we calculated the temperature (°C) vs. time trace for each run, graphs of both the reference and sample traces, and graphs of the difference trace (sample trace minus reference trace).

The effect of various metals used for the filament and thermocouple on the pyrolysis products was examined. Pt, Ni, W, and Ta foils and gold-coated nichrome were substituted for nichrome IV and were found not to have any significant effect on the pyrolysis product distribution. To determine if different spot-welded thermocouples affected the data, we attached type K, J, and E thermocouples to nichrome and platinum filaments.

Again, no significant differences were found in the thermal traces or product distributions.

In a typical experiment, two thermal traces were recorded—one of a filament without a sample, and the other of a filament on which one or two mg of sample were spread. Otherwise, the conditions were the same. The pyrolysis cell was sealed and purged with argon, and the pressure of Ar was adjusted to the desired level, as measured by a McDaniel gauge. The filament was connected to the Foxboro pyrolysis timer-current controller. A fast-acting shutter (Oriel) that blocked the IR beam of a Nicolet 60SX FT-IR spectrometer was connected in series with the filament through the pyrolysis control. The spectrometer was set to scan at 4-cm^{-1} resolution and 10 interferograms/s. Two interferograms were added in each file. With the spectrometer scanning, we initiated the experiment by triggering the oscilloscope to begin recording the output of the thermocouple and activating the filament/shutter circuit that simultaneously opened the shutter and began the heating. The first interferogram thereby corresponded to the onset of heating. A connection could easily be made between the time, temperature, and interferogram. The temperature and spectra were collected for 10 s.

The relative concentrations of the products in each spectrum were quantified by the ratioing of the intensity of a characteristic mode to the absolute intensity of that mode. The relative percent by volume concentration of each product was thereby obtained. Provided the sample size was similar, the relative concentrations of the gases were very reproducible in multiple determinations, showing that gas mixing occurs rapidly and uniformly in the cell. However, several details of this procedure of quantification merit mention. First, N_2 , H_2 , and O_2 can be products of thermal decomposition, but cannot be quantified with IR spectroscopy. H_2O was not quantified, because of the complexity of its rotation-vibration fine structure. Second, when pressures above 500 psi are used, the vibrational modes of gas products may be noticeably broadened.²⁰ This fact can produce some uncertainty in the concentration-intensity relationship. The absorption profiles for several of the gases were checked at various pressures and, except for HCN, convinced us that the error produced by the pressure broadening is negligible in the face of experimental uncertainty in the absolute intensities ($\pm 5\%$) listed in the literature. The effect of pressure broadening on the HCN absorptions was corrected for at 1000 psi Ar. The presentation of the relative rather than absolute concentrations compensates for most of the uncertainty in the quantitation procedure. Third, by chemical reaction rate standards, even rapid-scan infrared spectroscopy is a slow technique. The different intensities of the *P* and *R* branches show that the gases are thermally cool. The gas products observed are not necessarily formed from primary reactions. Instead, they have probably undergone many collisions before detection. Nevertheless, the temporal resolution used to quantify the gas products in these experiments and the heating rates are much greater than has been customary in pyrolysis research. This factor, coupled with the large amount of data obtained at one time, provides a new perspective on the thermolysis mechanisms of energetic materials.

TABLE I. A comparison of melting temperatures measured at fast heating rates compared with literature values measured at slow heating rates.

Compound	Melting point, °C	
	Fast heating ^a	Literature
Ammonium nitrate (AN), NH_4NO_3	170	170 ^b
Ethylenediaminedinitramine (EDNA), $\text{HN}(\text{NO}_2)(\text{CH}_2)_2\text{N}(\text{NO}_2)\text{H}$	170	177 ^b
1,7-Diazido-2,4,6-trinitro-2,4,6-triazasheptane (DATH)	133	133 ^c
3-Nitro-1,2,4-triazol-5-one (NTO), $\text{C}_2\text{H}_2\text{N}_4\text{O}_3$	275	265-68 ^d
1,3,5-Trinitro-s-triazine (RDX), $(\text{CH}_2\text{NNO}_2)_3$	200	203 ^b
Octahydro-1,3,5,7-tetranitro-1,3,5,7-tetrazocine (HMX), $(\text{CH}_2\text{NNO}_2)_4$	275	280 ^b
Ethylenediamine dinitrate (EDDN), $[\text{C}_2\text{H}_4(\text{NH}_2)_2](\text{NO}_3)_2$	180	185-7 ^b
Nitroguanidine (NGu), $\text{C}(\text{NH}_2)_2\text{NNO}_2$	250	250 ^b
Pentaerythrityl tetranitrate (PETN), $\text{C}(\text{CH}_2\text{ONO}_2)_4$	140	141 ^b
Methylenediaminedinitramine (MEDINA), $\text{CH}_2(\text{NHNO}_2)_2$	110	102 ^b
Hydrazinium nitrate, $(\text{NH}_2\text{NH}_2)\text{NO}_3$	65-70	70 ^b

^a $dT/dt = 70\text{--}150^\circ\text{C/s}$, 1-2 mg sample.

^b B. T. Fedoroff, *Encyclopedia of Explosives and Related Items* (Picatinny Arsenal, Dover, New Jersey, 1960).

^c Ref. 21.

^d K. Y. Lee and M. D. Coburn, *J. Energetic Mat.* 1, 1983.

RESULTS AND DISCUSSION

Thermal Profiling at High-Heating Rates. The thermal profiling portion of this cell strongly augments the already effective ability of rapid-scan infrared spectroscopy to elucidate rapid pyrolysis processes. The sensitivity of this cell to thermal changes is sufficiently high that only 1 to 2 mg of sample is needed. The small sample size reduces artifacts in the thermal trace that might be produced by nonuniform heating of the sample. On the basis of melting points measured at $70\text{--}150^\circ\text{C/s}$, compared with literature values measured at a slow heating rate (Table 1), the absolute temperature accuracy of the cell appears to be quite good. Furthermore, the thermal traces seem to be sensitive to thermal changes in the condensed phase and not to those involving gas-phase species.

The thermal profiles of the condensed phase can be displayed as (1) the sample temperature vs. time; (2) the sample minus the reference trace (ΔT) vs. time; or (3) ΔT vs. temperature. In practice, we have found that (1) and (2) are sufficiently informative and most easily obtained.

The relative concentrations of the gas products measured by FT-IR spectroscopy can be correlated with the thermal events detailed in the condensed phase. The cell also permits studies to be conducted at different pressures. These opportunities afford considerable conceptual understanding about the fast thermolysis of individual materials and mixtures of materials which, heretofore, have been difficult to study, owing to the complexity of the process.

The rapid-scan FT-IR/thermal profiling method is at present insufficient for kinetic measurements, because the heat and mass transfer cannot be assumed to be uniform. Therefore, our objective was not to make kinetic measurements but to describe some of the phenomena

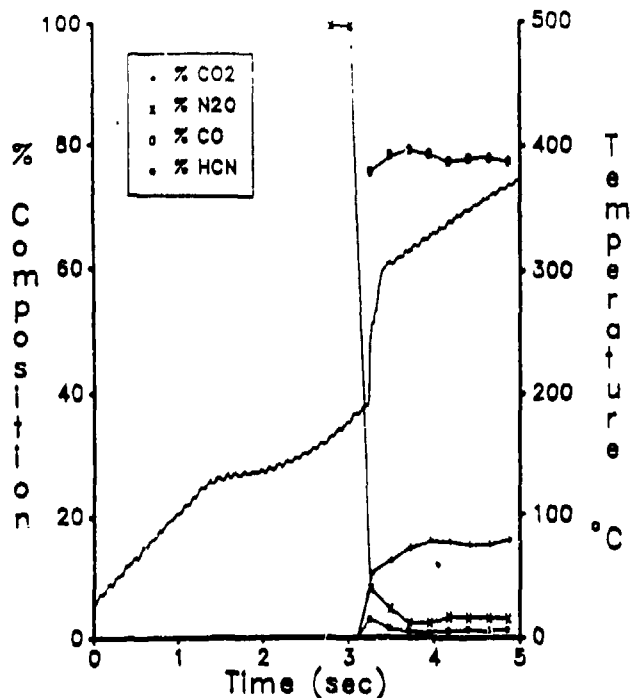
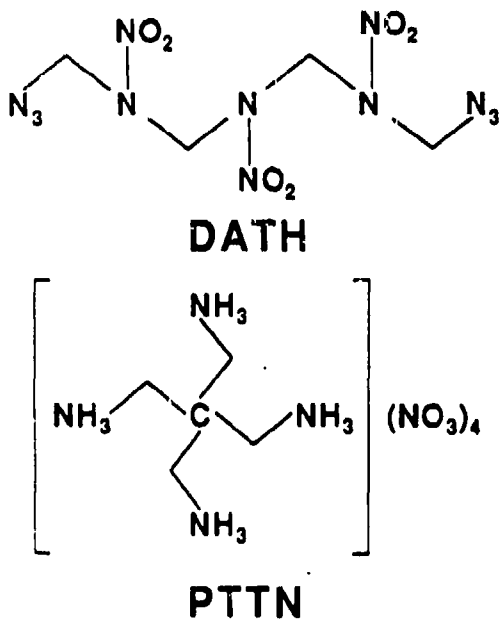


FIG. 3. The thermal trace of the condensed phase superimposed on the gas products evolved upon thermolysis of DATH at 80°C/s under 15 psi Ar.

that take place when a material rapidly heats through its decomposition temperature. An attempt was made to estimate ΔH for the events by calibrating the filament with the melting of indium metal. We found it difficult to achieve a sufficient degree of thermal equilibrium to allow us to be confident of quantitation by this procedure.

The RSFT-IR/thermal profiling technique is well illustrated with the results for two compounds, DATH²¹ and PTTN,²² whose thermolysis products



have recently been characterized at both slow and fast heating rates.

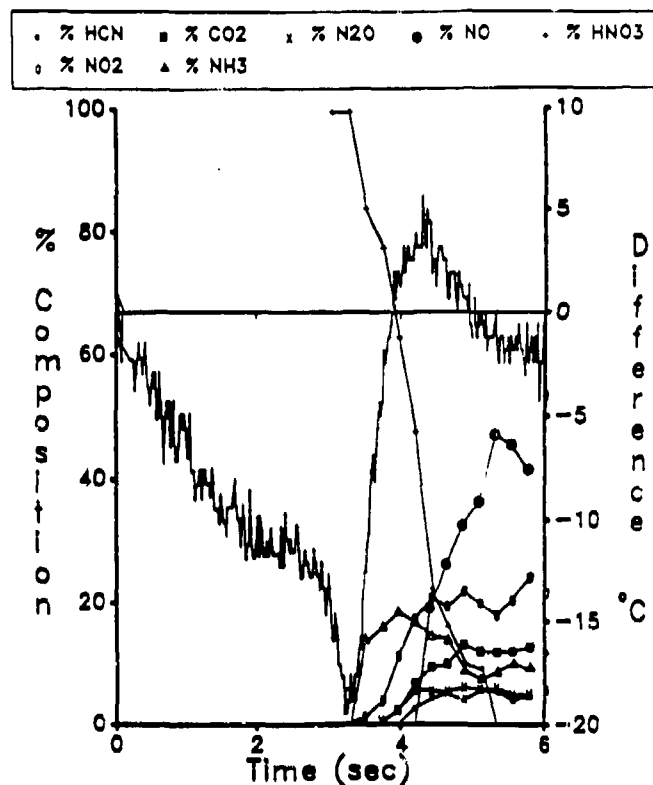


FIG. 4. The temperature difference trace (sample temperature minus reference temperature) of the filament, superimposed on the gas products quantified for PTTN heated at about 100°C/s under 15 psi Ar.

Thermolysis of DATH. Figure 3 is the superimposition of the thermal profile of the condensed phase and the relative concentrations of the quantified gas products from thermolysis of one mg of DATH heated at an initial rate of 80°C/s. According to the thermal trace, the first thermal event is endothermic melting at 133°C, which corresponds remarkably well to the value measured at a slow heating rate (133°C).²¹ The melt phase heats until decomposition begins and the first IR-active gas product (N₂O) is detected. N₂O was earlier observed to be one of the dominant IR-active gas products.²¹ This event occurs in the 160–165°C range, which corresponds well to the onset of weight loss at 158°C measured by TGA at a much slower heating rate (10°C/min).²¹ On the basis of thermal profile in this temperature range, the loss of N₂O appears to be a slightly endothermic or thermally neutral event. However, at 195–200°C there occurs a vigorous exotherm that drives the filament temperature above that of the reference trace (corresponding to the temperature that takes place with no sample present). The temperature of the exotherm coincides with the temperature where vigorous weight loss occurs in the TGA (197°C).²¹ At this time, the relative concentrations of the gas products change markedly and are dominated by CO, CO₂, and H₂O (not quantified). Undoubtedly, the absence of nitrogen-containing products in the IR spectrum results from the formation of N₂. The products are essentially those of combustion; hence, the exotherm might be thought of as an ignition or, possibly, an explosion.

The correspondence of the thermal events at 80°C/s in this experiment to those at 10°C/min is remarkably

food for DATH and strongly implies that the decomposition characteristics are essentially the same at these two rather different heating rates. This implication is surprising in light of the fact that the IR-active decomposition products are known to strongly depend on the heating rate.²¹ Instead of a change in the decomposition mechanism, this dependence on dT/dt appears to result from a transition from controlled decomposition to self-acceleratory deflagration, in which the first detected decomposition products engage in further reactions leading to the more thermodynamically stable final products characteristic of combustion. Also revealed is the presence of endothermic degradation reactions leading to gas products in advance of the strongly exothermic and probably autocatalytic deflagration reactions.

Thermolysis of PTTN. PTTN illustrates the usefulness of displaying the thermal profile as a difference trace (sample temperature minus reference temperature). The difference plot reveals subtle slope changes that can sometimes be disguised in the simple thermal profile of the filament. Figure 4 shows the overlay of the difference trace and the relative concentrations of the IR-active gas products quantified for PTTN. PTTN was heated at an initial rate of about 100°C/s in these experiments. At a slow heating rate (5°C/min), melting of PTTN with decomposition occurred at 217°C.²² However, at 100°C/s no melting endotherm could be detected. Instead, the thermal difference trace begins—immediately upon heating—as a negative slope, owing to the heat capacity of the sample. At about 300°C a distinctly endothermic event takes place that is concurrent with the appearance of HNO₃(g). Thus, proton transfer and desorption is the initial reaction. Proton transfer from an ammonium ion to NO₃⁻ followed by desorption of HNO₃ is definitely shown to be endothermic, on the basis of studies with NH₄NO₃.²³

As energy continues to be fed to the sample, a strongly exothermic process quickly follows the proton transfer step and is accompanied by the appearance of backbone decomposition products that were quantified (NH₃, CO, CO₂, HCN) and products not quantified (HNCO and H₂O), along with NO₂, a decomposition product of HNO₃. Following this vigorously exothermic event, the filament is sufficiently hot (~380°C) that reactions (perhaps among gas products) leading to the formation of NO(g) clearly become important. The filament temperature is not affected by reactions taking place entirely in the gas phase.

The considerable detail about the thermal decomposition of DATH and PTTN that is revealed by the combining of thermal profiling and real-time infrared spectroscopy should advance understanding of the fast thermal decomposition mechanisms of other pure materials and mixtures and of the relationship of the thermal profiles to the impact sensitivity, as well as understanding of catalytic processes. We are currently pursuing research in all these areas.

ACKNOWLEDGMENTS

We are grateful to the Army Research Office for support of this research under DAAG29-84-K-0198. A sample of DATH was provided by D. O. Woolery of Rocketdyne, and a sample of PTTN was provided by W. S. Anderson of Chemical Systems Division of United Technologies. T. P. Russell recorded the spectra and thermal trace of PTTN.

1. Y. Oyumi and T. B. Brill, *Combust. Flame* **62**, 213 (1985).
2. T. B. Brill and Y. Oyumi, *J. Phys. Chem.* **90**, 2679 (1986).
3. Y. Oyumi, A. L. Rheingold, and T. B. Brill, *Prop. Explos. Pyrotech.* **12**, 1 (1987).
4. T. B. Brill and Y. Oyumi, *J. Phys. Chem.* **90**, 6848 (1986).
5. Y. Oyumi, T. B. Brill, and A. L. Rheingold, *J. Phys. Chem.* **90**, 2526 (1986).
6. Y. Oyumi and T. B. Brill, *J. Phys. Chem.* **91**, 3657 (1987).
7. Y. Oyumi and T. B. Brill, *Combust. Flame* **68**, 209 (1987).
8. Y. Oyumi and T. B. Brill, *Combust. Flame* **67**, 121 (1987).
9. Y. Oyumi, T. B. Brill, and A. L. Rheingold, *Thermochem. Acta* **114**, 209 (1987).
10. J. T. Cronin and T. B. Brill, *J. Phys. Chem.* **90**, 178 (1986).
11. Y. Oyumi and T. B. Brill, *Prop. Explos. Pyrotech.* **11**, 35 (1986).
12. J. Wenograd, *Trans. Farad. Soc.* **57**, 1621 (1961).
13. P. R. Solomon, M. A. Serio, R. M. Carangelo, and J. R. Markham, *Fuel* **65**, 182 (1986).
14. R. L. Coates, *AIAA J.* **3**, 1257 (1965).
15. N. S. Cohen, R. W. Fleming, and R. L. Derr, *AIAA J.* **12**, 212 (1974).
16. A. D. Baer, *J. Fire & Flammability* **12**, 214 (1981).
17. J. H. Hedges, A. D. Baer, and N. W. Ryan, *Proceedings of the 7th Symposium (International) on Combustion (The Combustion Institute, Pittsburgh, Pennsylvania, 1978)*, p. 1173.
18. E. N. Price, R. K. Sigman, R. J. Powers, C. Markoy, and J. K. Sambamurthi, Final Report on N00014-79-C-0764, Office of Naval Research, Washington, D.C., August 1986.
19. R. J. Kerpowicz, Ph.D. dissertation, University of Delaware, Newark (1984).
20. J. A. A. Ketelaar, *Spectrochim. Acta* **14**, 237 (1959).
21. Y. Oyumi, A. L. Rheingold, and T. B. Brill, *J. Phys. Chem.* **91**, 920 (1987).
22. Y. Oyumi, T. B. Brill, and A. L. Rheingold, *J. Phys. Chem.* **89**, 2309 (1985).
23. W. A. Rosser, S. H. Inami, and H. Wise, *J. Phys. Chem.* **67**, 1753 (1963).

Acoustic Levitation as an IR Spectroscopy Sampling Technique

J.T. Cronin and T.B. Brill*
Department of Chemistry
University of Delaware
Newark, DE 19716

Abstract

Acoustic levitation of liquid droplets (<4 mm dia.), bubbles and solid particles is described as an unusual sampling technique for obtaining the infrared spectrum of samples that might be incompatible with conventional sample support methods, and for studies of materials under extreme conditions. Excellent FTIR spectra were recorded of bubbles of a concentrated aqueous nitrate solution, mineral oil, and an aqueous surfactant solution. Polymethacrylic acid packing foam also produced a high quality spectrum. Large aqueous droplets and dense solids gave unsatisfactory spectra. The design of the levitator and various spectroscopic considerations are discussed.

Introduction

Major experimental challenges are frequently encountered when FTIR spectroscopy is attempted on highly reactive substances. For example, the material might rapidly react with the sample support. In situ, IR spectroscopy of dynamically changing materials, such as occurs during combustion of a solid or liquid, also presents a problem with the sample support. Static levitation of solid and liquid samples in air (or other gases, if desired) is described in this paper as an approach to problems of this type.

From a spectroscopic point of view, IR spectra of large (0.1-5 mm dia.) semi-spherical particles suspended in a second medium is photometrically complex because of the potential for both absorption and reflection of the IR

radiation and the different pathlengths of the sample. However, such problems might be of interest in casting light on the spectral features of heterogeneous mixtures in which large particles of one material are dispersed in another medium.

Various methods for stationary positioning of materials in a gas or vacuum (containerless processing) have been developed: optical, electrostatic, electromagnetic, aerodynamic and acoustic. Optical levitation employs the force of a vertically directed TEM_{00} Gaussian mode CW laser to support a 1-40 μ m dia. particle.¹ Electrically conductive materials can be levitated by appropriately designed AC coils and is the basis of electromagnetic levitation.^{2,3} Electrostatic levitation uses appropriately positioned electrodes to produce a two- or three- dimensional potential minimum^{2,4} into which a charged sample can be placed. The Bernoulli effect created by a gas jet from various shaped nozzles is the basis of aerodynamic levitation.^{5,6} Aerodynamic levitation can be applied to most materials, but is not useful for liquids with a significant vapor pressure. Acoustic levitation, in which the sample is suspended in the pressure wells caused by the interference pattern of monochromatic sound waves, is the most generally applicable method from the point of view of minimizing the perturbations to the sample.^{2,7} It was therefore chosen to levitate samples for FTIR studies. Previously, acoustic levitation has been used to record the IR spectrum of ammonium sulfate by measuring the absorbance values at 50 cm^{-1} intervals and plotting them.⁸ To our knowledge broad-band FTIR spectra have not been previously obtained on levitated samples, and, thus, the technique has not been generally evaluated.

FTIR spectra of droplets of a concentrated aqueous nitrate salt based solution (LGP1845), of solid particles of polymethacrylic acid packing

material, and bubbles of LGP1845, mineral oil and the aqueous surfactant sodium dodecyl diphenyloxide disulfonate, all in the levitated environment are discussed in this paper.

Feasibility Studies

The potentially long, non-uniform optical pathlength created by a large levitated droplet could severely complicate IR spectra. To evaluate the potential problems and to aid in the experimental design, two preliminary studies were performed. Droplets tethered on a Teflon-coated wire and suspended in the beam of the FTIR spectrometer and droplets suspended between two Teflon-coated wires on the stage of an IR microscope were studied to learn how the spectrum is influenced by the diameter of the IR beam, the position of the focal point of the beam with respect to the droplet, and the proportion of absorbance and reflectance over the non-uniform pathlength of the sample.

Tethered droplets are tear-shaped rather than spherical but sufficiently simulate levitated droplets to be worthy of study. It was found that a 3-4 mm droplet of a concentrated aqueous salt solution tethered in the IR beam of a Nicolet 60SX FTIR spectrometer produced no spectral detail. A pin-point aperture placed in front of or behind the droplet to increase the ratio of radiation encountering the sample to that passing around it had little effect. A Nicolet Microbeam accessory was then used to focus the IR radiation at various points on the surface of the tethered droplet. Some spectral detail was observed that strongly depended on the position of the beam on the droplet surface. Figure 1 shows the spectrum of a tethered LGP1845 droplet (see Experimental for the composition) positioned slightly off-center of the IR beam compared to the Circle Cell spectrum of the same material. The droplet spectrum indicates that complex reflection/absorption effects exist, but

demonstrates that spectra of droplets can probably be acquired. However, beam focusing appears to be necessary to study levitated droplets successfully. Also, this experiment revealed that the diameter of the droplet diminished by about 20% after 20-30 min in the IR beam as a result of evaporation due to heating.

A Spectra-Tech IR Plan microscope and Nicolet 20DXB FTIR spectrometer were used to investigate the effect of the beam position on the spectrum of the tethered droplet. Attempts were made to obtain both absorption and reflection spectra. A spectrum matching the absorption or reflection spectrum of a thin film of LGP1845 was not obtained from the droplet, but the absorption spectra most closely matched one another when the beam was near the annulus of the sample. This suggested that the annular region where the pathlength is the shortest is most responsible for the absorption component.

Acoustic Levitation

With the above preliminary information in mind, the design of a levitation/optical system can be envisioned in which the chance for success is optimized. An interference-type acoustic levitator⁷ was built that made use of a reflected monochromatic sound wave to produce an interference pattern. A parabolic driver machined from titanium and driven by four piezoelectric ceramic disks produced a 22.7 KHz sound wave that reflected from a flat circular reflector whose diameter was $1/2\lambda$. The approximately spherical shaped reflected wave interfered with the primary wave to create a series of nodes and anti-nodes with continuous restoring forces in all dimensions around the pressure nodes. The nodes and anti-nodes are separated by $1/2\lambda$. In the absence of air currents and temperature changes, droplets could be held stationary for spectroscopic study. The maximum theoretical droplet diameter

5

is about $1/2\lambda$ at 22.7 KHz. This corresponds to about 7 mm. In practice, the maximum diameter was 3-4 mm without severely distorting the energy well.

Figure 2 shows a diagram of the acoustic driver assembly.

It was necessary to construct a separate optical bench for the Nicolet 60SX to accommodate the driver and permit the IR beam to be focused on the levitated droplet. This arrangement is shown in Figure 3. The f1 optics of a Nicolet Microbeam accessory were remounted on the optical bench along with an MCT-A detector as shown in Figure 4. A plexiglas box was constructed around the bench to reduce the air currents and to permit purging. Droplets and particles could be positioned in the IR beam after moderate effort was expended in adjusting the mirrors and levitator.

Experimental

Acoustic Levitator. The acoustic driver useful for levitation is shown in Figure 2. It consists of four piezoelectric crystals and electrodes (supplied by Intersonics, Northbrook, IL), a cylindrical aluminum body (8x2 in.), a "change-in-diameter" area and a parabolic titanium driver cone with a terminal radius of 2.5 in. A Hewlett-Packard 3325A function generator set to produce a 22.745 KHz sine wave was amplified by a 90W PS-200 Crown stereo amplifier. The signal was matched to the impedance of the levitator (100 ohms) by a transformer. Pressure waves ($\lambda=15$ mm) are reflected from the flat face of a 7 mm dia. S.S. rod mounted on a screw. The distance between the reflecting rod and the driver cone was adjustable by the screw because λ is somewhat dependent on the temperature. The levitator was constructed, in part, with the help of Intersonics, Inc. (Northbrook, IL) who recommended several modifications to the design of the driver, and analyzed and matched the impedance of the driver to the audio amplifier. Figures 3 and 4 show the external optical bench which was

designed for this experiment. The mirrors from a Nicolet Microbeam accessory were used and positioned on the basis of a blueprint for the device. The HeNe laser of the IR spectrometer was used to align the mirrors. The levitator driver was mounted on an Ardel xy translator and a labjack to permit xyz adjustments.

A PlexiglasTM box was constructed to enclose the optical bench. The top and three sidewalls of this box contained glove ports. Since movement of the gloves produced air currents that destabilized the levitated droplets, it was decided to leave the top port open. The CO₂ and H₂O levels were allowed to equilibrate before recording the background and sample spectra. Several minutes were required to warm up the driver cone and the levitator body during which time the frequency shifted by 5-10 Hz. The small shift in the resonance frequency was monitored on a dual channel oscilloscope as the difference in the phase angle between the voltage and current of the levitator. The most stable levitation was achieved when the phase angle was maintained at zero. While the levitator was at power, protective earmuffs were used.

Liquid droplets were introduced into the nodes by a fine capillary tube drawn from a disposable pipet. Bubbles were formed by the use of larger capillary tubes. Solids could be placed in the nodes with a tweezers or a spatula. Droplets and solids were normally levitated in the strongest (first) node, while bubbles were levitated in the less intense second node. The material was then positioned in the beam by xyz translation of the driver and the stability then improved by adjusting the position of the reflecting rod.

Spectra were recorded on a Nicolet 60SX FTIR spectrometer with an MCT-A detector. Typically 200 interferograms at 4 cm⁻¹ resolution were collected. Once studied, the sample was allowed to fall out of the node by reducing the

sound power, and the background spectrum was then recorded.

Samples. LGP1845 is a solution of 63.2% hydroxylammonium nitrate, 19.9% triethanolammonium nitrate and 17.3% H₂O.¹³ Sodium dodecyl diphenyloxide disulfonate (Dowfax) was obtained from Reichhold Chemicals, Inc.

IR Spectra of Liquid Spheres

In keeping with the results obtained with tethered droplets, spectra of levitated semi-spherical droplets were largely unusable. Figure 5 shows a typical spectrum of a droplet of LGP1845. The throughput is low. There is evidence of a strong spectral reflectance component in that the N-H symmetric stretch at 3000 cm⁻¹ has some derivative characteristics and $\nu_3(\text{NO}_3^-)$ at about 1400 cm⁻¹ is highly asymmetric. On the other hand, it was discovered that bubbles could occasionally be formed and stably levitated at low power. Good quality IR spectra could be obtained with the infrared beam centered on the bubble. Figure 6 shows the spectrum of a bubble of LGP1845 along with the spectrum obtained with a Circle Cell. Because of the longer pathlength of the bubble compared to the Circle Cell (as much as 100 μM compare to 10 μM), the bubble spectrum is considerably more intense. Figure 7 shows the spectrum of levitated bubbles of mineral oil along with the spectrum recorded with the Circle Cell. Again, the bubble has much greater absorbance, but the spectral details closely resemble those measured with the Circle Cell. There is some evidence of dispersion as indicated by the absorption peak at 3250 cm⁻¹ in the Circle Cell spectrum which appears to be inverted in the bubble spectrum. Figure 8 shows the spectrum of a levitated bubble of H₂O containing sodium dodecyl diphenyloxide disulfonate (Dowfax) surfactant. The Circle Cell spectrum closely resembles it, taking into account the difference in the total absorbance.

IR Spectra of Solids

Solid samples could be stably levitated with little effort. A translucent sample of polymethacrylic acid low density packing foam cut to a 3x4 mm rectangle was levitated with a low acoustic power. The sample was easily positioned in the IR beam using the xyz translation support on the levitator. The IR throughput was about 50%. Figure 9 shows the spectrum of the sample compared to that of a thin film. The correspondence is excellent. A solid pellet of polymethacrylic acid with a reflecting or a roughened surface failed to produce a spectrum having any detail.

Discussion

The quality of FTIR spectra of levitated samples is affected by the stability of the levitation, the position of the sample in the IR beam, and the nature and size of the sample. With regard to the levitation stability, small movement (oscillations) of the sample causes a change in the amount of IR radiation that encounters the sample. Large differences in the throughput result, causing spectral inaccuracies. Best results were obtained when the sample visually appeared to be stationary. The reduction of air currents, careful tuning of the levitator, and the use of an appropriately sized sample strongly enhanced the stability of the levitation.

Once stably levitated, the position of the sample in the IR beam was important. The location of the focal point at the front surface, center, or back surface greatly influenced the results. The best spectra were obtained with the focal point at the back half or at the center of the droplet. In these cases, most of the droplet was enveloped by the beam.

The physical properties of the sample are important. Aqueous solutions

with a low vapor pressure and a high surface tension levitated well. Droplets of liquids with low surface tensions often ruptured. A liquid with a high vapor pressure tended to evaporate rapidly because of heating by the IR beam and the energy transferred from the sound wave. If such a sample is not isolated from the optical bench, the vapor can contaminate the bench and become part of the spectrum. The maximum practical diameter for droplets levitated in the device described here is 3-4 mm. Larger droplets deformed and were less stable.

Spectra of 1-4 mm diameter droplets were generally poor. Absorption and specular reflectance features were evident in several spectra, but the details were difficult to reproduce because of the complexity of the photometrics. For instance, artifacts can arise resulting from the multiple sample pathlengths. Although the Mertz method of phase correction using 1024 data points was employed,¹⁰ the number of experimental variables involved in obtaining spectra of levitated materials precluded a detailed analysis of any phase-related problems.

Levitated bubbles of organic materials and aqueous solutions produced good to excellent spectra that closely resemble those obtained with a Circle Cell. This is because the pathlength is small enough to transmit a significant amount of radiation. The technique is the most suitable for samples in this situation. However, successful use of acoustic levitation as an IR sampling technique for wider applications might be enhanced by employing a recently developed driver configuration in which two opposed radiators are used.¹¹ This method gives more stable levitation and is much less dependent on the temperature compared to the interference levitator described here.¹¹ Also, recording the IR emission spectrum rather than the absorption spectrum from

droplets and solid particles might be a promising approach.¹³ However, the results with bubbles and selected solids demonstrate that levitation is a very satisfactory sampling method for obtaining IR absorption spectra in specialized applications.

Acknowledgements

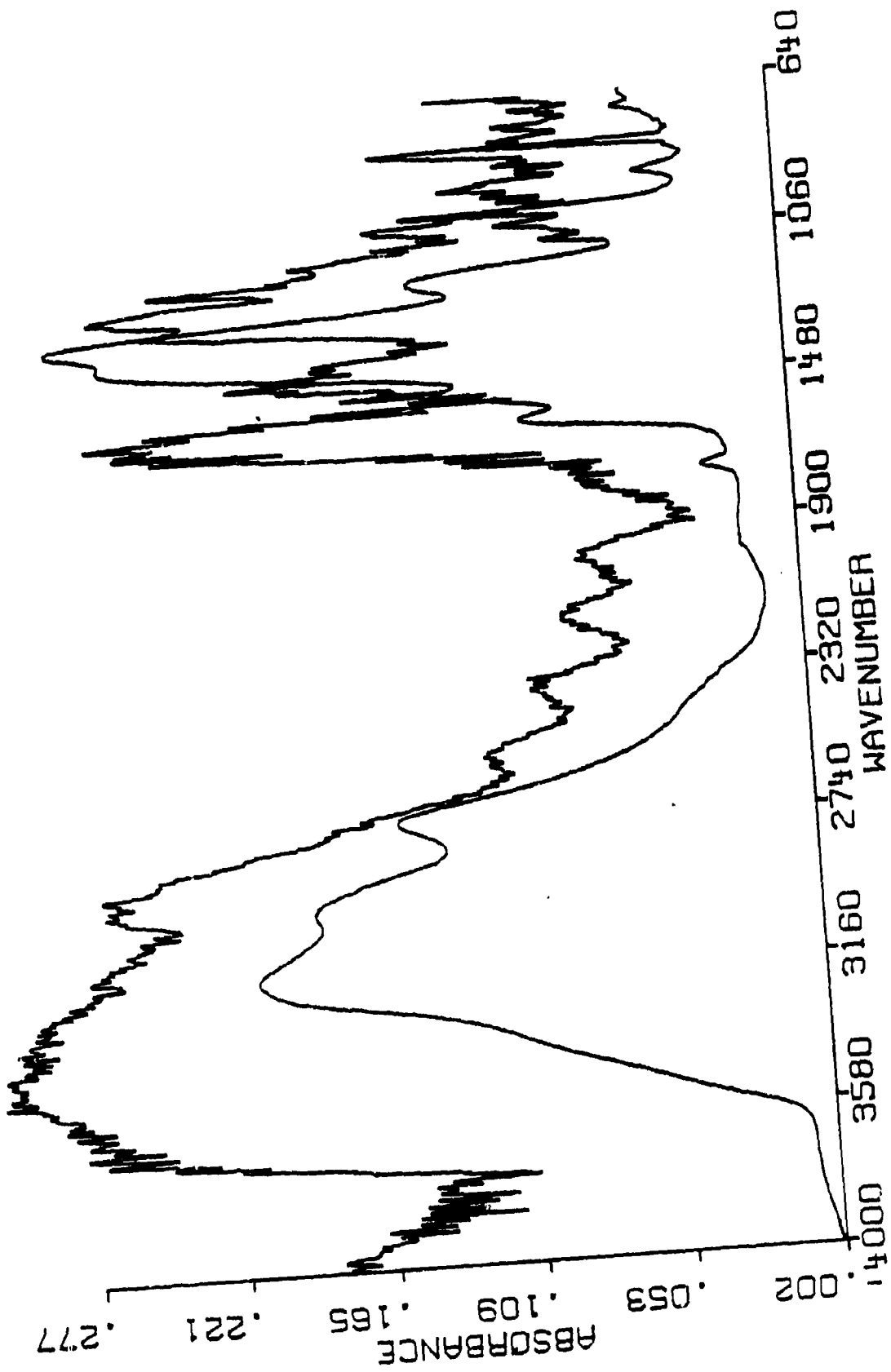
We are grateful to the Army Research Office for support of this work on DAAG29-84-K-0198. The tethered droplet spectra taken with a beam condenser were measured at Himont, Inc., Wilmington, DE. The IR-microscope and Nicolet 20DXB spectrometer were used at Reichhold Chemicals, Inc, Dover, DE. We are grateful to Dr. R. Rosenthal of Nicolet Analytical Instruments for providing the mirrors of the microbeam accessory and for helpful discussions. We also thank Dr. D. B. Chase of The DuPont Central Research Dept. for comments on the spectroscopy and Dennis R. Merkley of Intersonics for help with the levitation system.

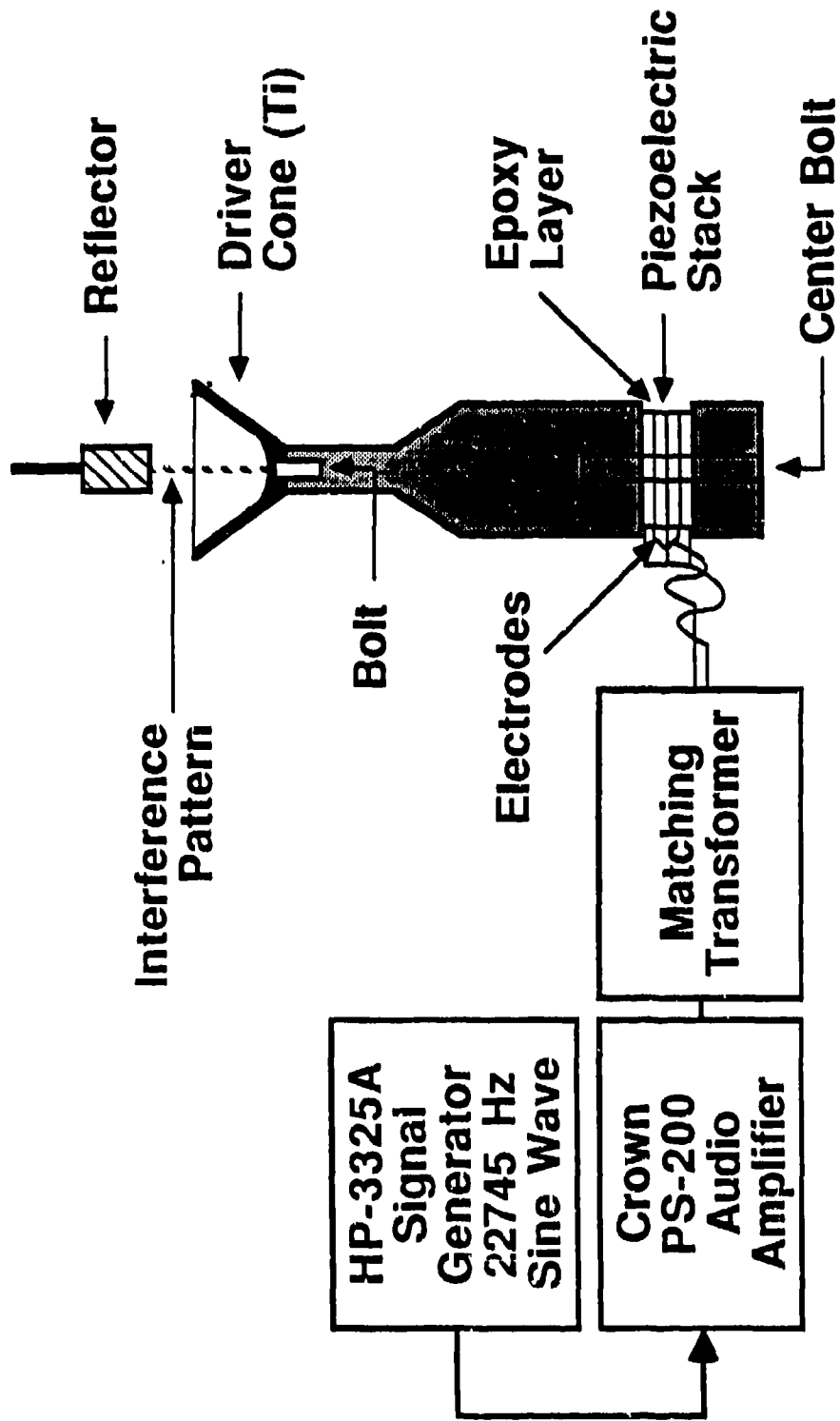
References

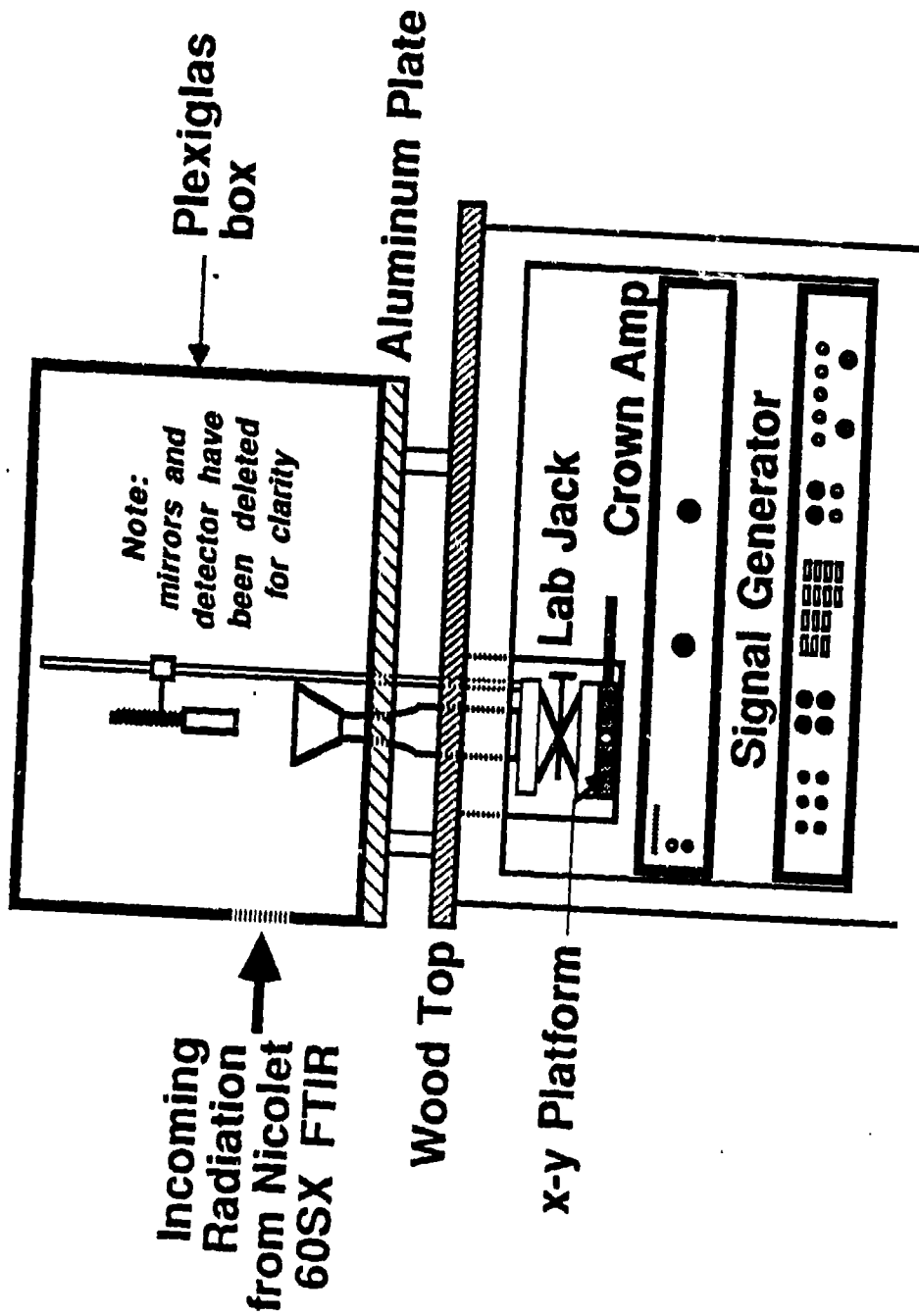
1. Ashkin, A. Science, 210, 1085 (1980).
2. Barmatz, M. "Overview of Containerless Processing Technologies", Proc. MRS Annual Meeting, November (1981).
3. Okress, E.C.; Wroughton, D.M.; Comenetz, G.; Brace, P.H.; Kelly, J.C.R.; J. Appl. Phys., 23, 545 (1952).
4. Clancy, P.F.; Lierka, E.G.; Grossbach, R.; Heide, W.M.; Thirteenth Congress, International Astronautical Federation, Munich, Sept. (1979)
5. Winborne, D.A.; Nordine, P.C.; Rosner, D.E.; Murley, N.F.; Met. Trans, B7b, 711 (1976).
6. Nordine, P.C.; Atkins, R.M., Rev. Sci. Instrum., 53, 1456 (1982).
7. Whymark, P.C.; Rey, C.; Yearnd, J.; Broz, R., Proc. 17th AIAA Mtg. paper 79-0370, New Orleans, LA, Jan. 1979.
8. Grader, G.S.; Flagan, R.C.; Seinfeld, J.H., Rev. Sci. Instrum., 58(4) 584 (1987).
9. Rey, C.A.; Danley, T.J.; Merkley, D.R.; Hammerlund, G.R., Proceedings 114th Meeting of The Acoustical Society of America, November (1987). Miami, FL.
10. Griffiths, P.R. deHaseth, J.A. "Fourier Transform Infrared Spectroscopy" Wiley-Interscience, N.Y., N.Y. 1986.
11. D.R. Merkley, Interionics, Inc. personal communication, 1988.
12. Griffiths, P.R.; Appl. Spectrosc. 26, 73 (1972).
13. For a review of LGP1845 propellants see Klein, N., BRL-TR-2641, Ballistic Research Laboratory, Aberdeen Proving Ground, MD, Feb. 1, 1985.

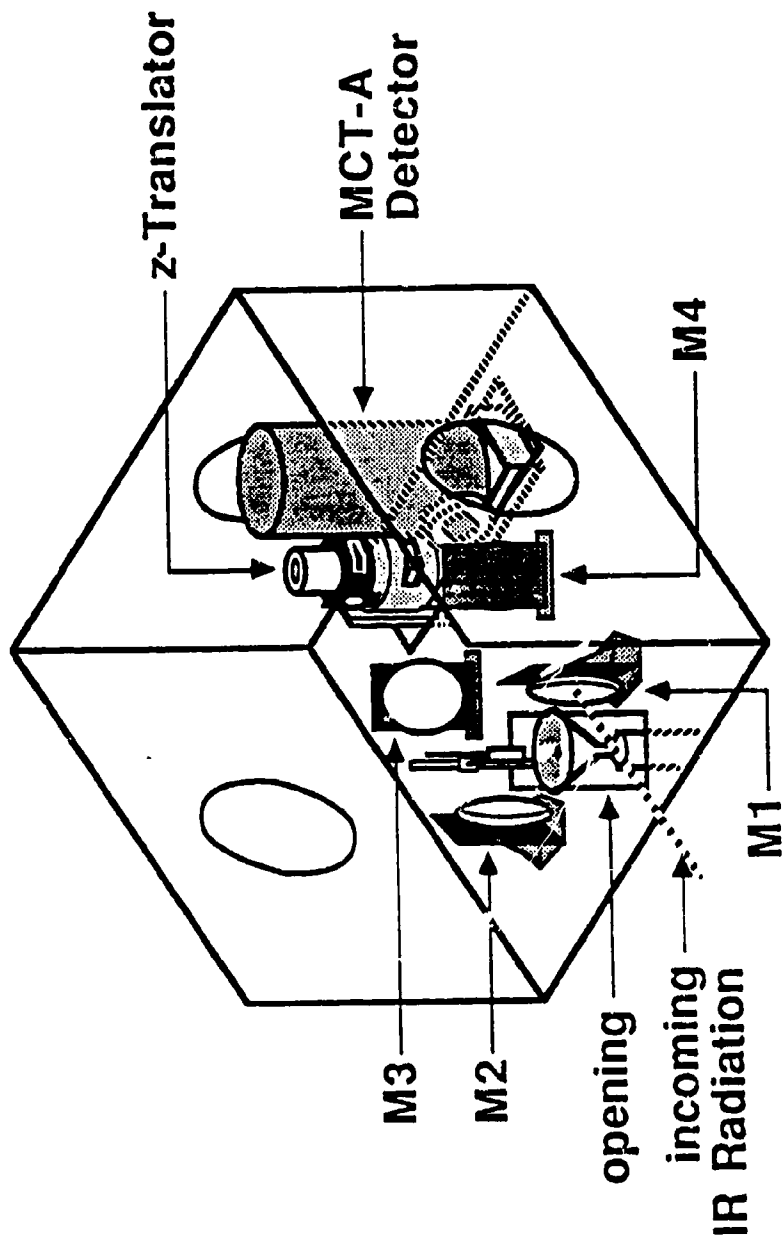
Figure Captions

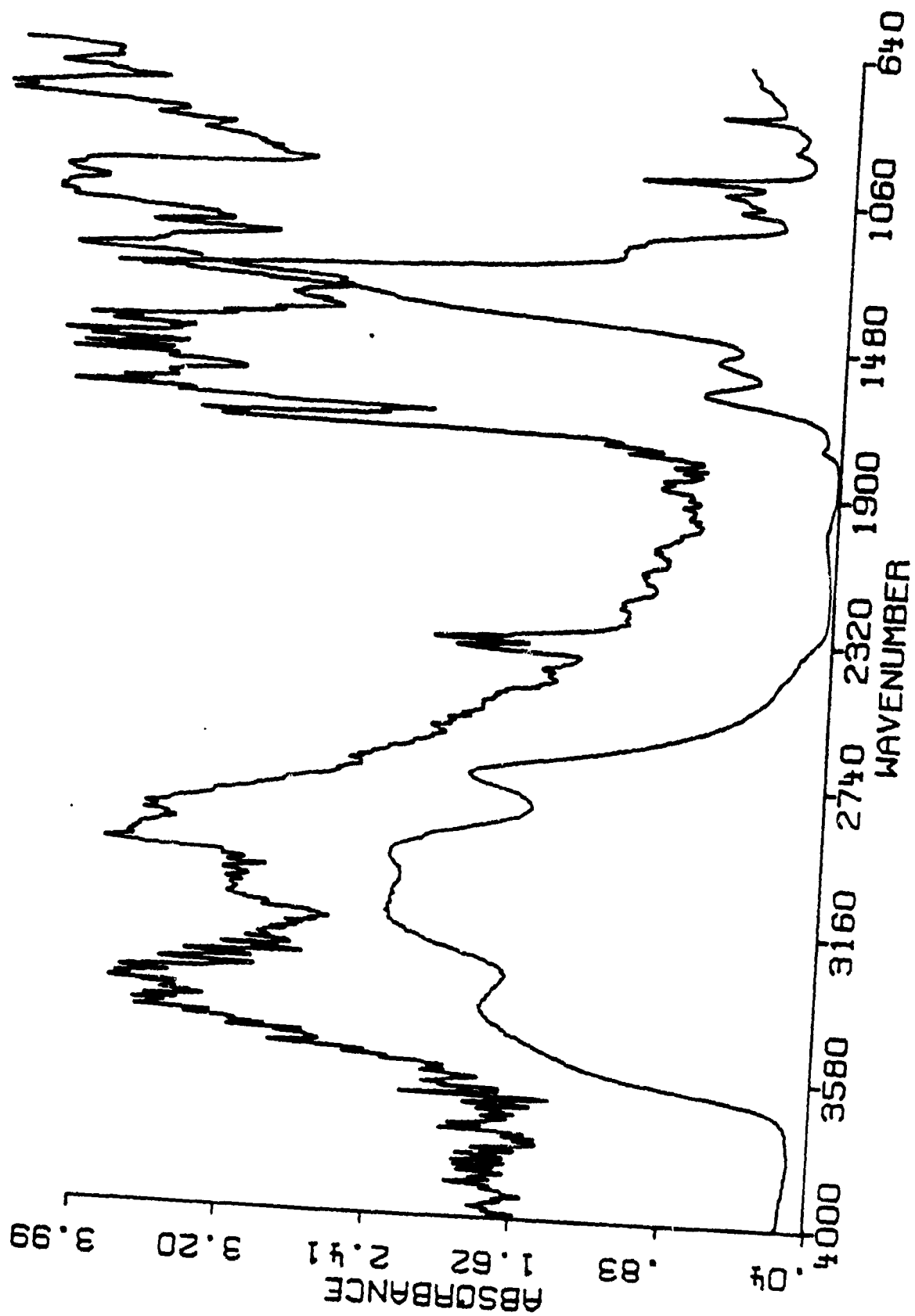
- Figure 1. (top) The IR spectrum of a tethered 3 mm dia. droplet of LGP1845 using Microbeam-focused IR radiation off-center from the droplet. (bottom) The spectrum of LGP1845 taken with a Circle Cell. The absorbance scale refers to the tethered droplet.
- Figure 2. A diagram of the levitator assembly.
- Figure 3. Support system for the levitator.
- Figure 4. Schematic of the optical bench for acoustic levitation.
- Figure 5. (top) The FTIR absorption spectrum of a levitated droplet of LGP1845 compared to the Circle Cell spectrum (bottom). The droplet spectrum is very poor because absorption with various pathlengths and reflection takes place simultaneously.
- Figure 6. (top) The absorbance spectrum of a levitated bubble of LGP1845. (bottom) The Circle Cell spectrum of LGP1845. Because of the longer sample pathlength, the bubble spectrum is more intense but the spectral features match well.
- Figure 7. (top) The absorbance spectrum of a levitated bubble of mineral oil compared to the Circle Cell spectrum (bottom). Except for intensity differences, there is a close match.
- Figure 8. (top) The absorbance spectrum of a levitated bubble of aqueous sodium dodecyl diphenyloxide disulfonate compared to the Circle Cell spectrum. Except for intensity differences, there is a close match.
- Figure 9. (top) The absorbance spectrum of levitated particle of polymethacrylic acid packing foam compared to the spectrum of a thin film of the material (bottom). The correspondence is excellent.











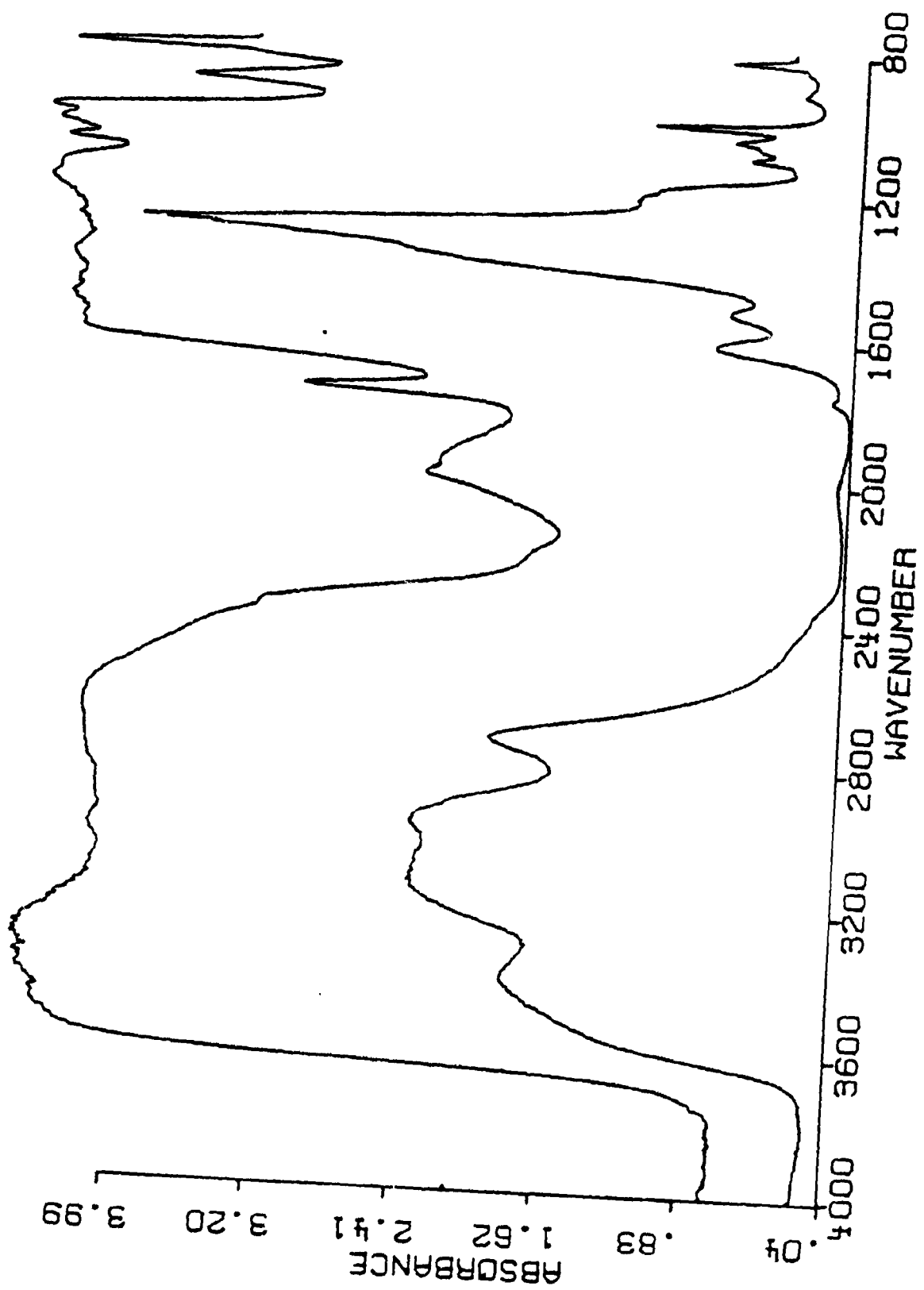


Figure 6

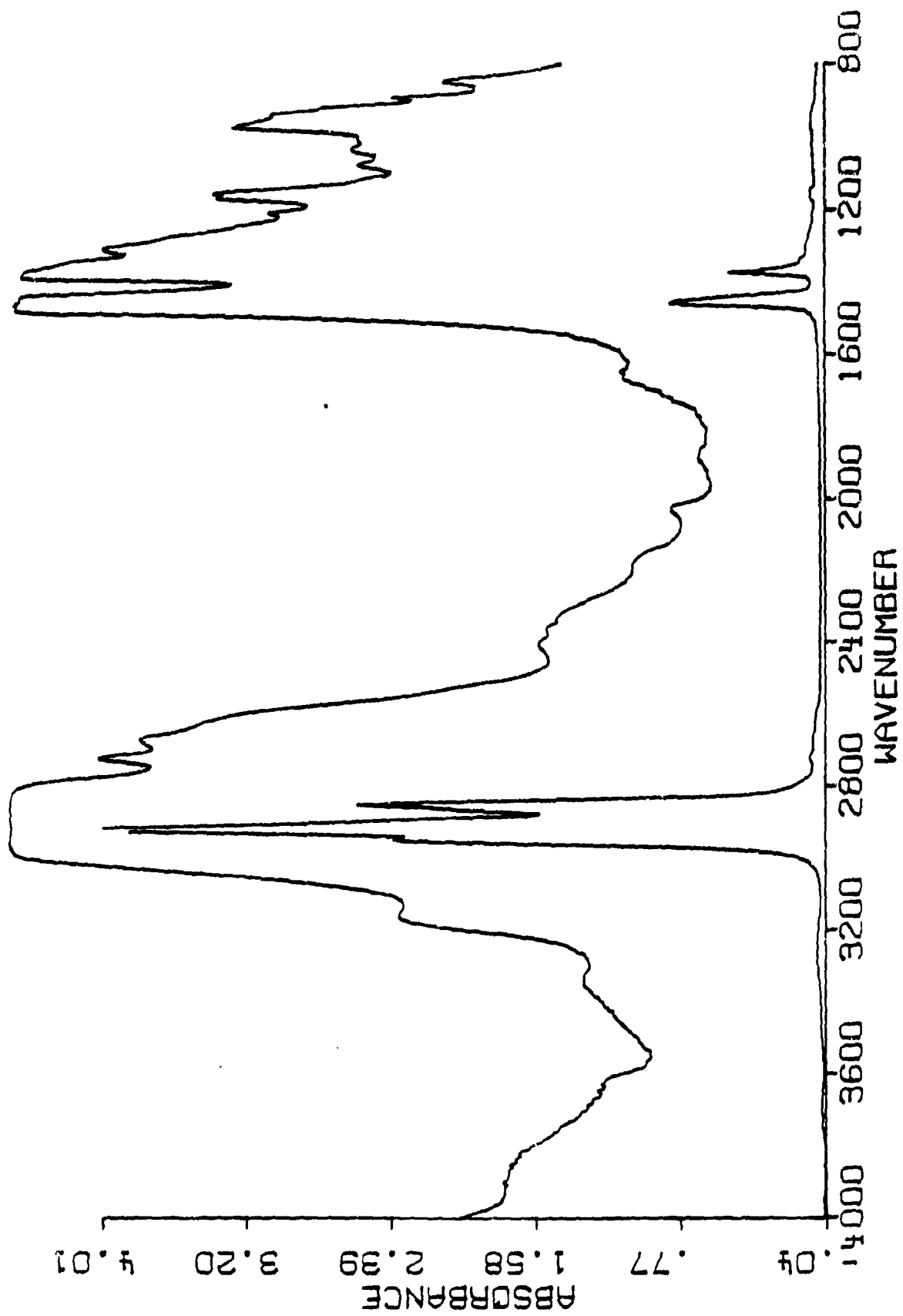


Figure 8

